Dissertation

APPLICATION OF STRUCTURED ILLUMINATION MICROSCOPY (SIM) IN STUDYING MITOCHONDRIAL STRUCTURE AND FUNCTION

submitted by

BSc MSc

Benjamin Gottschalk

for the Academic Degree of

Doctor of Philosophy

(PhD)

at the

Medical University of Graz

Gottfried Schatz Research Center

Molecular Biology and Biochemistry

under the Supervision of

Univ.-Prof. Mag.pharm. Dr.rer.nat. Wolfgang Graier

2019

Statutory Declaration

I hereby declare that this thesis is my own original work and that I have acknowledged by name all who have made a contribution. Furthermore, all sources used for the preparation of the thesis are cited. Throughout this thesis and for all related publications, I followed the Standards of Good Scientific Practice and Ombuds Committee at the Medical University of Graz.

Graz, September 9th, 2019 *Benjamin Gottschalk*

Disclosures

Part of this thesis has been published in:

Gottschalk B, Klec C, Leitinger G, Bernhart E, Rost R, Bischof H, Madreiter-Sokolowski CT, Radulović S, Eroglu E, Sattler W, Waldeck-Weiermair M, Malli R, Graier WF. MICU1 controls cristae junction and spatially anchors mitochondrial Ca^{2+} uniporter complex. *Nat Commun*. 2019 Aug 19;10(1):3732. doi: 10.1038/s41467-019-11692-x

Gottschalk B, Klec C, Waldeck-Weiermair M, Malli R, Graier WF. Intracellular Ca^{2+} release decelerates mitochondrial cristae dynamics within the junctions to the endoplasmic reticulum. Pflugers Arch. 2018 Aug;470(8):1193-1203. doi: 10.1007/s00424-018-2133-0.

The following co-authors contributed to my first-author publications:

Christiane Klec[1], Corina T. Madreiter-Sokolowski[1,2], Maria Depaoli[1], Gerd Leitinger[1], Eva Bernhart[1], René Rost[1], Snjezana Radulovic[1], Felix Karsten[1], Helmut Bischof[1], Emrah Eroglu[1], Wolfgang Sattler[1], Markus Waldeck-Weiermair[1], Roland Malli[1], Wolfgang F. Graier[1]

[1]Medical University of Graz, Neue Stiftingtalstraße 6/6, 8010 Graz, Austria

I confirm that all co-authors have agreed to use their data in my thesis. I have permission from the publisher to reproduce figures published in Gottschalk et al. (2018) and Gottschalk et al. (2019). Both papers (Gottschalk et al. (2018)[88] and Gottschalk et al. (2019)[96]) are distributed under the terms of the Creative Commons CC BY license, which permits unrestricted use, distribution, and reproduction in any medium, provided the original work is properly cited.

During my PhD thesis I also contributed to the following publications:

Publication bibliography:

Bärnthaler, Thomas; Maric, Jovana; Platzer, Wolfgang; Konya, Viktoria; Theiler, Anna; Hasenöhrl, Carina et al. (2017): The Role of PGE2 in Alveolar Epithelial and Lung Microvascular Endothelial Crosstalk. In: Scientific reports 7 (1), S. 7923. DOI: 10.1038/s41598-017-08228-y.

Bernhart, Eva; Kogelnik, Nora; Prasch, Jürgen; Gottschalk, Benjamin; Goeritzer, Madeleine; Depaoli, Maria Rosa et al. (2018): 2-Chlorohexadecanoic acid induces ER stress and mitochondrial dysfunction in brain microvascular endothelial cells. In: Redox biology 15, S. 441–451. DOI: 10.1016/j.redox.2018.01.003.

Bischof, Helmut; Rehberg, Markus; Stryeck, Sarah; Artinger, Katharina; Eroglu, Emrah; Waldeck-Weiermair, Markus et al. (2017): Novel genetically encoded fluorescent probes enable real-time detection of potassium in vitro and in vivo. In: Nature communications 8 (1), S. 1422. DOI: 10.1038/s41467-017-01615-z.

Burgstaller, Sandra; Bischof, Helmut; Gensch, Thomas; Stryeck, Sarah; Gottschalk, Benjamin; Ramadani-Muja, Jeta et al. (2019): pH-Lemon, a Fluorescent Protein-Based pH Reporter for Acidic Compartments. In: ACS sensors 4 (4), S. 883–891. DOI: 10.1021/acssensors.8b01599.

Deak, Andras T.; Gottschalk, Benjamin; Eroglu, Emrah; Rost, Rene; Waldeck-Weiermair, Markus; Graier, Wolfgang F.; Malli, Roland (2018): High-Resolution Imaging of STIM/Orai Subcellular Localization Using Array Confocal Laser Scanning Microscopy. In: Methods in molecular biology (Clifton, N.J.) 1843, S. 175–187. DOI: 10.1007/978-1-4939-8704-7_15.

Depaoli, Maria R.; Karsten, Felix; Madreiter-Sokolowski, Corina T.; Klec, Christiane; Gottschalk, Benjamin; Bischof, Helmut et al. (2018): Real-Time Imaging of Mitochondrial ATP Dynamics Reveals the Metabolic Setting of Single Cells. In: Cell reports 25 (2), 501-512.e3. DOI: 10.1016/j.celrep.2018.09.027.

Duta-Mare, Madalina; Sachdev, Vinay; Leopold, Christina; Kolb, Dagmar; Vujic, Nemanja; Korbelius, Melanie et al. (2018): Lysosomal acid lipase regulates fatty acid channeling in brown

adipose tissue to maintain thermogenesis. In: Biochimica et biophysica acta. Molecular and cell biology of lipids 1863 (4), S. 467–478. DOI: 10.1016/j.bbalip.2018.01.011.

Eroglu, Emrah; Charoensin, Suphachai; Bischof, Helmut; Ramadani, Jeta; Gottschalk, Benjamin; Depaoli, Maria R. et al. (2018): Genetic biosensors for imaging nitric oxide in single cells. In: Free radical biology & medicine 128, S. 50–58. DOI: 10.1016/j.freeradbiomed.2018.01.027.

Eroglu, Emrah; Gottschalk, Benjamin; Charoensin, Suphachai; Blass, Sandra; Bischof, Helmut; Rost, Rene et al. (2016): Development of novel FP-based probes for live-cell imaging of nitric oxide dynamics. In: Nature communications 7, S. 10623. DOI: 10.1038/ncomms10623.

Eroglu, Emrah; Rost, Rene; Bischof, Helmut; Blass, Sandra; Schreilechner, Anna; Gottschalk, Benjamin et al. (2017): Application of Genetically Encoded Fluorescent Nitric Oxide (NO•) Probes, the geNOps, for Real-time Imaging of NO• Signals in Single Cells. In: Journal of visualized experiments: JoVE (121). DOI: 10.3791/55486.

Goeritzer, Madeleine; Vujic, Nemanja; Schlager, Stefanie; Chandak, Prakash G.; Korbelius, Melanie; Gottschalk, Benjamin et al. (2015): Active autophagy but not lipophagy in macrophages with defective lipolysis. In: Biochimica et biophysica acta 1851 (10), S. 1304–1316. DOI: 10.1016/j.bbalip.2015.06.005.

Klec, Christiane; Madreiter-Sokolowski, Corina T.; Stryeck, Sarah; Sachdev, Vinay; Duta-Mare, Madalina; Gottschalk, Benjamin et al. (2019): Glycogen Synthase Kinase 3 Beta Controls Presenilin-1-Mediated Endoplasmic Reticulum Ca^{2+} Leak Directed to Mitochondria in Pancreatic Islets and β-Cells. In: Cellular physiology and biochemistry: international journal of experimental cellular physiology, biochemistry, and pharmacology 52 (1), S. 57–75. DOI: 10.33594/000000005.

Klec, Christiane; Madreiter-Sokolowski, Corina T.; Ziomek, Gabriela; Stryeck, Sarah; Sachdev, Vinay; Duta-Mare, Madalina et al. (2019): Presenilin-1 Established ER-Ca^{2+} Leak: a Follow Up on Its Importance for the Initial Insulin Secretion in Pancreatic Islets and β-Cells upon Elevated Glucose. In: Cellular physiology and biochemistry: international journal of experimental cellular physiology, biochemistry, and pharmacology 53 (3), S. 573–586. DOI: 10.33594/000000158.

Korbelius, Melanie; Vujic, Nemanja; Sachdev, Vinay; Obrowsky, Sascha; Rainer, Silvia; Gottschalk, Benjamin et al. (2019): ATGL/CGI-58-Dependent Hydrolysis of a Lipid Storage Pool in Murine Enterocytes. In: Cell reports 28 (7), 1923-1934.e4. DOI: 10.1016/j.celrep.2019.07.030.

Lehmann, Martin; Gottschalk, Benjamin; Puchkov, Dmytro; Schmieder, Peter; Schwagerus, Sergej; Hackenberger, Christian P. R. et al. (2015): Multicolor Caged dSTORM Resolves the Ultrastructure of Synaptic Vesicles in the Brain. In: Angewandte Chemie (International ed. in English) 54 (45), S. 13230–13235. DOI: 10.1002/anie.201505138.

Madreiter-Sokolowski, Corina T.; Gottschalk, Benjamin; Parichatikanond, Warisara; Eroglu, Emrah; Klec, Christiane; Waldeck-Weiermair, Markus et al. (2016): Resveratrol Specifically Kills Cancer Cells by a Devastating Increase in the Ca^{2+} Coupling Between the Greatly Tethered Endoplasmic Reticulum and Mitochondria. In: Cellular physiology and biochemistry : international journal of experimental cellular physiology, biochemistry, and pharmacology 39 (4), S. 1404–1420. DOI: 10.1159/000447844.

Madreiter-Sokolowski, Corina T.; Klec, Christiane; Parichatikanond, Warisara; Stryeck, Sarah; Gottschalk, Benjamin; Pulido, Sergio et al. (2016): PRMT1-mediated methylation of MICU1 determines the UCP2/3 dependency of mitochondrial $Ca^{(2+)}$ uptake in immortalized cells. In: Nature communications 7, S. 12897. DOI: 10.1038/ncomms12897.

Madreiter-Sokolowski, Corina T.; Ramadani-Muja, Jeta; Ziomek, Gabriela; Burgstaller, Sandra; Bischof, Helmut; Koshenov, Zhanat et al. (2019): Tracking intra- and inter-organelle signaling of mitochondria. In: The FEBS journal 286 (22), S. 4378–4401. DOI: 10.1111/febs.15103.

Madreiter-Sokolowski, Corina T.; Waldeck-Weiermair, Markus; Bourguignon, Marie-Pierre; Villeneuve, Nicole; Gottschalk, Benjamin; Klec, Christiane et al. (2019): Enhanced inter-compartmental Ca^{2+} flux modulates mitochondrial metabolism and apoptotic threshold during aging. In: Redox biology 20, S. 458–466. DOI: 10.1016/j.redox.2018.11.003.

Waldeck-Weiermair, Markus; Bischof, Helmut; Blass, Sandra; Deak, Andras T.; Klec, Christiane; Graier, Thomas et al. (2015): Generation of Red-Shifted Cameleons for Imaging

Ca^{2+} Dynamics of the Endoplasmic Reticulum. In: Sensors (Basel, Switzerland) 15 (6), S. 13052–13068. DOI: 10.3390/s150613052.

Waldeck-Weiermair, Markus; Gottschalk, Benjamin; Madreiter-Sokolowski, Corina T.; Ramadani-Muja, Jeta; Ziomek, Gabriela; Klec, Christiane et al. (2019): Development and Application of Sub-Mitochondrial Targeted Ca^{2+} Biosensors. In: Frontiers in cellular neuroscience 13, S. 449. DOI: 10.3389/fncel.2019.00449.

Waldeck-Weiermair, Markus; Malli, Roland; Parichatikanond, Warisara; Gottschalk, Benjamin; Madreiter-Sokolowski, Corina T.; Klec, Christiane et al. (2015): Rearrangement of MICU1 multimers for activation of MCU is solely controlled by cytosolic $Ca^{(2+)}$. In: Scientific reports 5, S. 15602. DOI: 10.1038/srep15602.

Acknowledgements

As a PhD student, I received funding from the Austrian Science Fund (FWF) (DK-MCD W1226 (to WFG)) and Nikon Instruments within the framework of the Nikon Excellence Center Graz, and BioTechMed.

Danksagung

Zu aller erst möchte ich meiner Familie danken, die mir stets Rückhalt gab, mich ermutigte, bestärke und mich auf meinem Weg unterstützt hat. Meine Großeltern Ilse und Günter Gottschalk sowie meine Mutter Ute Gottschalk-Krimlowski und ihr Mann Kai Uwe Gottschalk-Krimlowski haben mir immer zur Seite gestanden, mich gestützt und angespornt.

Auch bei meinen großartigen Kollegen möchte ich mich bedanken. Die fünf Jahre mit ihnen sind wie im Flug vergangen. Ob nun eine fachliche Diskussionen, ein gemütlicher Abend oder eine Runde „wutzeln“, es war mir immer eine große Freude mit ihnen zu arbeiten, zu feiern und einfach eine großartige Zeit zu verbringen.

Insbesondere möchte ich Christiane, Corina, Maria, Markus und René danken mit denen ich einen Großteil meiner PhD-Zeit verbracht habe. Sie haben mir unter die Arme gegriffen wenn möglich, mich aufgebaut wenn nötig und meinen Laboralltag und Leben enorm bereichert.

Meiner Partnerin Snjezana Radulovic gilt ebenfalls ein besonderer Dank. Nicht nur für ihre aufopfernde Geduld, ihr großes Verständnis sondern auch für ihre wertvolle fachliche Hilfe und Unterstützung während meines PhD-Studiums.

Ebenfalls danke ich den Mitgliedern meines Dissertations-Komitees Roland Malli und Klaus Groschner für ihre Unterstützung und wissenschaftliche Begleitung während meines PhD-Studiums.

Zu guter Letzt möchte ich mich auch ganz herzlich bei meinem Chef und Supervisor Wolfgang Graier bedanken. Er hat mir immer sehr geduldig mit Rat und Tat zur Seite gestanden, mich auf meinem Weg unterstützt und mit seiner großen wissenschaftlichen Leidenschaft und Fachkenntnis ein echtes Vorbild geliefert dem ich nachstreben möchte.

Table of contents

Abbreviations

2CaB	$2Ca^{2+}$- buffer
AR	Aspect ratio
ATP	Adenosine triphosphate
Bp	Base pair
BSA	Bovine serum albumin
CaMKI	Calmodulin-dependent protein kinase I
Cas9	CRISPR associated protein 9
CFP	Cyan fluorescent protein
CJ	Cristae junction
CM	Cristae membrane
Co-IP	Co-immunoprecipitation
DMEM	Dulbecco's modified eagle's medium
DRP1	Dynamin related protein 1
dSTORM	Direct STORM
EF-hand	Helix-loop-helix structural domain
EMRE	Essential MCU regulator
ER	Endoplasmic reticulum
FCS	Fetal calf serum
FF	Form factor
FP	Fluorescent protein
FRET	Förster resonance energy transfer
FWHM	Full width at half maximum
GAPDH	Glyceraldehyde 3-phosphate dehydrogenase
GFP	Green fluorescent protein
GRP75	75 kDa glucose-regulated protein
IBM	Inner boundary membrane
IgG	Immunoglobulin G
IMM	Inner mitochondrial membrane
IP_3	Inositol triphosphate
KO	genetical knock out
L-OPA1	Long isoform of OPA1
MAM	Mitochondria-associated ER membranes
mCherry	Red fluorescent protein
MCU	Mitochondrial Ca^{2+} uniporter
MCUb	dominant negative pore-forming subunit of the MCU-complex
MCU-complex	Mitochondrial Ca^{2+} uniporter complex
MCUR1	Mitochondrial calcium uniporter regulator 1
MFN1	Mitofusin 1
MFN2	Mitofusin 2
MICOS	Mitochondrial contact site complex

MICU1	Mitochondrial calcium uptake 1
MICU2	Mitochondrial calcium uptake 2
MICU3	Mitochondrial calcium uptake 3
MIRO1/2	Mitochondrial Rho GTPase 1/2
MTG	MitoTracker™ Green FM
MTR	MitoTracker™ Red FM
MTR-CMX	MitoTracker™ Red CMXRos
NA	Numerical aperture
NL-SIM	Non-linear SIM
OMA1	Metalloendopeptidase
OMM	Outer mitochondrial membrane
OPA1	Optic atrophy 1
PALM	Photo activated localization microscopy
PBS	Phosphate buffered saline
PCR	Polymerase chain reaction
PFA	Paraformaldehyde
PRMT1	Protein arginine N-methyltransferase 1
PVDF membrane	polyvinylidene difluoride membrane
qRT-PCR	quantitative real time polymerase chain reaction
RFP	Red fluorescent protein
ROS	Reactive oxygen species
RT	Room temperature
SD	Standard deviation
SDS-PAGE	sodium dodecyl sulfate polyacrylamide gel electrophoresis
SEM	Standard error of the mean
SIM	Structured illumination microscopy
SLM	Spatial light modulators
SMLM	Single molecule localization microscopy
S-OPA	Short isoform of OPA1
STED	Stimulated emission depletion
STORM	Stochastic optical reconstruction microscopy
TMRM	Tetramethylrhodamine
TOM22	Translocase of the outer membrane 22
TRAK1/2	Trafficking protein, kinesin binding 1/2
UCP2	Uncoupling protein 2
UCP3	Uncoupling protein 3
UCP4	Uncoupling protein 4
VDAC	Voltage-dependent anion-selective channel 1
Wt	Wild type
YFP	Yellow fluorescent protein
YME1L	i-AAA protease

Abstract

Mitochondria are multifunctional organelles that essentially contribute to cell signaling by sophisticated mechanisms of communication. Morphological and structural properties of mitochondria often correlate with cellular functions and *vice versa*. Ca^{2+} plays an essential role as secondary messenger to transfer inter- and extracellular signals that modulate in particular mitochondrial shape, metabolism or stress response. Mitochondrial morphology was observed either in fixed cells with great spatial resolution using electron microscopy, or in living cells using fluorescence imaging approaches. Structured illumination microscopy (SIM) allows a compromise of both techniques combining enhanced spatial resolution compared to conventional fluorescence microscopy and the ability to observe dynamic processes in living cells. In this work two particular aspects of mitochondrial structure and function in relation to Ca^{2+} signaling were investigated: **1)** The dynamics of the inner mitochondrial membrane (IMM) were quantified to investigate the influence of IP_3-mediated endoplasmic reticulum (ER)-Ca^{2+} release on the sub-mitochondrial membrane organization. Dual-color SIM was used to quantitatively analyse cristae membrane (CM) dynamics in close proximity to mitochondria-associated ER membranes (MAMs). CM kinetics were spatially confined in MAMs by intracellular Ca^{2+} release independent of mitochondrial matrix Ca^{2+} signals. **2)** Ca^{2+} movement across the IMM is strictly regulated by the mitochondrial Ca^{2+} uniporter complex (MCU-complex), which consists of multiple proteins like the pore forming mitochondrial Ca^{2+} uniporter (MCU), EMRE (an essential MCU regulator) and the Ca^{2+} gatekeeper MICU1 (mitochondrial Ca^{2+} uptake 1). Using SIM, MICU1 was found to localize at the inner boundary membrane (IBM) guarding mitochondria under resting conditions against Ca^{2+} overload, loss of membrane potential and cytochrome c release by cristae junction (CJ) stabilization. Upon intracellular Ca^{2+} elevation MICU1 functions as a Ca^{2+} dependent diffusion trap for MCU and EMRE, assembling the MCU-complex at the IBM to potentially increase Ca^{2+} uptake efficacy. Both aspects show how the interplay of structure and function of the mitochondrial membrane framework, dynamic sub-mitochondrial protein localization and Ca^{2+} signaling influence and regulate essential cellular processes.

Zusammenfassung

Mitochondrien sind multifunktionale Organellen, die durch ausgeklügelte Kommunikationsmechanismen wesentlich zur Signalverarbeitung der Zellen beitragen. Morphologische und strukturelle Eigenschaften von Mitochondrien korrelieren häufig mit zellulären Funktionen und umgekehrt. Als sekundärer Botenstoff spielt Ca^{2+} eine wesentliche Rolle für die Übertragung inter- und extrazellulärer Signale, die insbesondere die Morphologie von Mitochondrien sowie deren Metabolismus und Stressreaktion modulieren. Die mitochondriale Morphologie wurde entweder in fixierten Zellen mit hoher räumlicher Auflösung durch Elektronenmikroskopie oder in lebenden Zellen über Fluoreszenzbildgebungsansätze beobachtet. Strukturierte Beleuchtungsmikroskopie (SIM) ermöglicht einen Kompromiss zwischen beiden Techniken, der eine verbesserte räumliche Auflösung im Vergleich zur konventionellen Fluoreszenzmikroskopie und die Fähigkeit zur Beobachtung dynamischer Prozesse in lebenden Zellen ermöglicht. In dieser Arbeit wurden zwei spezielle Aspekte der mitochondrialen Struktur und Funktion im Zusammenhang mit Ca^{2+}-Signalen untersucht: 1) Die Dynamik der inneren Mitochondrienmembran (IMM) wurde quantifiziert, um den Einfluss von IP_3-vermittelter Ca^{2+}-Freisetzung aus dem endoplasmatischem Retikulum (ER) auf die submitochondriale Membranorganisation zu untersuchen. Zweifarbiges SIM wurde verwendet, um die Dynamik der Cristae-Membran (CM) in unmittelbarer Nähe Mitochondrien-assoziierter ER-Membranen (MAMs) quantitativ zu analysieren. Die CM-Kinetik wurde in MAMs durch intrazelluläre Ca^{2+}-Freisetzung räumlich reduziert, während sie von Ca^{2+} Signalen der mitochondrialen Matrix unabhängig war. 2) Die Ca^{2+}-Bewegung durch die IMM wird streng durch den mitochondrialen Ca^{2+}-Transporter-Komplex (MCU-Komplex) reguliert, der aus mehreren Proteinen besteht, wie dem porenbildenden mitochondrialen Ca^{2+}-Uniporter (MCU), EMRE (essentieller MCU-Regulator) und dem Ca^{2+}-Wächter MICU1 (mitochondriale Ca^{2+} Aufnahme 1). Es wurde festgestellt, dass sich MICU1 an der inneren Grenzmembran (IBM) befindet und Mitochondrien unter Ruhebedingungen vor Ca^{2+}-Überlastung, Verlust des Membranpotentials und Freisetzung von Zytochrom C durch Stabilisierung der Cristae schützt. Infolge intrazellulärer Ca^{2+}-Erhöhung fungiert MICU1 als Ca^{2+}-abhängige Diffusionsfalle für MCU und EMRE und assembliert den MCU-Komplex an der IBM, um möglicherweise die Ca^{2+}-

Aufnahmeeffektivität zu erhöhen. Beide Aspekte zeigen, wie das Zusammenspiel von Struktur und Funktion des mitochondrialen Membrangerüsts, die dynamische submitochondriale Proteinlokalisation und die Ca^{2+}-Signalübertragung wesentliche zelluläre Prozesse beeinflussen und regulieren.

1 Introduction

1.1 **Mitochondrial Ca^{2+} signaling**

Mitochondria are multifunctional organelles that essentially contribute to cell signaling by sophisticated mechanisms of communication whereby Ca^{2+} uptake represents one of the most important processes involved[1,2]. Biochemical signals moving bidirectionally in and out of the organelle have to pass the inner (IMM) and outer mitochondrial membrane (OMM). Ca^{2+} signaling has been studied extensively due to its major regulatory effect on mitochondrial metabolic activity or cell death initiation[3], thus, determining the cellular fate. Ca^{2+} diffusion across the OMM is quite unrestricted due to the open VDAC conformation, while the Ca^{2+} flux through the IMM is strictly regulated and carried out by the mitochondrial Ca^{2+} uniporter complex (MCU-complex)[3,4]. MCU (mitochondrial Ca^{2+} uniporter) [5,6] and EMRE (an essential MCU regulator)[7] are the two pore forming proteins of the MCU-complex accompanied by the dominant-negative pore-forming subunit MCUb[8] and a scaffolding factor (MCUR1; mitochondrial calcium uniporter regulator 1)[9].

The permeability of the MCU-complex is regulated and controlled by the IMS proteins MICU1 (mitochondrial calcium uptake 1)[10] and its paralog MICU2[10]. MICU1 is an IMS located[11] EF-hand (helix-loop-helix structural domain) Ca^{2+} binding protein and acts as a gatekeeper of MCU by inhibiting mitochondrial Ca^{2+} influx at low resting cytosolic Ca^{2+} concentrations while it facilitates mitochondrial Ca^{2+} uptake upon high Ca^{2+} concentrations [9]. Recently it was shown that the rearrangement of MICU1 multimers, which is necessary for activation of MCU, is controlled by cytosolic Ca^{2+}[12]. EMRE governs the MCU channel activity by sensing mitochondrial matrix Ca^{2+} levels and thereby blocking mitochondrial Ca^{2+} influx at resting cytosolic Ca^{2+} concentrations while opening MCU channels at low matrix Ca^{2+}[13]. The interplay of EMRE and MICU1 protects mitochondria from Ca^{2+} depletion by maintaining matrix Ca^{2+}

concentration as well as Ca^{2+} overload under resting conditions while enabling dynamic mitochondrial Ca^{2+} signaling[13].

Recently, arginine M-methyltransferase 1 (PRMT1) and Uncoupling protein 2 (UCP2) were identified as important regulators of the MCU-complex [14]. PRMT1 methylates MICU1 and desensitizes it to Ca^{2+} thereby inhibiting mitochondrial matrix Ca^{2+} uptake. UCP2 binds specifically to methylated MICU1 and re-sensitizes it to Ca^{2+} binding, thus, recovering mitochondrial Ca^{2+} uptake[14]. In addition to the regulation of MICU1 by PRMT1 methylation, phosphorylation of the N-terminal region of MICU1 by mitochondrion-targeted AKT increases basal mitochondrial matrix Ca^{2+} levels and impairs processing and stability of MICU1[11]. The regulation of the MCU-complex is further based on the stoichiometry of MCU, MICU1 and MICU2. Different ratios between single components of the MCU-complex in different tissues (e.g. heart, liver, skeletal muscle) are directly related to the Ca^{2+} uptake capacities and kinetics[15]. Not only the ratio but also the strength of interaction between subunits of the MCU-complex is important for Ca^{2+} uptake regulation. The essential oxidoreductase MIA40 was shown to dimerize disulfide dependent MICU1 and MICU2 to a heterodimer. Blocking dimerization increases Ca^{2+} uptake showing that hetero- or homo-dimerization of MICU1/MICU2 plays an important role for mitochondrial Ca^{2+} regulation[16]. MICU2 in general was shown to have an inhibitory effect on MCU Ca^{2+} permeability, but in an MICU1 dependent manner. MICU1 is essential for MICU2 influence on MCU pointing to a non-redundant functionality of both proteins[17]. Another homolog of MICU1 is MICU3. MICU3 is predominantly expressed in the brain and is able to form heterodimers with MICU1 like MICU2. In contrast to MICU2, MICU3 enhances mitochondrial Ca^{2+} uptake in HeLa and HEK cells when overexpressed[18]. Pull-down assays have shown that MICU1 can bind directly to MCU or EMRE. MICU1 was predicted to have a transmembrane domain and was resistant to carbonyl extraction, indicating that MICU1 is an integral membrane protein[19]. Nevertheless, experimental proof is missing. Kamer et al. showed that MICU1 binds independent of the presence of Ca^{2+} to cardiolipin, a phospholipid with high occurrence within the IMM and OMM[20]. While MICU1 binding to MCU is believed to be mediated by EMRE[7,21], direct binding

of MICU1 to MCU was verified as well[22]. Additionally, expression of EMRE mutants lacking the CAD (C-terminus acidic domain) and thus the ability to bind to MICU1 did not change the mitochondrial Ca^{2+} uptake capacity, indicating that the MICU1-EMRE interaction is dispensable for MCU activity and regulation[21].

1.2 Inner boundary membrane, cristae membrane and cristae junction biogenesis

Unlike the OMM, the IMM is morphologically separated into two compartments divided by the cristae junction (CJ); the inner boundary membrane (IBM) directly facing the inner leaflet of the OMM, and the cristae membrane (CM) forming the protrusions and invaginations of the IMM into the mitochondrial matrix[23–25].

Notably, distinct localizations of proteins in the CM and IBM were demonstrated for the F_0F_1-ATP synthase, electron transport chain subunits[26,27] and TIM-proteins[25], respectively. Remarkably, spatial distributions of proteins that form the MCU-complex have not been previously examined.

Beside the effects of OPA1 on the fission and fusion balance of the mitochondrial network, OPA1 is also strongly involved in cytochrome c release into the cytosol and induction of apoptosis. The balance of OPA1-L and -S form oligomers was shown to correlate with the tightness of the cristae junction[28,29]. While the reduction of OPA1 expression via siRNA leads to drastic disorganization of the cristae[30–32], complete loss of OPA1 leads to perturbation of the inner mitochondrial membrane and results in apoptosis [33]. Cristae shape, respiratory chain supercomplexes, complex-I-dependent respiration, and respiratory growth are impaired after OPA1 depletion [34].

1.3 Endoplasmic reticulum related mitochondria-associated membranes (MAM)

Contact sides between mitochondria and the endoplasmic reticulum (ER), so called mitochondria-associated membranes (MAM), play an important role in signal transduction and Ca^{2+} signaling [35,36]. ER and mitochondria are bound closely to each other by inter-organelle tethers formed by different proteins like mitofusin 2 or the IP3 receptor-GRP75-VDAC complex (GRP75 (75 kDa glucose-regulated protein); VDAC (voltage-dependent anion channels))[1,37]. The close proximity of both organelles enables efficient Ca^{2+} transfer after e.g. inositol-3-phosphat (IP_3) mobilization and subsequent ER Ca^{2+} efflux [36]. Furthermore, mitochondrial movement along microtubules is regulated by MIRO1/2 (Mitochondrial Rho GTPase 1/2) which are associated with MAMs. Both proteins function as anchors for TRAK1/2 (Trafficking Protein, Kinesin Binding 1/2) which bind the microtubule motor proteins kinesin and dynein. Binding of Ca^{2+} to the MIRO1/2 EF-hand motive inhibits interaction to TRAK1/2 and prevents mitochondrial transport along the microtubules leading to a mitochondrial movement arrest[38,39].

1.4 Mitochondrial fission and fusion machinery

The balancing of mitochondrial fission and fusion plays a critical role in maintaining the mitochondrial integrity and participates in the high dynamic adaption of mitochondria to meet metabolic needs and respond to internal and external stress and survival signaling. The fusion and fission homeostasis is highly correlated with the opening probability of the permeability transition pore[40], oxidative capacity[34,41], ROS (reactive oxygen species)-production[42], mitophagy[43], apoptosis [28,44], calcium signaling[35,44–47] and mitochondrial interaction sites with other cell compartments[48–50].

Mitochondrial fission is mainly mediated by the cytosolic dynamin-related protein 1 (DRP1). After binding to the OMM it constricts the mitochondrion by its GTPase activity [51]. Binding of DRP1 is facilitated after ER-Ca^{2+} release via calcineurin and Ca^{2+}/calmodulin-dependent protein kinase I (CaMKI)[52]. Since DRP 1 is leading only to a constriction but not cleavage of

the mitochondrion, the dynamin GTPase is needed for complete fission of mitochondria[53,53,54]. So far it is not known whether a dedicated machinery is needed for IMM cleavage during the fission process.

Mitofusin 1 and 2 (MFN1 and MFN2) and Optic atrophy 1 (OPA1) are the main regulators facilitating fusion of the OMM and IMM, respectively[31,55,56]. The GTPase activity of MFN1 delivers the necessary force to fuse the OMM of two neighboring mitochondria[57]. OPA1 is the IMM analog to the OMM located MFN1 and MFN2[58]. Two forms of OPA1 (L-OPA1 and S-OPA) are kept in balance by the proteases OMA1 and YME1L by proteolytic cleavage of the IMM bound L-OPA1 to soluble S-OPA1[59,60]. In case of a predominance of the L-form, mitochondria form a complex network, but metabolic or cell stress signals activate YME1L and OMA1 leading to L-OPA1 proteolytic cleavage and a decreased fission activity, resulting in fragmented mitochondria [59,60].

1.5 **Sub-mitochondrial localization of proteins and function correlation**

The division of the mitochondrial membrane framework into OMM, IBM and CM, the latter separated by the CJ, enables complex but efficient function of proteins located specifically in one of these compartments. The F_1F_0-ATPase as well as the respiratory chain complexes I, III, and IV are located to the CM with very low abundance in the IBM[25–27,61]. The uncoupling protein UCP4 on the other side is localized predominantly in the IBM[61]. Klotzsch et al. concluded that the CM localization of the F_1F_0-ATPase facilitates a high degree of efficiency caused by the closed cristae lumen compartment. Overactivity of the electron transport chain could be buffered by a proton flow thought the CJ reaching IBM located UCP4 which in turn uncouples the proton gradient locally[61]. While the translocase of the outer membrane (TOM) complex resides at the OMM, the translocase of the inner membrane (TIM) can be found mainly at the IBM[25]. While no clear mechanism is known how the localization of TIM proteins is maintained at the IBM, it is predicted that proteins which are imported by the TOM complex into the IMS are directly translocated into the mitochondrial matrix by TIM. In this way the translocated protein peptide chain acts as a linker of TOM and TIM[62]

1.6 Surpassing the diffraction limit with super-resolution fluorescence microscopy

Fluorescence light microscopy is mainly limited regarding the spatial resolution in x, y and z dimensions by the wavelength of light used (λ_{light}) and the numerical aperture (NA) of the objective. The NA is determined by the refractive index and α is the half maximum angle of the light that is collected by the optical system. This physical limitation is called the diffraction barrier (Figure 1).

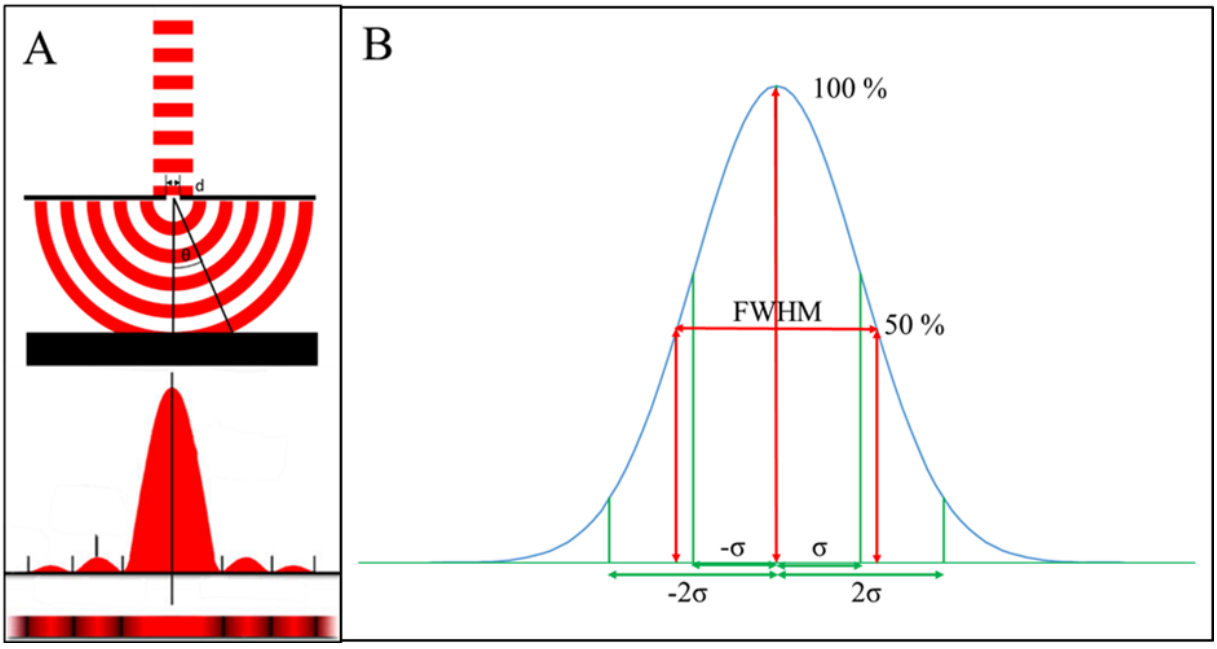

Figure 1 ***Appearance of diffraction pattern.*** *(A) After passing an aperture light is dispersed in a radial pattern. By constructive and destructive interference a Point spread function (PSF) is observed. (B) PSF can be simplified to a Gaussian function with associated standard deviation (σ). Additionally, the full width of half maximum (FWHM) is included which is taken mainly to determine a resolution of a system.*

In general, the resolution limit can be calculated[63] in x/y and z with the following simple equations:

$$d_{x/y} = \frac{\lambda_{light}}{2n \sin\alpha} = \frac{\lambda_{light}}{2NA}$$

$$d_z = \frac{\lambda_{light}}{n (\sin\alpha)^2}$$

The generally achievable resolution of fluorescence microscopes is approximately 200 nm in the lateral and 600 nm in axial dimension. Cellular structure soften surpass the size limits of conventional fluorescence microscopy. Super-resolution techniques based on fluorescence microscopy were developed to circumvent the physical laws of optical physics and increase the spatial resolution.

1.6.1 Structured illumination microscopy (SIM)

Several recently introduced super-resolution fluorescence imaging methods substantially surpass the diffraction limit. Structured illumination microscopy (SIM) uses a grid pattern which is shifted and rotated to illuminate the sample plane. By analyzing the Moiré pattern additional information can be extracted and thereby the Abbe diffraction limit surpassed by 2-fold (Figure 2)[64,65].

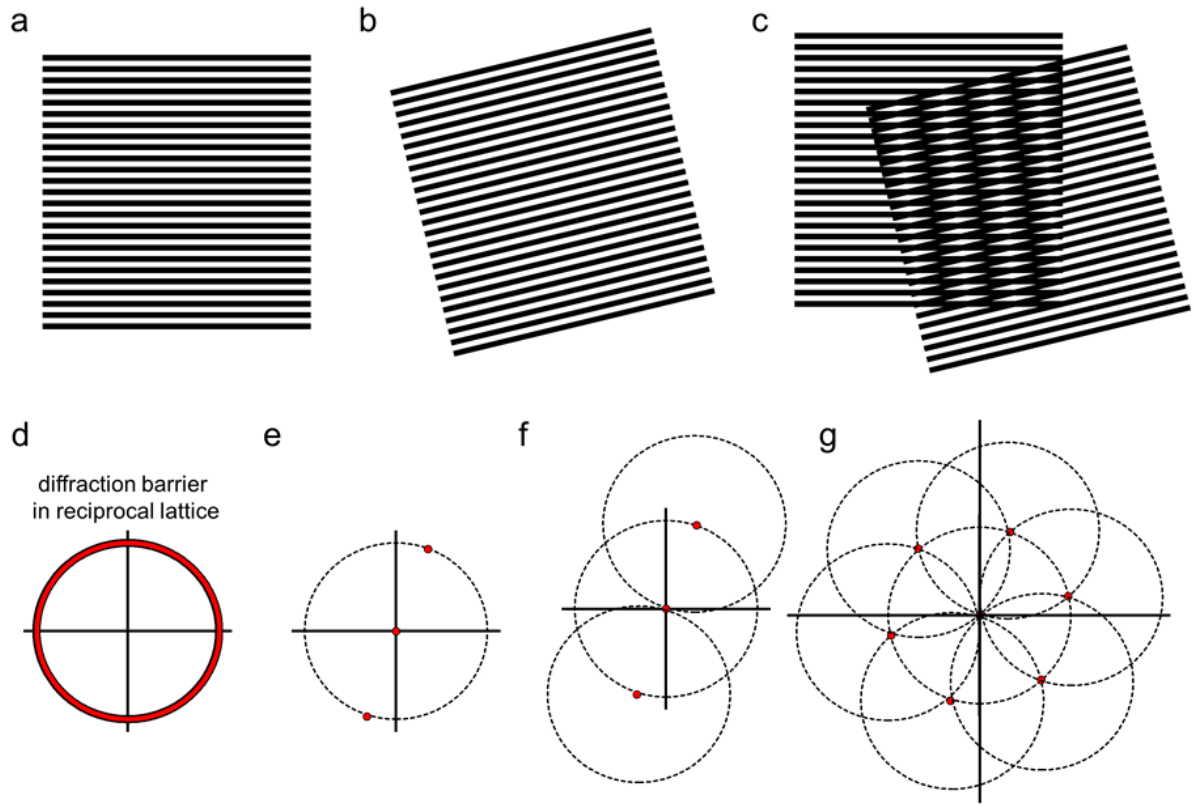

Figure 2: ***Enhancing the resolution with structured illumination.*** *(a) Line pattern representing the sample. (b) Line pattern representing the sigmoidal structured illumination. (c) Superposing both line patterns of (a) and (b) results in moiré fringes apparent as vertical stripes. (d) Converting any image into its reciprocal space using a Fourier transformation results in area, limited by the resolution of that image (in microscopically optics the Abbe diffraction barrier). (e) The sinusoidal line patterns only has three Fourier components whose locations are limited by the diffraction barrier in reciprocal space. (f) The overlap of the sample and the structured illumination pattern with results in moiré fringes inheriting information with higher frequencies and changed position in reciprocal space. (g) By using different angles and phases (7-9 orientations in total) of the structured illumination, information of an area twice the radius of the former diffraction limited area can be obtained and thereby double the resolution of the resulting image after reconversion form the reciprocal space into the real space.*

To generate the sinusoidal stripe pattern needed for structured illumination microscopy several techniques are available. In general, the interferences of two or more laser beams are used to generate structured patterns [66,67]. These laser beams are often created, like in the Nikon system used in this study (Figure 3), by diffracting light into +1, 0 and -1 order beams [68]. Rigid gratings are replaced continually by spatial light modulators (SLM). As no moving parts are needed higher acquisition rates and better system stability are the clear benefits of SLMs[69–72].

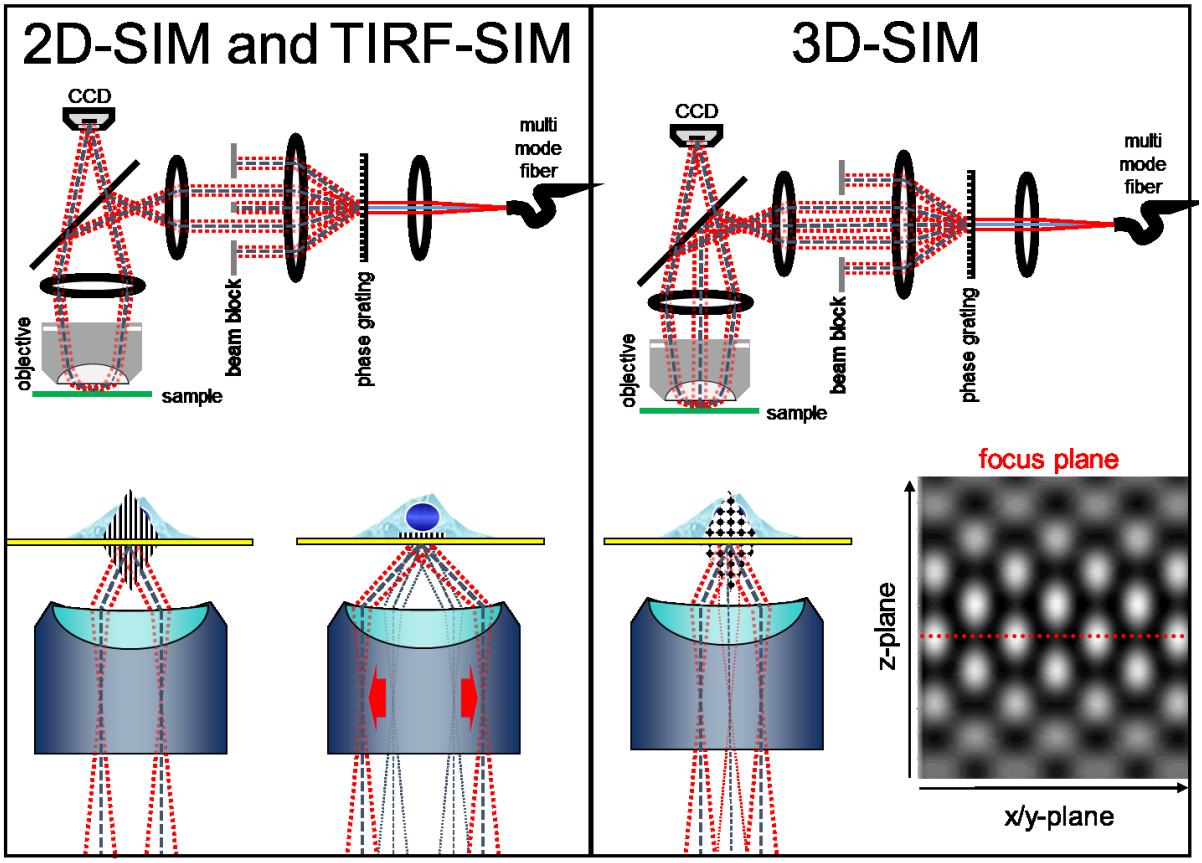

Figure 3: ***Generating the sinusoidal stripe pattern with Nikon-SIM.*** *(Left panel) The laser is coupled by a multi-mode fiber into a phase grating. For 2D-SIM the grating creates interference pattern and the +1 and -1 order are projected into the sample. At the sample plane +1 and -1 order light rays interfere with each other to create a sinusoidal stripe pattern projected into the focus plane to illuminate the sample. In case of TIRF SIM the +2 and -2 orders are projected in a wider angel into the focus plane generating the needed stripe pattern as an evanescent field. (Right panel) In order to increase the z resolution the +1, 0 and -1 orders are brought to interfere in the sample plane generating a not only a 2D stripe pattern but expanding to a 3D bar pattern.*

Using SIM microscopy yields a double in spatial resolution in x,y-plane as well as in z (Figure 4). In theory, the concept of SIM does not have a limit in spatial resolution. In non-linear SIM (NL-SIM) the illumination pattern consists of multiple spatial frequencies mixing with underlying sample information. During the reconstruction process with this additional information the resolution can be enhanced even further [64]. The drawback of this method originates from the additional spatial illumination frequencies which increase the number of phases and angles dramatically. Achieving a resolution of approximately 50 nm requires already 63 images [64].

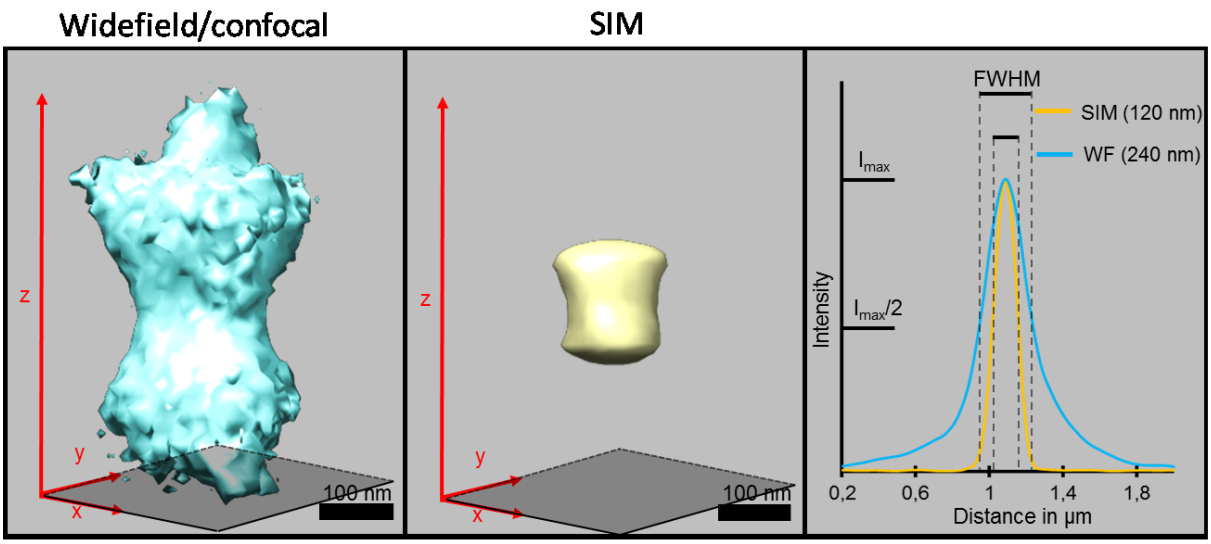

Figure 4: ***Increase of resolution by SIM microscopy visualized on 100 nm fluorescent beads.*** *A Tetraspek bead with a size of 100 nm was imaged with wide field (left panel) and SIM microscopy (middle panel) with 488 nm excitation in 60 nm z-increments. On the left to typical point spread function of the microscopic setup is visible. This point spread function is not only reduced in x,y and z by 2-fold (right panel), but also the out of focus fluorescence in z is minimized.*

1.6.2 Stochastic optical reconstruction microscopy (STORM)

Within the family of fluorescence super-resolution microscopy techniques STORM or single molecule localization microscopy (SMLM) represents the approach with the highest spatial resolution. Single fluorescent emitters are isolated and imaged followed by fitting their signals to their point spread function. The fitting process yields x and y coordinates which are extracted and plotted into an empty image frame. By repeating this process 500,000 - 2,000,000 times a super-resolved image can be created based on the extracted x and y coordinates (Figure 5).

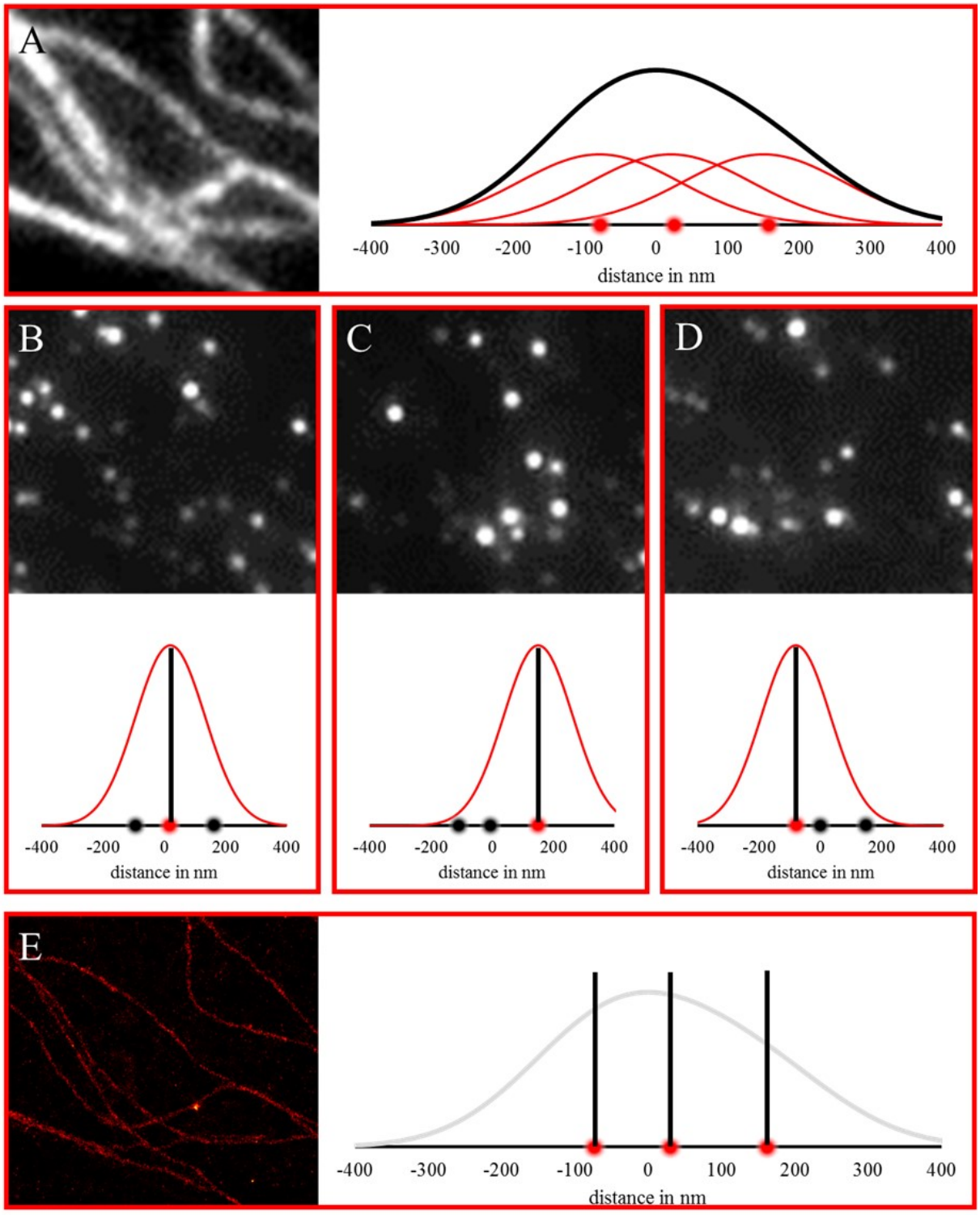

Figure 5: ***Principle of stochastic readout techniques.*** *(A) EPI-fluorescence image of immunostained microtubules with superimposed PSFs of multiple fluorophores. (B), (C), and (D) show images of single and isolated fluorophore signals which can be fitted to a Gaussian distribution. The peaks of these fits were rendered into a new image (E). A super-resolved image, where the resolution is limited to the Gaussian fit accuracy, is generated.*

For isolation of fluorescent emitters, several techniques are available. STORM microscopy was first introduced in 2006 by Rust et al [73]. Cyanine based fluorophores Cy3 and Cy5 were used

to co-label biological samples. First, all Cy5 molecules are switched to an off state by a strong red laser pulse. A green laser pulse is used to excite Cy3, which in turn transfers energy to Cy5 to bring it back to the on state. As the conversion from the off to the on state is easily adjustable by tuning the green light intensity, the amount of on state Cy5 can be limited to an amount in which the PSFs are not overlapping [73]. Direct STORM (dSTORM) uses conventional fluorophores in a reducing buffer containing 100 mM mercaptoethanolamine (MEA). The thiol-group binds to the excited state of the fluorophore and transfers it into an off state. Using UV light, the bond between the thiol group and the fluorophore can be broken and transferred back into the on-state [74]. This technique brings two major advances. First, by removing the green light for activation a second channel for multicolor imaging is available and, second, a broad range of fluorophores can be used with this technic [75]. While STORM and dSTORM achieve lateral resolution of approximately 10-20 nm, cagedSTORM reaches up to 1 nm x/y resolution. The resolution of single molecule localization microscopy depends mainly of the number of photons emitted by a single fluorophore per activation event. The more information collected the better the PSF or Gaussian fitting algorithm can estimate the precise localization. Vaughan et al. used a chemical procedure for caging (quenching) fluorophores with sodium borohydride ($NaBH_4$)[76]. UV-light was used to recover the off-state dyes into an on-state. By using a very efficient oxygen scavenging system composed of glucose oxidase and catalase and a redox system holding the fluorophore for long time in the on-state after UV-activation protecting from photo bleaching, up 1.7 million photons can be collected per activation event compared to 10,000 - 20,000 photons achieved with STORM or dSTORM[76] (Figure 6). Later, Lehmann et al. extended the range of suitable fluorophores for cagedSTORM for multicolor usage and were able to detect single synaptic vesicles in ultrathin sections of mouse hippocampal tissue [77].

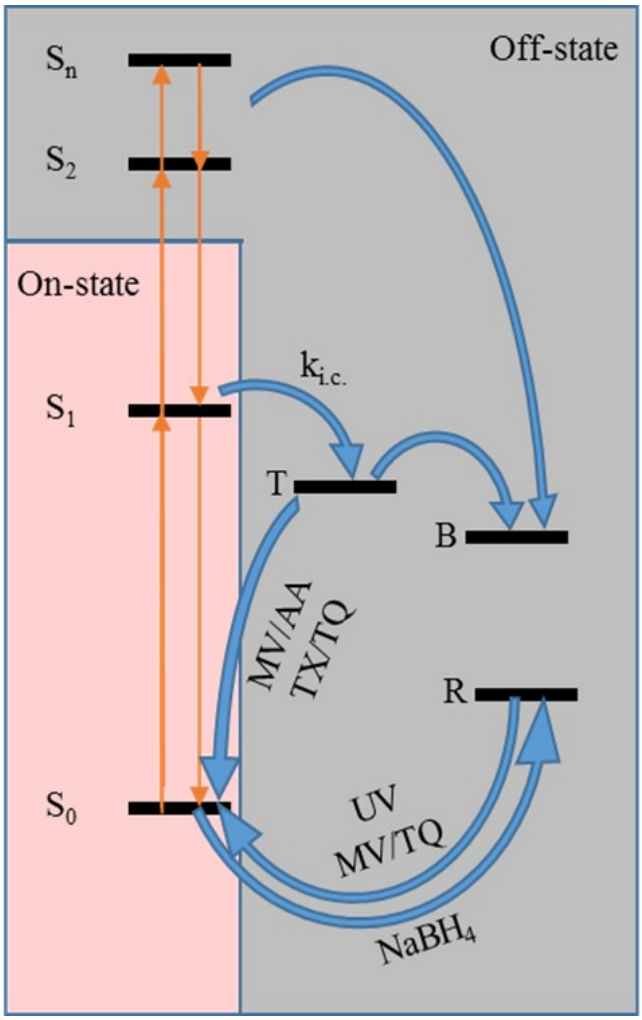

Figure 6: ***The fluorophore On/Off-States for cagedSTORM****. Fluorescence is emitted by alternating ground (S_0) and first exited states (S_1). $NaBH_4$-caging of fluorophores leads to a reduced off-state (R) which can be reversed to the on-state by UV-light or oxidative agents like methyl viologen (MV) or trolox-quinone (TQ). During excitation internal conversation ($k_{i.c.}$) leads to triplet off-state (T) formation. The triplet state can lead to photo bleaching (B) due to its high reactivity. Triplet state quencher like methyl viologen (MV), ascorbic acid (AA), trolox (TX), and trolox-quinone (TQ) are capable to transfer the fluorophore back to the ground state. Adsorption of multi-photons or higher energy photons of blue light can lead to higher excited state (S_{2-n}). These can lead to photo bleaching likewise the triplet state or are transferred back to first the excited or ground state by radiative or non-radiative relaxation.*

While having superior resolution above other super-resolution technics STORM, dSTORM and cagedSTORM are not suitable for live cell imaging because of antibody labeling or harsh buffer conditions. Photo activated localization microscopy (PALM) uses photo-convertible fluorescent proteins which can be specifically targeted in living cells. Fluorescent proteins like PA-GFP, Dronpa, Kaede, Kikume Green-Red or Eos can be used instead of chemical dyes and achieve resolutions of up to 20 nm[78].

1.6.3 Stimulated emission depletion microscopy (STED)

To circumvent the limitation of optical resolution based on the point spread function of optical systems, Hell and Wichmann introduced already 1994 the principles of stimulated emission depletion fluorescence microscopy [79]. The principle is based on the fact that during the excitation of a fluorophore a valence electron is raised form its ground state (S_0) to its excited state (S_1). More precisely from L_0 to L_1 as indicated in Figure 7 . By vibrational relaxation the electron loses some energy and falls back to state L_2. Under normal conditions the electron is now relaxing back to the ground state L_0 accompanied by light emission. In case of a strong excitation with a laser beam (STED-laser) matching with its wavelength the energy needed for a relaxation form L_2 into L_3 the electron is forced by the energy resonance of the STED laser to fall back into L_3 instead of L_0. L_3 is further transformed by vibrational relaxation back into L_0 (Figure 7) [79,80].

That general principle can be applied to fluorescence microscopy. By illuminating the microscopical sample with an excitation beam using a confocal laser scanning microscope the fluorophores are excited within the point spread function of the optical system. A secondary donut shaped STED laser, generated by a 2π phase plate, is targeted on the same position [81]. The STED laser is actively canceling out the fluorescence generated by the excitation laser and thereby reshaping and narrowing the PSF of the emitted photons of the sample (Figure 7). Using this technique the effective resolution of approximately 200 nm can by reduced dramatically to less than 50 nm [81].

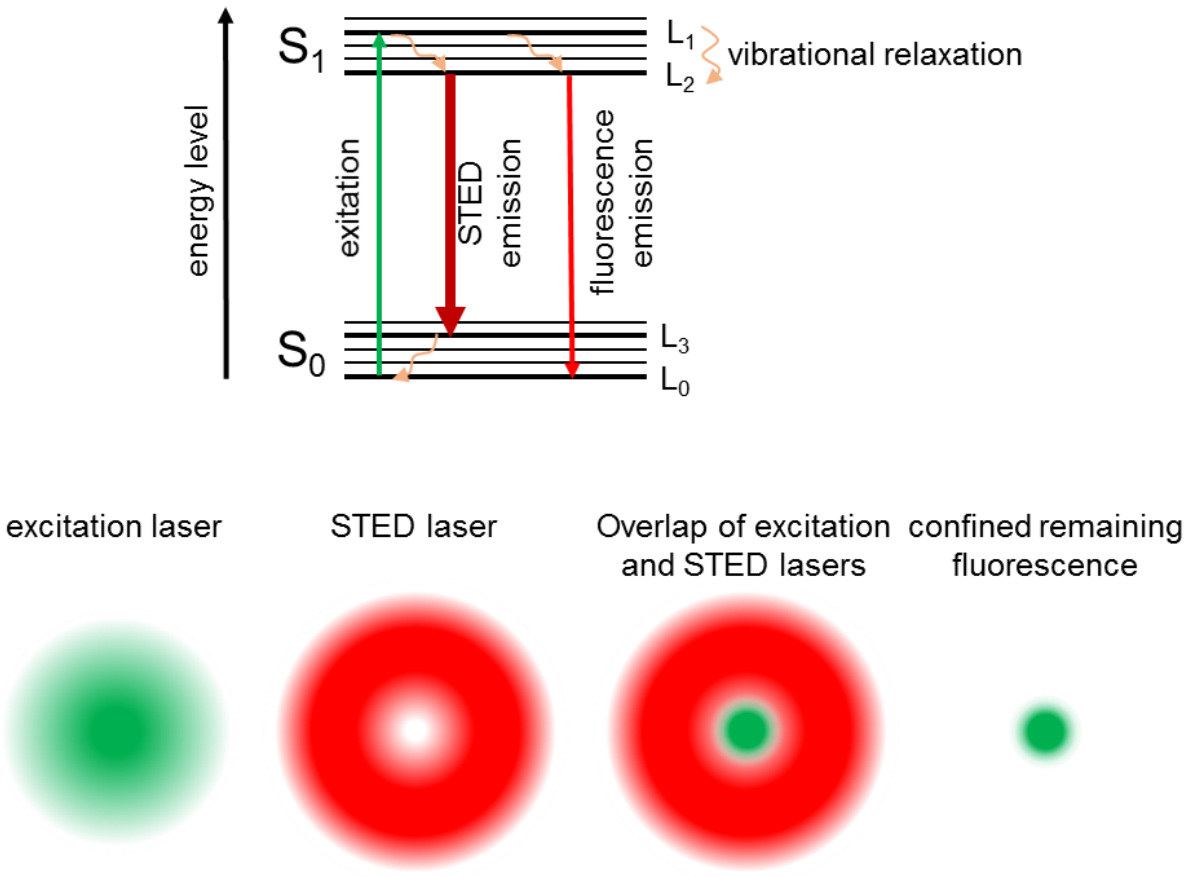

Figure 7: ***Principle of STED-microscopy.*** *During excitation of a fluorophore, an electron is energized from its ground state (S_0) to its excited state (S_1). After vibrational relaxation within the S_1 state, the electron falls back into S_0 accompanied by light radiation. Using a high energy light source like a laser (STED-laser) the electron can be forced to relax into another sub S_0 state, emitting light at a different wavelength then general fluorescence light of the same molecule. That principle is used in STED microscopy by illumination the sample with a normal excitation laser together with a donut shape STED-laser. While all the fluorophores get excited, only the one in the middle are able to emit in their normal emission spectrum. Fluorophores hit by the STED-laser are forced to emit in another wavelength, filtered out afterward by optical filters, reducing the spot size of active fluorophores to the center of the donut shape STED-laser.*

1.6.4 Comparing SIM, STED and STORM

Imaging and analysis of mitochondria requires, depending of the specific characteristic investigated, a subset of microscopical properties. In order to compare the different super-resolution microscopy techniques discussed above (1.6.1, page 12; 1.6.2, page 15; 1.6.3, page 19) the main and most important characteristics in regard of imaging properties were summed up in Table 1. While PALM/STORM clearly delivers the best special resolution, live cell experiments are very limited due to the slow acquisition time. Fast moving cellular components cannot be imaged. STED and SIM on the other side have a high temporal resolution sufficient to image dynamic processes in living cells. While STED has a superior spatial resolution

compared to SIM, the extremely high laser powers needed for the STED-laser introduce serious complications, such as bleaching, photo and cell toxicity and even thermal damaging. For long live cell experiments with a need of high spatial resolution, SIM is the best compromise of spatial and temporal resolution with similar photo toxicity and bleaching effects like conventional wide field microscopy with the added benefit of no special fluorophores needed.

	wide field microscopy	SIM	STED	PALM/STORM
resolution planar	~260 nm	100 - 140 nm	40 - 70 nm	2 - 40 nm
resolution axial	~600 nm	~250 nm	100 - 150 nm	10 - 50 nm
live imaging	> 10 frame/s	>1 frame/s	1 - 2 frame/s	0.2 frame/s
light power	< 1 W/cm^2	1 - 10 W/cm^2	100 MW/cm^2	1 - 25 kW/cm^2
colors	> 4	up to 4	maximal 2	2-4
dyes	no exclusions	no exclusions	e.g. Atto647N, Chromeo 494	e.g. A647, mEos2

Table 1: ***Comparison of wide field and super-resolution SIM, STED and STROM technics.*** *Resolution, live imaging capabilities, necessary laser power, multicolor potential and suitable fluorophores are listed for wide field, SIM, STED, and PALM/STORM microscopy.*

1.6.5 Super-resolution microscopy in analyzing mitochondrial structure and function

The current knowledge about the mitochondrial ultrastructure is mainly based on fixed cells or tissue imaged with electron microscopy. The recent advancements in super-resolution microscopy enable researchers to visualize and investigate the mitochondrial ultrastructure in living cells and can be used as an alternative to electron microscopy techniques. dSTORM was used to determine the sub-mitochondrial localization of the F_0F_1-ATP synthase [82] or uncoupling protein 4 (UCP4) [61] with high spatial resolution. These examples show that dSTORM provides a clear alternative to immunogold labeling because of a much higher labeling density. Thus, more detailed information about the organization and orientation of specific proteins or protein clusters van be obtained. However, STORM/PALM microscopy does not have the temporal resolution to analyze dynamic processes, especially the dynamics

of mitochondrial movement or of the inner mitochondrial membrane (IMM). Recently several groups were able to resolve the inner mitochondrial structure with 3D-SIM but a quantification approach was not published so far [70,83,84]. Also, STED microscopy was used to resolve the structure and dynamics of the IMM in living cells using TMRM, Mitotracker Green and fluorescent proteins [85]. The analysis and quantification of MICOS-cluster arrays along the inner boundary membrane of yeast and human mitochondria were done using STED microscopy. The super-resolution technic combined with electron microscopy and immunogold labeling enables a more complex and visual imagination of the micro-architecture of mitochondrial membrane systems [86,87].

2 Material and Methods

Material and methods are published in Gottschalk et al 2018[88] and Gottschalk et al 2019[96].

2.1 **Single and dual camera SIM imaging**

The SIM-setup used is composed of a 405 nm, 488 nm, 515 nm, 532 nm and a 561 nm excitation laser introduced at the back focal plane inside the SIM-box with a multimodal optical fiber. For super-resolution, a CFI SR Apochromat TIRF 100x-oil (NA 1.49) objective was mounted on a Nikon-Structured Illumination Microscopy (N-SIM®) System with standard wide field and SIM filter sets and equipped with two Andor iXon3® EMCCD cameras mounted to a Two Camera Imaging Adapter (Nikon Austria, Vienna, Austria). For calibration and reconstruction of SIM images, the Nikon software NIS-Elements was used. Reconstruction was always done with the same robust setting to avoid artifact generation and ensure reproducibility with a small loss of resolution of 10% compared to the most sensitive and rigorous reconstruction settings. Prior to each measurement, laser adjustment was checked by projecting the laser beam through the objective at the top cover of the bright field arm of the microscope. Lasers were aligned and focused using the interlock system screws at the N-SIM box to ensure appropriate illumination of the sample. 100 nm Tetraspec beads (InvitrogenTM, Thermo Fischer Scientific, Vienna, Austria) were diluted 1:200 in 1 ml 0.01% poly-L-lysine and incubated on the 1.5H high precision glass cover slips (Marienfeld-Superior, Lauda Königshofen, Germany) for 20 min. Afterwards, the plate was washed once and transferred to the live cell camber containing 1 ml of buffer (2CaB) containing in mM: 2 $CaCl_2$, 140 NaCl, 5 KCl, 1 $MgCl_2$, 1 HEPES and 10 D-Glucose, pH adjusted to 7.4 (all buffer salts were obtained from Roth, Graz, Austria). Ring correction was done as follows: 3D-stacks of beads were acquired to verify the point spread function of the system. Potential asymmetric point spread function was corrected using the objective correction ring. Subsequently, grating block adjustment was performed to find the perfect focus for the laser beam interference at the focal plane. This process was automatically run by the Nikon-software. To align both channels for

parallel dual-color experiments NIS-Elements Two-CAM registration was used taking the same Tetraspec bead samples. Error estimation in x,y, and z-axes caused by chromatic aberration was done by imaging multiple z-stacks of Tetraspec beads. The exact localization of the beads in both colors was determined with sub-pixel accuracy using the ImageJ plugin Quickpalm. For each bead, the x and y abbreviation was calculated and defined as a vector. The relative error of chromatic abbreviations was determined by the vector product of each bead with its nearest neighbor normalized to the distance of the beads. The alignment of both channels along the z-axes was done by selecting each bead in a 320 x 320 nm square, projecting it on the x-z axes, and determining the maximum intensity in both channels with sub-pixel accuracy using a Gaussian-fit in ImageJ (Supplementary figure 4). Cells were transiently transfected with the respective constructs or siRNAs and stained, if necessary, with Mitotracker Green/FM (MTG), Mitotracker Red/FM (MTR), or Mitotracker Red CMXROS (MTR-CMX) (InvitrogenTM, Thermo Fischer Scientific, Vienna, Austria). Simultaneous dual-channel 3D-SIM images were acquired 90 s after placing cells in 2CaB. Experiments with MTG stained mitochondria were not possible with the dual bandpass filter setup because of fluorescence bleed through into the red channel. Sequential dual-color 3D-SIM images were performed instead [88].

2.2 **Cell culture**

HeLa, HEK, MCF-7 or A549 cells were seeded on 1.5H high precision glass cover slips (Marienfeld-Superior) and cultured in DMEM (D5523, Sigma-Aldrich, Darmstadt, Germany) containing 10% FCS (Gibco™, Thermo Fisher Scientific), penicillin (100 U/ml), streptomycin (100 µg/ml) and amphotericin B (1.25 µg/ml) (all Gibco™) in a humidified incubator (37 °C, 5% CO_2/95% air).

2.3 **Cloning of constructs**

For generating mCherry or YFP-tagged constructs, the respective coding sequences were subcloned into backbones already containing the sequences for the FP's(fluorescent protein)[89]. mCherry was fused N-terminally to Tom22 (mCherry-Tom22), and, cloned into a

pcDNA3.1(-) backbone flanked by Cla-I and Hind-III restriction sites. EMRE, MCU and UCP2 constructs were fused to the N-terminus of mCherry (EMRE-mCherry, UCP2-mCherry, MCU-mCherry) and subcloned into a pcDNA3.1 (+) backbone. EMRE and MCU are flanked by Hind III and Eco RI, UCP2 by Kpn-I and Eco-RI, and ΔMICU1 by Bam-HI and Eco-RI. For SIM measurements the plasmids encoding for either wildtype MICU1, MICU1 R455K (MICU1-K), MICU1 R455F (MICU1-F) or EF hand mutated MICU1 (MICU1-EF) were C-terminally fused to a citrine (YFP) as described before [12,14]. MICU1 lacking its C-terminal domain (MICU1ΔC) was fused in-frame to the same YFP via BamHI and EcoRI restriction sites in a pcDNA3(+) vector using the primers MICU1 pos. 1 forward 5'-CCCGGATCCATGTTTCGTCTGAACTCACT-3' and MICU1 pos. 1332 reverse 5'-GGTTGAATTCCATCAGCCGTTGCTTCATGAT-3'. $MICU1^{1-70}$ and $MICU1^{1-140}$ were inserted in-frame via XhoI/EcoRI in a pcDNA3.1(-) vector containing a circular permutated enhanced green fluorescent protein (cpEGFP) [90] with the primers as follows: MICU1 pos. 1 forward; MICU1 pos. 210 reverse; MICU1 pos. 420 reverse. For suborganelle-specific Ca^{2+} measurements within the mitochondrial cristae (MC) a mutated version of reactive oxygen species modulator 1 (ROMO1) was synthesized by exchanging potential ROS modulating cysteines at pos. 15, 27 and 42 to serines. ROMO1 and the IMS specific targeting sequence of $MICU1^{1-140}$ were then fused to a ratiometric GEMGeCO1 (Addgene; Cambridge, MA, USA) via XhoI/BamHI in a pcDNA3.1(-) with the primers ROMO1 pos. 1 forward; ROMO1 position 255 reverse; MICU1 pos. 1 forward and MICU1 position 420 reverse. For immunohistochemistry of MCU-mCherry and EMRE-mCherry in frame with a myc-HIS-tag a myc-HIS-tag was constructed to the C-terminal end of the mCherry in a series of PCR amplifications by using overlapping reverse primers. The resulting mCherry-myc-His-tag fragment was then subcloned in fusion with either MCU or EMRE via EcoRI and HindIII restriction sites. All respective primers can be found in Table 2.

2.4 **Generation of UCP-KO and EMRE-KO cells**

For generating UCP2-KO or EMRE-KO cells pcDNA3.3-Cas9-2A-eGFP and pGS-U6-gUCP2 / pGS-U6-gEMRE from GenscriptTM (Thermo Fischer Scientific) were ordered. The gRNA

sequence of UCP2 is 5´-CCCAGTACCGCGGTGTGAT-3´ and for EMRE 5´-GCTAGTATTGGCACCCGTC-3´. For homologous recombination in case of UCP2, an 800-bp upstream fragment (Hind-III/Eco-RI) and an 800-bp downstream fragment (Bsm I) of the genomic UCP2 cutting side by Cas9 was cloned into the pcDNA3.1 flanking neomycin cassette. All three plasmids were co-transfected into HeLa cells in a ratio of 1:1:1. After 48 h GFP-positive cells were single sorted into 96-well plates. Clones were further cultivated and selected with G-418 (Sigma-Aldrich) for two weeks in 12-well plates. Nearly 50 clones were analyzed with PCR. To check if each allele of 5 clones was mutated, bacterial subclones were made of amplified PCR fragments and sequenced using the Sanger method (Microsynth, Balgach, Switzerland).

To generate EMRE-KO (knock out) cells, HeLa cells were co-transfected with pcDNA3.3-Cas9-2A-eGFP and pGS-U6-gEMRE. Next day, single GFP-positive cells were sorted into 96-well plates. Clones were further cultivated and analyzed with PCR. To check if each allele was mutated, bacterial sub-clones of amplified PCR fragments were made and sequenced with the Sanger method (Microsynth, Balgach, Switzerland).

2.5 **Mitochondrial staining**

Cells were washed once with loading-buffer containing in mM: 2 $CaCl_2$, 135 NaCl, 5 KCl, 1 $MgCl_2$, 1 HEPES, 2.6 $NaHCO_3$, 0.44 KH_2PO_4, 0.34 Na_2HPO_4, 10 D-glucose (Roth), 0.1% vitamins, 0.2% essential amino acids and 1% penicillin/streptomycin (Gibco™) at pH 7.4. Cells were incubated in loading-buffer containing 0.5 µM MTG, 0.5 µM MTR, or 0.05 µM MTR-CMX (Invitrogen™) for 40 minutes or 10 minutes, respectively. Thereafter, cells were washed once with loading buffer and imaged in 2CaB.

2.6 **Transfection siRNA treatment**

HeLa cells were grown under standard culture conditions until 50% confluence was reached, transfected in DMEM (without FCS and antibiotics) with 1.5 µg/ml plasmids or 100 nM siRNA using 2.5 µg/ml TransFast™ transfection reagent (Promega, Madison, WI, USA)[10]. After 24h,

the medium was replaced with DMEM containing 10% FCS and 1% penicillin/streptomycin and kept for further 24 h prior experiments. The specific siRNAs (Microsynth) used in this study are listed in Table 2.

2.7 Cytochrome c staining

After staining the cells with MTR-CMX cells were washed with PBS (phosphate buffered saline), fixed with 3.7 % paraformaldehyde (PFA) in PBS for 15 min and permeabilized with 0.25% (v/v) Triton X-100/PBS for 15 min at RT. Following permeabilization, cells were washed twice with PBS and nonspecific absorption was blocked using UltraVision blocking reagent (Thermo Fisher Scientific) for 10 min at RT. Then, cells were incubated at 4 °C overnight with anti-Cytochrome c antibody (Cell Signaling, # 12963; 1:100 in Antibody Diluent, Dako). After washing with PBS, Alexa488-labeled goat anti-mouse IgG (Invitrogen, # A11001; 1:300 in Antibody Diluent) was used as a secondary antibody (60 minutes, RT). Slides were stored in 1% (w/v) BSA/PBS until further use.

2.8 Sub-mitochondrial localization of UCP2, MCU, EMRE, and TOM22

Cells transfected with EMRE-mCherry, MCU-mCherry, UCP2-mCherry or mCherry-TOM22 were stained with MTG and imaged using 3D-SIM microscopy. Images were background-subtracted with an ImageJ Plugin (Mosaic Suite, background subtractor, NIH). The width of mitochondria was measured using the FWHM (full width at half maximum). Line plots were taken for the images in ImageJ and the FWHM was determined.

2.9 Assigning MICU1 localization to inner mitochondrial membrane

Dual-color 3D-SIM images of MICU1-YFP and mCherry-TOM22 transfected cells in 2CaB were background-subtracted with an ImageJ plugin (Mosaic Suite, background subtractor, NIH). Blind line plots of mitochondrial cross-sections within the mCherry-TOM22 label were done. The outer mitochondria membrane can be modeled as a hollow tube that, if stained, displays a double line structure in z-projection[91]. Intensity line plots of MICU1-YFP and

mCherry-TOM22 were fitted to a double Gaussian-function. The distances of the peak values of these fits can be interpreted as the diameter of the mitochondria and were determined for both channels. By bisecting the difference in peak distances of MICU1-YFP and mCherry-TOM22 staining the distance of both labels on one side can be determined. Using the hollow tube model and the Gauss fitting method the precision for estimating the center localization of MICU1 and TOM22 distributions can be increased beyond the actual resolution of SIM microscopy as long as the mitochondrial double line structure in images or the double peak structure of mitochondrial cross section intensity plots is present. For image analysis, the freeware program ImageJ (NIH, MA, USA) was used.

2.10 **MICU1 time-lapse imaging during mitochondria depolarization**

Time lapse imaging of MICU1 cristae relocalization was performed with 30 s time increments over 300 seconds in 2CaB supplemented with 2 µM oligomycin A (Sigma-Aldrich). 90 seconds after acquisition started, antimycin A was added into the live cell chamber to a final concentration of 4 µM.

2.11 **Analysis of protein sub-mitochondrial localization**

Dual-color images were split into two separate channels, background-corrected with an ImageJ Plugin (Mosaic Suite, background subtractor, NIH) and further described as object and reference channels. The reference channel was Otsu auto thresholded [92] and further in two parallel approaches either dilated (iterations=1-4 count=1) or treated with an erosion algorithm (iterations=2-6 count=1). The Otsu auto threshold algorithm included in ImageJ generates a grayscale intensity histogram and separates the pixel intensities in two groups. The threshold between these groups is chosen by minimizing the intra-class variance. By minimizing the weighted sum of variances of the two classes background and structural fluorescence information can be distinguished from each other in an automated, unbiased, and reproducible procedure[92]. Erosion, dilation iterations, and counts were changed according to the experiment to get the highest sensitivity possible for each experimental set. More detailed information

about the parameters used and comparability between the experiments is listed elsewhere (Table 3)**.** Different settings of erosion and dilation parameters were necessary to extract the sub-mitochondrial localization using different reference markers with variable mitochondrial localization patterns. In case of MICU1-YFP as the reference after auto thresholding, a fill holes step was added. Pixel-wise subtraction of the erosion reference of the dilated reference image yields in a hollow structure. The hollow structure was further used as a template to determine the fluorescence intensity in the IBM while the erosion reference served as a template for the bulk or cristae fluorescence intensity. The measured fluorescence intensities were normalized to the area covered by the cristae and IBM template. The ratio of IBM/CM mean intensities is a value to estimate changes of the object label distribution inside a mitochondrion and termed IBM association index. The higher the ratio value the higher the distribution of protein label in the IBM. For image analysis the freeware program ImageJ was used.

2.12 **Electron microscopy and analysis of cristae junction width**

Cells were washed in PBS, fixed with 2.5% glutardialdehyde and 2% formaldehyde in a buffered solution and post fixed in 1% osmium tetroxide that had been reduced with 1% potassiumhexacyanoferrate[93]. The cells were dehydrated in an ascending ethanol series, embedded in TAAB embedding resin, and sectioned on a Leica Ultracut 7 ultramicrotome using a Diatome diamond knife. The sections were counterstained using platinum blue (IBIlabs) and lead citrate (Leica) and visualized in an FEI Tecnai 20 transmission electron microscope. They were photographed at 27,000x magnification with a Gatan ultrascan 1000 camera. To quantitatively analyze the electron microscopical images a line was drawn in ImageJ manually into the cristae starting with the cristae junction proceeding into the cristae volume as far as the image quality was sufficient for image quantification, the curvature of the cristae was not crossing the line or a maximum of 130 nm length was reached. Along the drawn line every 2 nm orthogonally line plots with a width of 10 nm were measured with an ImageJ macro starting from the CJ. Each line plot was halved and the position of the minimal intensity was determined

for both sides. The distance of both minimal intensities was set as the distance between opposing sides of the cristae.

2.13 **Morphological analysis of mitochondria imaged with SIM**

Single 3D-SIM and time-lapsed images of EMRE-mCherry, MTR, MTG, or MICU1-YFP were used for morphological analysis over time. Images were background corrected with an ImageJ Plugin (Mosaic Suite, background subtractor, NIH) and a binarization was done using a Yen auto threshold [94]. The ImageJ particle analyzer was used to extract the mitochondrial count (c), area (a), perimeter (p), minor (x) and major (y) axes of the mitochondria. Aspect ratio (AR) was determined as $AR = \frac{y}{x}$

The Form Factor (FF) was determined as followed: $FF = \frac{p^2}{4\pi \cdot a}$

For image analysis the freeware program ImageJ was used.

2.14 **Morphological analysis of mitochondria imaged with confocal microscopy**

Z-stacks of mitochondria with 0.2 µm increments were imaged with a Zeiss Observer Z.1 inverted microscope equipped with a Yokogawa CSU-X1 Nipkow spinning disk system, a piezoelectric z-axes motorized stage (CRWG3-200; Nippon Thompson Co., Ltd., Tokyo, Japan), and a CoolSNAP HQ2 CCD Camera (Photometrics). The image stacks were deconvolved using blind deconvolution (NIS-Elements, Nikon, Austria). Morphology parameters were measured automatically with a custom-made ImageJ macro using the following procedure. An additional background subtraction using the rolling ball method was used to further increase contrast for later analysis. Both a global auto Otsu threshold using the stack histogram as well as a local auto Otsu threshold (radius of 640 nm) using the single slice histogram were applied to the stack and merged. The ImageJ plugin 3D manager was used to segment the binarized mitochondria. With the plugin 3D Geometrical Measure the mitochondrial volume and surface were determined. The Plugin 3D Ellipsoid Fitting generated an ellipsoid fit of the mitochondria to measure elongation and flatness parameters.

2.15 Mitochondrial shape descriptors and co-localization of MTG and ER-RFP

HeLa cells transfected with ER-RFP and stained with MTG were recorded with live dual-color SIM imaging. The mitochondrial branching was measured by determining the area-weighted form factor and mitochondrial size using ImageJ [88]. For co-localization studies, the ImageJ plugin coloc2 was used to measure the Pearson coefficient.

2.16 Cell viability and apoptosis assay

24 h after transfection in 10 cm dishes, cells were seeded in 96-well plates at a density of 5,000 cells per well. Cell viability was measured using CellTiter®-Blue assay (Promega) and apoptotic caspase activity via Caspase-Glo®3/7 assay (Promega) following the standard protocols [14].

2.17 Live cell Fura-2, TMRM, and mitochondrial Ca^{2+} measurements

Measurements were performed on an inverted and advanced fluorescence microscope with a motorized sample stage (Till Photonics, Graefling, Germany). The probes were excited via a polychrome V (Till Photonics), and emission was visualized using a 40x objective (alpha Plan Fluar 40, Zeiss, Goettingen, Germany), and a charge-coupled device camera (AVT Stringray F145B, Allied Vision Technologies, Stadtroda, Germany). Fura-2 (Invitrogen™) was alternately excited at 340 and 380 nm, and emissions were captured at 515 nm (495dcxru; Omega Optical, Brattleboro, VT, USA). TMRM (Cat: T668; Invitrogen™) was excited at 550 nm, and emissions were captured at 600 nm (59004; Chroma, Bellows Falls, VT, USA). Mitochondrial Ca^{2+} FRET-measurements with 4mtD3cpv were done using 430 nm and 480 nm excitation, and emission was captured at 480 nm and 535 nm (69008; Chroma), respectively[12]. For control of the microscope and acquisition, the live acquisition 2.0.0.12 software (Till Photonics, Munich, Germany) was used. For Fura-2 imaging cells were incubated in loading-buffer containing 3.3 µM Fura-2 for 40 min [14]. TMRM loading was done likewise for 40 min with a TMRM concentration of 100 nM [95]. For mitochondrial Ca^{2+} measurement cells were transfected with the 4mtD3cpv-Plasmid[9]. All recordings were background-subtracted using a background

ROI and corrected for bleaching using an exponential decay fit. Mitochondrially targeted R-GECO was used to measure mitochondrial Ca^{2+} using the single-channel SIM-setup in wide field mode. Time-lapse images were background subtracted using a background ROI and corrected for bleaching using an exponential decay fit.

2.18 Live cell measurement of inter boundary membrane and cristae membrane Ca^{2+}

Ratiometric green-emitting genetically encoded Ca^{2+} indicators for optical imaging (GEMGeCO1) fused to either ROMO1 or MICU11-140 was excited at 430 nm and emissions were collected by using a conventional CFP/YFP dichroic filter at 480 and 535 nm. The resulting ratio was calculated by the division of the fluorescence intensity at 480 nm by 535 nm.

2.19 mRNA Isolation and real-time PCR

Total RNA was isolated according to the manufacturer's protocol using the PEQLAB total RNA isolation kit (Peqlab, Erlangen, Germany). cDNA was generated using a high-capacity cDNA reverse transcription kit (Applied Biosystems, Foster City, CA) and a thermal cycler (Peqlab). Knock-down and overexpression efficiency of MICU1 was examined by qRT-PCR using a QuantiFast SYBR Green RT-PCR kit (Qiagen, Hilden, Germany) and a LightCycler 480 (Roche Diagnostics, Vienna, Austria). Relative expression of the gene of interest was normalized to GAPDH, as a reference gene. Primers for real-time PCR were designed by us and obtained from Invitrogen (Vienna, Austria). The respective primer sequences used can be found elsewhere (Table 2).

2.20 Co-Immunoprecipitation

HeLa or HEK cells were transfected with MICU1-FLAG alone or in combination with MCU-mCherry-HIS or EMRE-mCherry-HIS constructs. The transfection process was repeated three times over a period of three days. Transfected cells were lysed in 0.7 mL lysis buffer (100 mM

NaCl, 20 mM Tris, 1 mM EGTA, 5 mM n-Dodecyl β-D-maltoside, pH 7.5-HCl) supplemented with protease inhibitors (10 µM phenylmethylsulfonyl fluoride, and 1 µg/ml each aprotinin, leupeptin, and pepstatin). After a short freeze-thaw cycle, lysates were centrifuged (12,000g, 10 min) and 60 µl of supernatants were removed for protein determination using a BCA assay (Thermo-Fisher) and total cell lysate analyses (input). The rest of the lysates (~ 1.2 mg total protein of HeLa cells and ~ 2 mg of HEK cells) were incubated with 30 µl of anti-Flag M2 affinity gel (Sigma-Aldrich; A2220-1ML; beads were prepared as recommended by the manufacturer) for 30 minutes on a rotary shaker. Then, beads were collected by centrifugation (8,000g, 30 seconds) and washed three times with TBS. All steps were performed on ice or at 4°C. Elution of FLAG-fusion proteins was performed in 50 µl of 2x Lämmli sample buffer with 5% β-mercaptoethanol and boiling for 10 minutes. For immunoblotting, whole-cell lysates (input, 120 µg of total protein) and Co-IP samples were subjected to SDS-PAGE. PVDF membranes were probed at 4 °C overnight with primary monoclonal mouse anti-6x His Tag antibody (Thermo Fisher, 1:000). To avoid interference from denatured heavy and light chain IgG, the HRP-conjugated immunoblot reagent Veriblot (Abcam; ab131366; 1:000) was used for detection of co-immunoprecipitated proteins. For detection of protein expression in input samples, HRP-conjugated goat-anti-mouse secondary antibody (Sigma, 1:2500) was used. Immunoreactive bands were visualized using Immobilon Western HRP Substrate (Thermo Fisher) and the chemiluminescence detection system ChemiDoc (Bio-Rad).

2.21 **Western Blot for MICU1 degradation analysis**

HeLa cells plated in 6-well plates were treated with 2 µM antimycin A and 4 µM oligomycin A for 2 and 10 minutes. For immunoblotting, whole-cell lysates were prepared with radioimmunoprecipitation assay (RIPA) buffer and 100 µg of total protein was subjected to SDS-PAGE. PVDF membranes were probed with primary polyclonal rabbit anti-MICU1 (Cell Signaling; 12524S) and HRP-conjugated goat-anti-rabbit (Sigma) antibodies. For normalization, membranes were stripped and re-probed with a primary antibody against β-

actin (Sigma). Immunoreactive bands were visualized using Immobilon Western HRP Substrate (Thermo Fisher) and the chemiluminescence detection system ChemiDoc (Bio-Rad).

2.22 **CM kinetics quantification**

Live SIM imaging sequences of 30 frames with a frame rate of 1 Hz of MTG-stained HeLa cells were recorded. The open-source program ImageJ was used to analyze the CM-kinetics. First, time-lapse acquisitions were background corrected using a histogram-based background subtractor (Mosaic group). Further, a time-dependent bleach correction using an exponential fitting method was applied to correct for intensity decrease over time caused by photobleaching. The corrected time lapse was auto thresholded twice. A global Otsu auto threshold[92] was used to segment mitochondria and a local mean auto threshold with a two-pixel radius was used to identify small intensity differences within the IMM structure. By pixel-wise multiplying both thresholded time lapses, the structural information of the IMM can be revealed. To determine the IMM-kinetic the difference of subsequent frames in time was calculated. Since mitochondria are moving very fast and changing their shape, the changes per frame of the IBM shell were excluded. Therefore, a closing algorithm consisting in the succession of a dilation with an erosion (iterations = 2 count = 2) as well as a whole filling algorithm were applied on the thresholded time lapse containing the IMM-structural information. Subsequent frames were subtracted from each other to get the IBM-kinetic of the mitochondrial shell. By subtracting the difference per frame of the IBM mitochondrial shell from the overall IMM-changes within the mitochondria, the CM-kinetics were extracted. Afterwards, the accumulated pixel counts of the CM-changes were normalized to the global Otsu auto thresholded pixel count for each frame and the mean of the time lapse was determined[88].

2.23 **Quantification of the CM-kinetics in relation to ER-proximity**

HeLa cells transfected with ER-RFP and stained with MTG were recorded with live dual-color SIM imaging. Three repeats of one frame ER-targeted red fluorescence protein (ER-RFP) and

10 frames MTG at a frequency of 1 Hz were recorded. To quantify the inner mitochondrial membrane kinetic in correlation to the sub-mitochondrial localization, the IMM-kinetics were measured like described above. Additionally, ER-RFP was globally Otsu thresholded. The overlap of both labels was generated by frame-wise multiplication and defined as mitochondria-associated membrane (MAM). These regions were enlarged by stepwise dilatation (iterations = 5, 10, and 20; pixel count = 3) to increase the area. By frame-wise multiplication of these differently enlarged MAM regions with the CM-inter-frame changes, the IMM-kinetic in close proximity to the ER could be defined. Further, the auto Otsu thresholded MTG area was reduced by multiplication with the differently enlarged MAM regions to get the proper size for normalization[88].

2.24 **Statistical analysis and reproducibility**

Each exact n value and the number of independent experiments is indicated in each figure legend. Statistical analysis was performed using the GraphPad Prism software version 5.04 (GraphPad Software, San Diego, CA, USA) or Microsoft Excel (Microsoft Office 2013). Analysis of variance (ANOVA) with Bonferroni post-hoc test and t-test were used for evaluation of the statistical significance. All Box-plots show minimum to maximum values as median and second and third quantile, while whiskers cover the first and fourth quantile. $P < 0.05$ was defined to be significant. At least three different experiments on three different days performed in at least triplicates have been performed for each experimental set-up.

3 Results

3.1 Influence of Ca^{2+} on the cristae kinetics in mitochondrial-ER junctions

The first part of the results section is based on my first author publication (Gottschalk et al. 2018). In short, structured illumination microscopy was used to visualize and quantify the dynamic movements of the inner mitochondrial membrane compartments` inner boundary membrane (IBM) and cristae membrane (CM). Knock-down of OPA1 decreased CM kinetics without influencing the IBM. Furthermore, dual-color SIM was used to monitor the CM dynamics in close proximity to the ER under IP_3-induced ER Ca^{2+} release.

3.1.1 Super-resolution SIM allows the discrimination of the kinetics of the IBM vs. CM

Initially, I verified the feasibility of our attempt to determine and quantify the dynamics of the IMM by utilizing SIM. Therefore, HeLa cells were loaded with MitoTracker Green® (MTG) and directly imaged at a frequency of 1 Hz with SIM. Live SIM time-lapse imaging allowed a detailed analysis of the dynamic changes of mitochondrial membranes[88] (Figure 8).

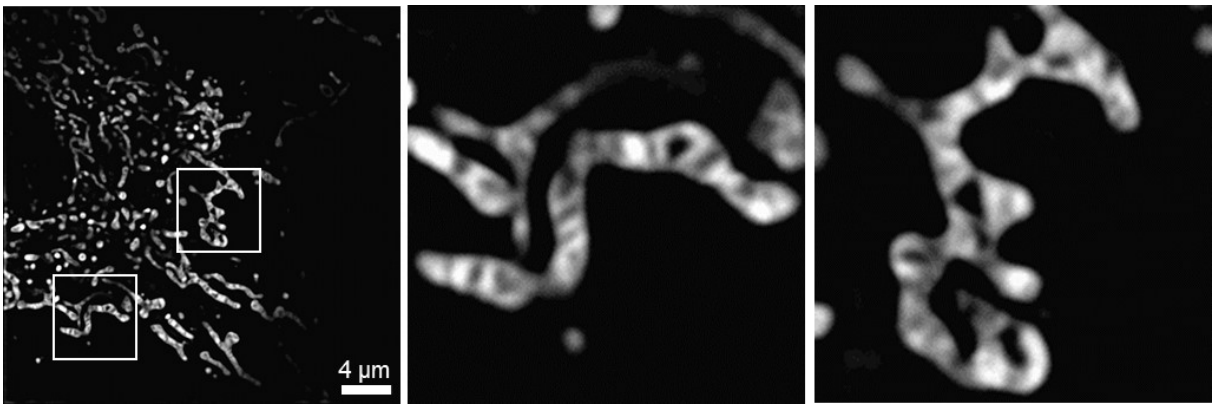

Figure 8: ***Structured illumination microscopy resolves the cristae structure.*** *HeLa cells were incubated with MTG for 40 min and time-lapse data was acquired at the N-SIM system. The middle and right panels show the magnifications of the left panel inside the white boxes[88]. [Figure panels reproduced from Gottschalk et al., Pflügers Archiv - European Journal of Physiology 2018.]*

Besides the labeling of the IMM by MTG, cells were transfected with TOM22-mCherry, ERME-mCherry, MCU-mCherry, and UCP2-mCherry constructs to visualize the sub-mitochondrial localization of the respective proteins and to validate the performance of the dual cam system.

While TOM22-mCherry showed a corona-like structure around the MTG mitochondrial reference, EMRE-mCherry, MCU-mCherry, and UCP2-mCherry co-localized with the IMM marker MTG (Figure 9).

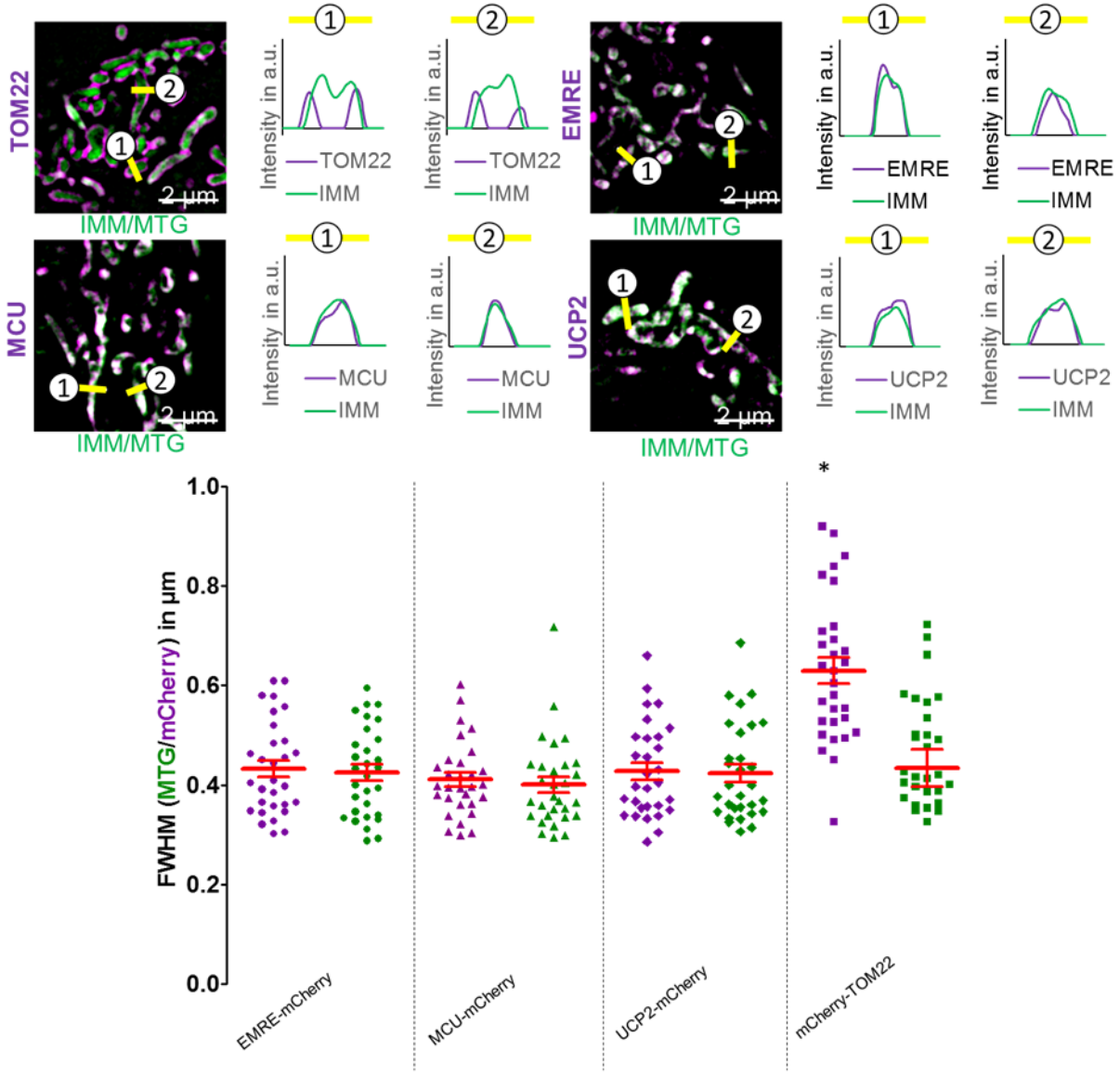

Figure 9: ***Representative images of mitochondrial proteins imaged with live 3D-SIM.*** *HeLa cells were transiently transfected with either mCherry-TOM22 (TOM22), EMRE-mCherry (EMRE), MCU-mCherry (MCU) or UCP2-mCherry (UCP2) (all magenta), stained with Mitotracker Green® (MTG) (green) prior to experiments and imaged under resting conditions utilizing sequential 3D-SIM imaging. Excluding mCherry-TOM22, all images and line plots taken from the indicated dotted lines in the images revealed a ubiquitous distribution of these proteins over the entire IMM indicated by their co-localization with MTG. The mitochondrial FWHM was measured for MTG and mCherry signals in cells transfected with MCU-, EMRE-, or UCP2-mCherry or mCherry-TOM22. No significant changes could be measured for the MTG FWHM while the mCherry-TOM22 FWHM was significantly increased compared to others. Data encompass n=30 cells form 3 independent experiments *P<0.05 vs. respective control conditions (ANOVA/Bonferonie post hoc)[96]. [Figure panels reproduced from Gottschalk et al., Nature Communication 2019.]*

To further test the N-SIM system regarding its dual color capabilities, HeLa cells were transfected with mtDSRed (a red fluorescent protein targeted to the mitochondrial matrix) and stained with the IMM-marker MTG. A 3D-SIM dual-color time course of 20 min was acquired using a frame rate of 1 Hz. The IMM and mitochondrial matrix marker did show a low amount of co-localization while the image quality could be maintained until the end of the time course (Figure 10).

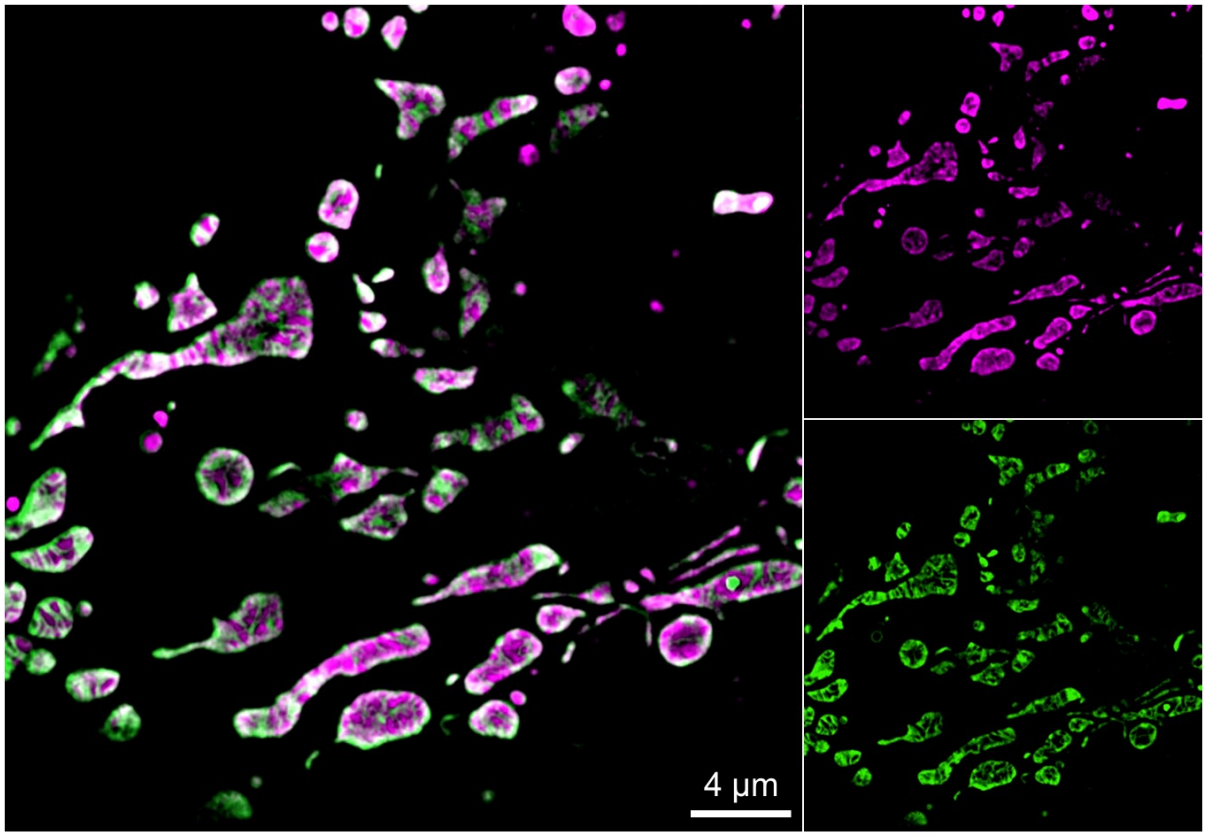

Figure 10: ***Dual color structured illumination microscopy resolves mitochondrial cristae and matrix****. HeLa cells were transfected with mtDsRed, labeled for 40 min with MTG and time-lapse data was acquired with Dual-Cam N-SIM. Clear structures of the IMM (MTG) and the matrix (MtDsRed) excluding each other can be observed.*

3.1.2 Depletion of OPA1 specifically affects cristae dynamics but not that of the IBM

To determine the cristae dynamics under various conditions, an analysis strategy was developed to filter and quantify the dynamic movement of the cristae membrane (CM) separately to that of the inner boundary membrane (IBM). This strategy consists of the following five steps (Figure 11): First, images out of a time-lapse acquisition were binarized applying local auto-thresholding. Second, to extract the individual kinetics of the IMM and CM,

a closing and fill holes algorithm was applied, and the delta intensity of subsequent frames was detected and determined as mitochondria IBM-changes. Third, the delta intensities of subsequent frames without applying the closing and fill holes algorithm were detected and determined as mitochondrial IMM-changes. Fourth, IBM-changes were subtracted from IMM-changes, thus revealing the changes within the CM (i.e., CM-changes). Fifth, the overall pixel intensities of CM-changes were frame-wise normalized to the global threshold area to get the percentage of moving mitochondrial area inside the mitochondria[88].

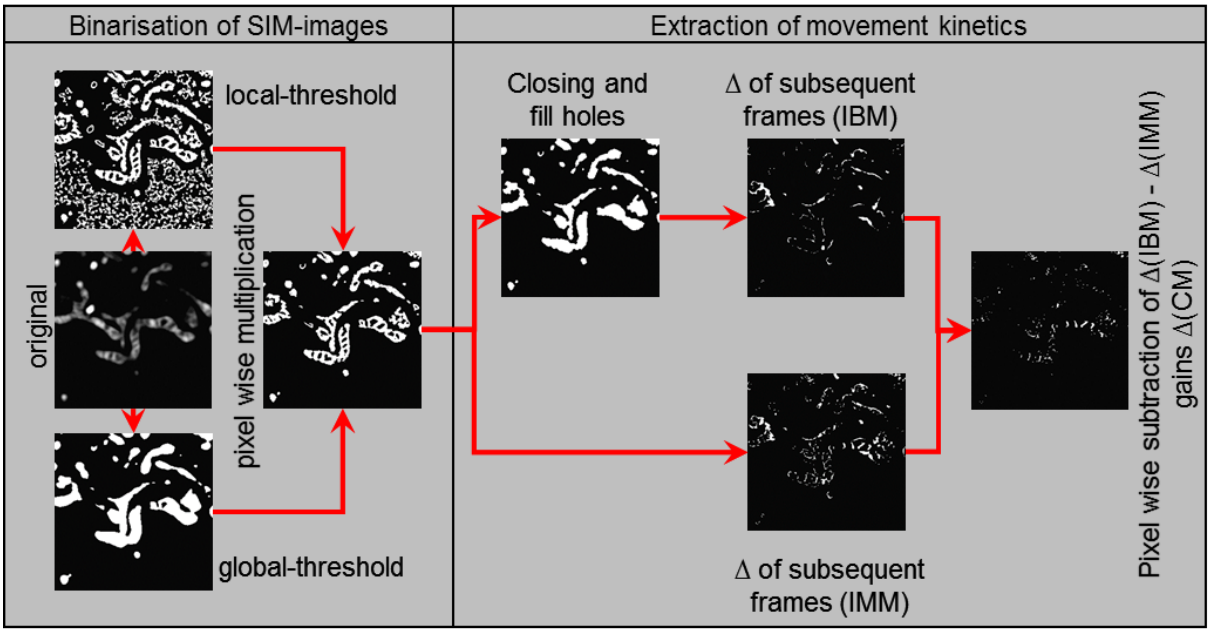

Figure 11: ***Process applied to quantify the kinetics of the IMM.*** *Time-lapse images were binarized applying local auto-thresholding (left panel), a closing and fill holes algorithm was applied and the delta intensity of subsequent frames was detected and determined as mitochondrial IBM-changes (middle panel). Delta intensities of subsequent frames without applying the closing and fill holes algorithm determined the mitochondrial IMM-changes. IBM-changes were subtracted from IMM-changes, thus revealing the dynamics of the CM. Finally, the overall pixel intensities of CM-changes were normalized to the global threshold area presenting the percentage of moving area inside the mitochondria [88]. [Figure panels reproduced from Gottschalk et al., Pflügers Archiv - European Journal of Physiology 2018.]*

To test the sensitivity of the SIM-based analysis of spatial IMM-dynamics described above, HeLa cells were depleted of OPA1, a known protein of the CJ, by transient transfection with the respective siRNA. Our analysis of spatial IMM kinetics revealed that the knock-down of OPA1 exclusively decreased kinetics of the CM while that of the IBM remained unchanged[88]. Considering that a knock-down of OPA1 results in a broadening of the CJ, our data suggest that cristae dynamics is reduced under conditions of widened CJ (Figure 12)[88].

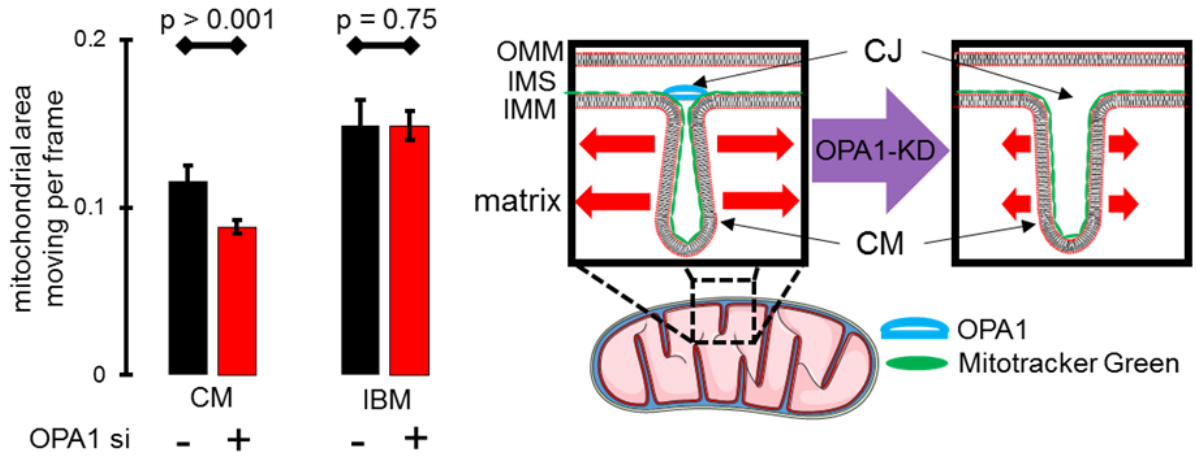

Figure 12: ***Influence of OPA1 in CM-kinetics.*** *HeLa cells were labeled with MTG imaged on the N-Sim system and analyzed like described in Figure 11. The percentage of mitochondrial area moving per frame separated into the CM and IBM was quantified for Control siRNA and OPA1 siRNA (n = 6). Schematic representation of the IMM and the OPA1-controlled CJ. Diminution of OPA1 leads to widened CJ and reduced cristae kinetics (IMM – inner mitochondrial membrane; OMM – outer mitochondrial membrane; IMS – intermembrane space; CJ – cristae junctions; CM – cristae membrane). Images and analyses were obtained from at least 5 cells in each of 6 experiments (n = 6). Bars represent mean ± SEM [88]. p vs. respective control conditions (two sided unpaired t-test) [Figure panels reproduced from Gottschalk et al., Pflügers Archiv - European Journal of Physiology 2018.]*

3.1.3 Analyzing the spatial IMM-kinetics in proximity to MAM structures

To investigate whether or not sites of physical and functional ER-mitochondrial coupling (i.e. MAMs) influence the spatial IMM kinetics in their vicinity, HeLa cells were transfected with ER-targeted red fluorescent protein (ER-RFP) and stained with MTG[88] (Figure 13).

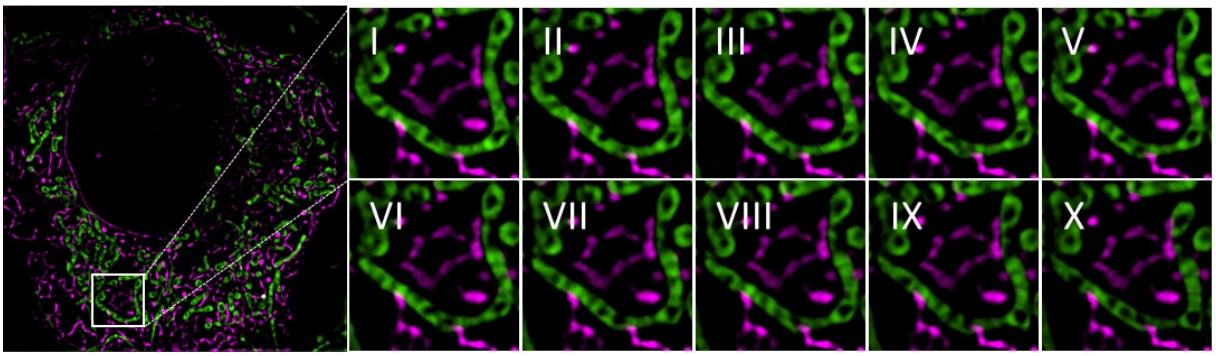

Figure 13: ***Cristae dynamics in close proximity to the ER.*** *HeLa cells transfected with ER-RFP and stained 40 min with MTG were imaged. A representative sequence of 10 frames (1 Hz) is shown as a magnification.*

The co-localization of both auto-thresholded labels obtained in the SIM was defined as MAMs. Spatial IMM-kinetics were measured within distinct areas with given proximity to MAM

structures experimentally defined as incremental dilatations of the defined MAM area[88] (Figure 14).

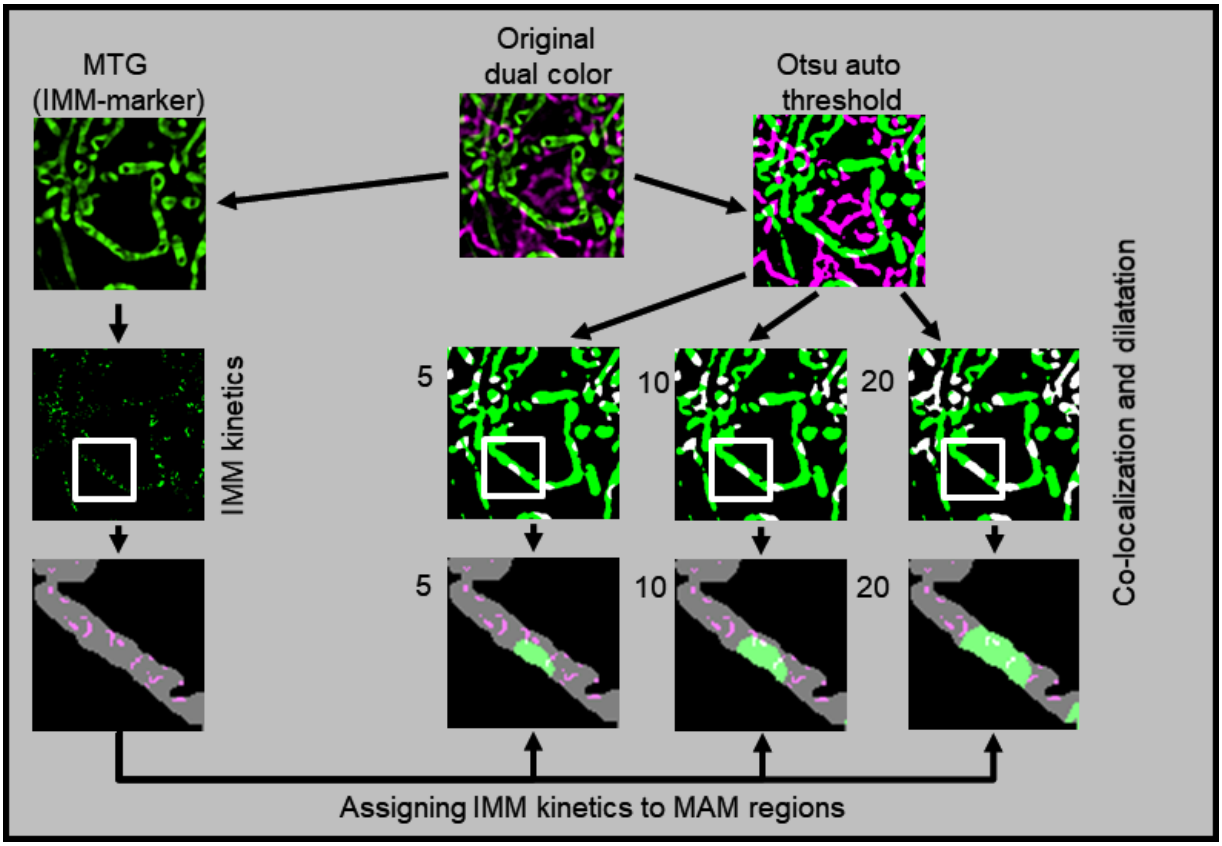

Figure 14: ***Scheme for the analysis of cristae dynamics in close proximity to the ER.*** *HeLa cells were transfected with ER-RFP, stained with MTG and imaged with live N-SIM. Both channels were auto Otsu thresholded. Overlap regions of ER and mitochondria were determined as MAMs and the areas of co-localization were incrementally dilated using 5, 10 or 20 iterations. The IMM-dynamics measured according to Fig. 1b were cropped to the dilated areas and subsequently quantified [88]. [Figure panels reproduced from Gottschalk et al., Pflügers Archiv - European Journal of Physiology 2018.]*

Expressing ER-RFP and labeling mitochondria with MTG allowed us to localize MAMs and to quantify IMM-dynamics to draw a correlation between CM-dynamics and its distance/proximity to MAMs. Using this approach, I could show significantly lower CM-kinetics in close proximity to MAMs compared to the overall CM-dynamics of the entire mitochondrial IMM area (Figure 15)[88]. To test the involvement of Ca^{2+} hotspots within the MAMs in local regulation of CM-dynamics, spatial Ca^{2+} signaling was prevented by loading cells with the fast Ca^{2+} chelator BAPTA-AM and CM-dynamics was measured[88]. Chelation of MAM-Ca^{2+} prevented the reduction of CM-dynamics in the proximity of MAMs and restored its dynamics to levels of the complete mitochondria (Figure 15)[88].

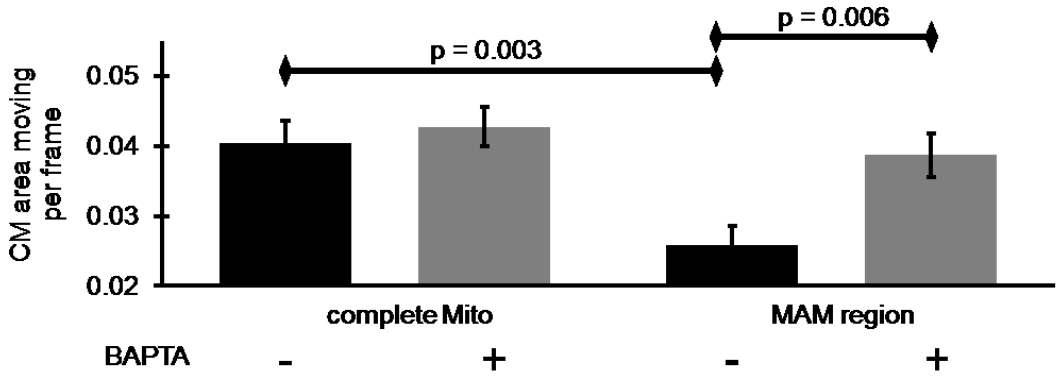

Figure 15: ***Ca^{2+} dependent reduction of CM-kinetics in MAM related mitochondrial regions.*** *HeLa cells stained with MTG and transfected with ER-RFP were imaged with N-SIM. Cells were incubated for 45 min in 2Ca-buffer or 0Ca-buffer with 50 µM BAPTA-AM. CM-dynamics of the complete mitochondria and that of MAM-related areas (5 iterations) were quantified. Bars represent mean ± SEM (n = 6)[88]. p vs. respective control conditions (ANOVA/Bonferonie post hoc) [Figure panels reproduced from Gottschalk et al., Pflügers Archiv - European Journal of Physiology 2018.]*

Furthermore, OPA1 knock-down resulted in a significant reduction of the CM-dynamics independently from its proximity to existing MAMs (Figure 16)[88].

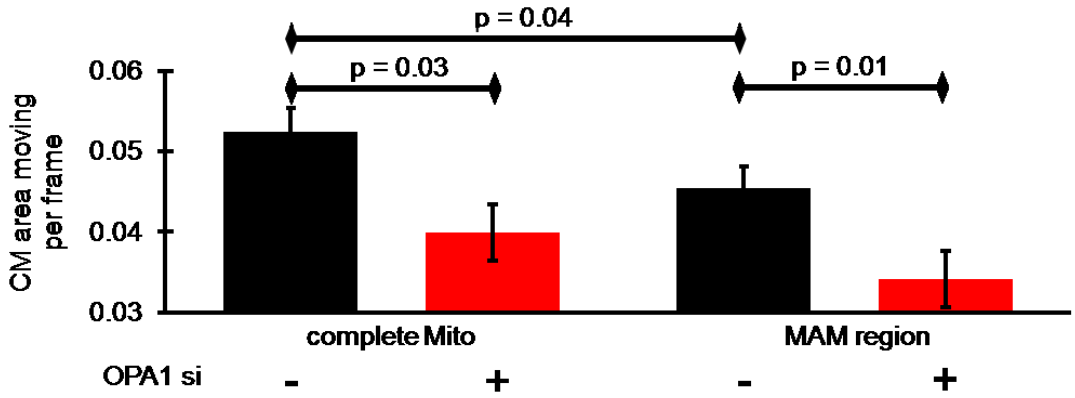

Figure 16: ***Silencing of OPA1 reduces CM-kinetics independent of MAM proximity.*** *HeLa cells transfected with ER-RFP and Control siRNA or OPA1-specific siRNA, stained with MTG were imaged with live N-SIM. CM-dynamics over the entire mitochondrion and in MAM-close regions (5 iterations) were quantified. Images and analyses were obtained from at least 5 cells in each of the 8 experiments (n = 8). Bars represent mean ± SEM [88]. p vs. respective control conditions (ANOVA/Bonferonie post hoc) [Figure panels reproduced from Gottschalk et al., Pflügers Archiv - European Journal of Physiology 2018.]*

3.1.4 ER Ca^{2+} release spatially influences CM-kinetics

To test the effect of intracellular Ca^{2+} release on CM-dynamics, cells were transfected with ER-RFP and stained with MTG. Ionomycin (200 nM) was used to evoke global Ca^{2+} release from the ER. Cells were imaged with and without the addition of ionomycin. While the CM-dynamics within the whole mitochondrion remained unchanged after the global Ca^{2+} release, the kinetics of CM decreased with the proximity (i.e., 5 and 10 iterations) to MAMs (**Fig. 10**)[88]. At farther distance from the MAM structures (i.e., 20 iterations), the CM kinetics were comparable to that of the whole mitochondria (Figure 17) [88].

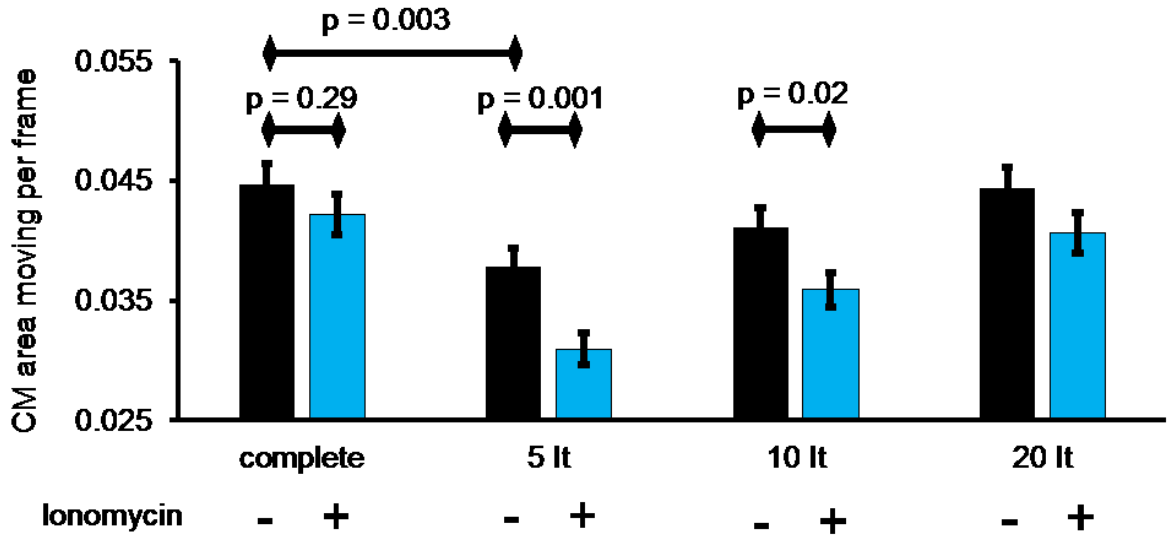

Figure 17: ***Differential IMM-dynamics in MAM and non-MAM mitochondrial regions upon ionomycin induced ER Ca^{2+} release.*** *HeLa cells transfected with ER-RFP and stained with MTG were imaged with live N-SIM. Cells were treated with 200 nM Ionomycin to induce selective ER Ca^{2+} release. IMM-dynamics were measured within the whole IMM surface and compared with that in close proximity to the MAMs with increasing area of influence, represented by the increasing amount of dilatation of 5, 10 and 20 iterations. Images and analyses were obtained from at least 5 cells in each of the 8 experiments (n = 8). Bars represent mean ± SEM [88]. p vs. indicated conditions (ANOVA/Bonferonie post hoc) [Figure panels reproduced from Gottschalk et al., Pflügers Archiv - European Journal of Physiology 2018.]*

Next, I investigated the impact of agonist-induced ER Ca^{2+} release on CM-dynamics in the entire mitochondria and in correlation with the distance to MAMs. Therefore, HeLa cells that were transfected with ER-RFP and stained with MTG were stimulated with the IP3-generating agonist histamine or ATP to induce strong ER Ca^{2+} release. Similar to our data with ionomycin, the CM-dynamics of the entire mitochondria was not affected upon strong IP3-mediated ER Ca^{2+} release (Figure 18)[88]. However, CM-dynamics in the proximity of MAMs was strongly

attenuated upon agonist-induced intracellular Ca^{2+} release, independently of the agonist used (Figure 18)[88].

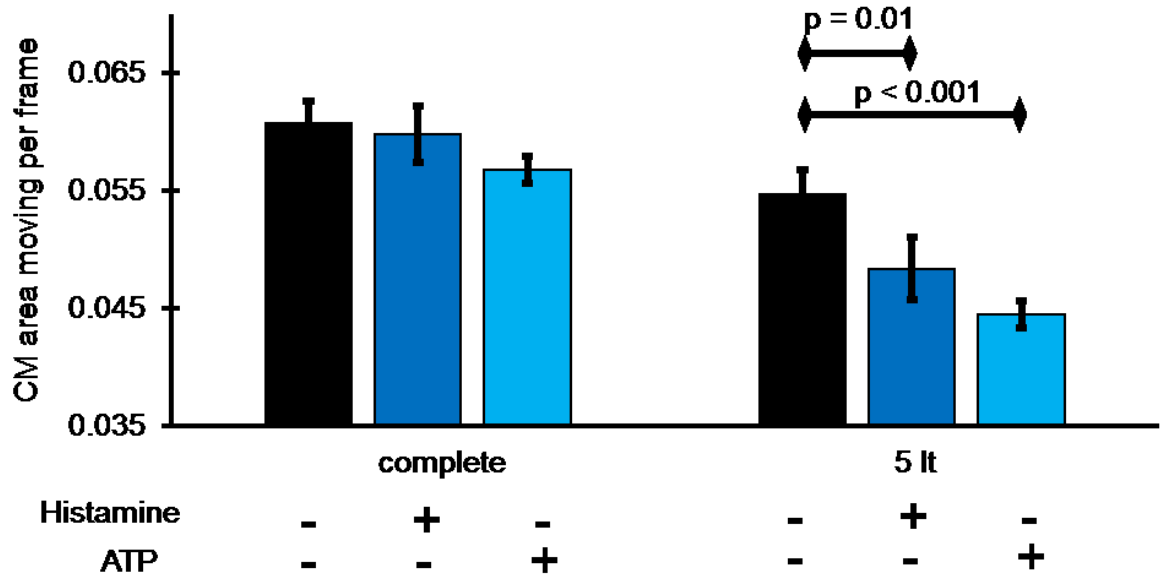

Figure 18: ***Differential IMM-dynamics in MAM and non-MAM mitochondrial regions upon histamine- or ATP-induced ER Ca^{2+} release*** *HeLa cells transfected with ER-RFP and stained with MTG, were treated with histamine (100 µM) or ATP (100 µM) to induce ER Ca^{2+} release. CM-dynamics of the whole IMM surface, as well as the area in close proximity to MAMs (5 iterations), were quantified. Images and analyses were obtained from at least 5 cells in each of the 8 experiments (n =8). Bars represent mean ± SEM. p vs. indicated conditions (ANOVA/Bonferonie post hoc)[88]. [Figure panels reproduced from Gottschalk et al., Pflügers Archiv - European Journal of Physiology 2018.]*

3.1.5 No further Ca^{2+}-induced CM deceleration was found under OPA1 knock-down

Furthermore, I investigated the influence of intracellular Ca^{2+} release on the CM-dynamics in cells depleted of OPA1. The knock-down of OPA1 in HeLa cells reduced the general dynamics in MAM-close and MAM-distinct CM (Fig. 9 &12), while no further effect of agonist-induced intracellular Ca^{2+} release on CM-dynamics was observed on the entire mitochondrion (Figure 19)[88].

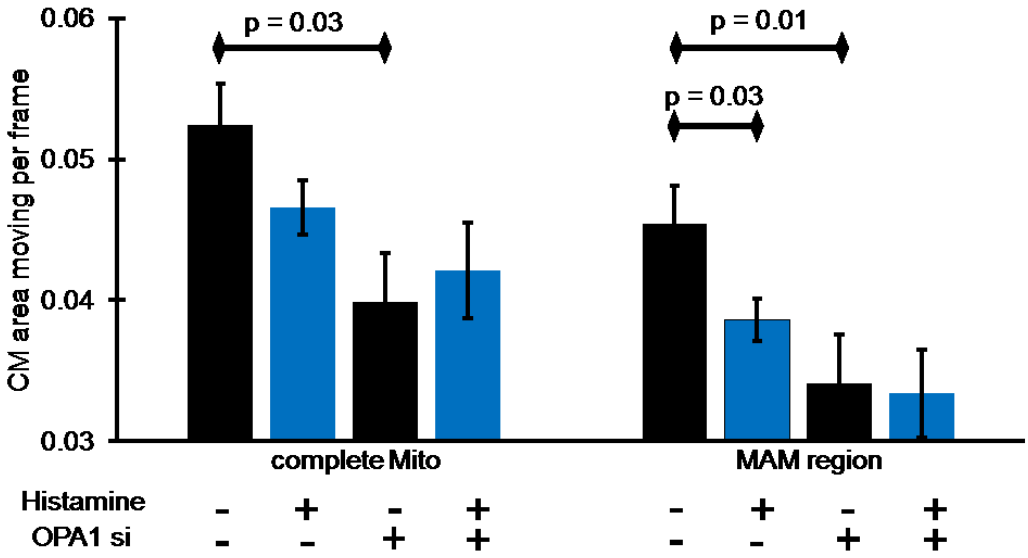

Figure 19: ***Impact of agonist induced ER Ca^{2+} release on IMM-dynamics in control cells and cells depleted from OPA1.*** *HeLa cells stained with MTG and transfected with ER-RFP and either Control siRNA or OPA1-specific siRNA were imaged with N-SIM. Histamine (100 µM) was added to induce ER Ca^{2+} release. CM-dynamics of the entire IMM surface and that of MAM-related areas (5 iterations) were quantified. Images and analyses were obtained from at least 5 cells in each of the 8 experiments (n = 8). Bars represent mean ± SEM. p vs. indicated conditions (ANOVA/Bonferonie post hoc)[88]. [Figure reproduced from Gottschalk et al., Pflügers Archiv - European Journal of Physiology 2018.]*

Hence, in OPA1-depleted cells, histamine-induced ER Ca^{2+} release did not affect mitochondrial branching *(Form factor)* (Figure 20)[88]. However, mitochondrial shape *(*aspect ratio) changed upon histamine stimulation independently of OPA1 expression (Figure 20). These data suggest that a general deceleration of the CM-dynamics in the entire mitochondrion (which is due to the broadening of the CJ induced by the lack of OPA1) cannot be further affected by intracellularly released Ca^{2+} [88].

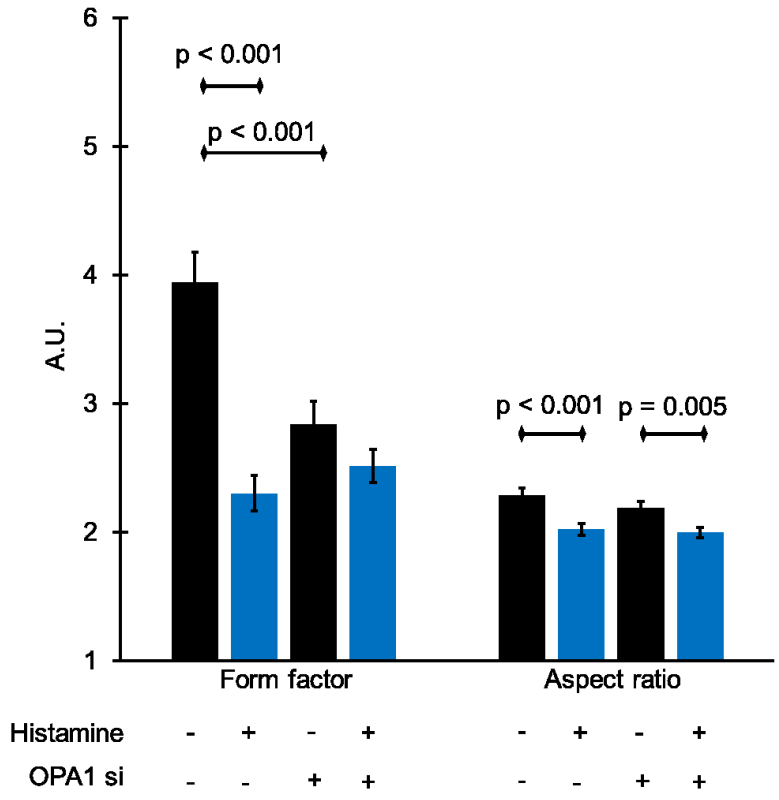

Figure 20: ***Silencing of OPA1 impacts the mitochondrial morphology in HeLa cells.*** *HeLa cells stained with MTG and transfected with ER-RFP and control or OPA1-specific siRNAs were imaged with N-SIM. Histamine (100 µM) was added to induce ER Ca^{2+} release. Form factor and aspect ratio were determined using ImageJ. Images and analyses were obtained from at least 5 cells in each of the 8 experiments (n= 8). Bars represent mean ± SEM. p vs. indicated conditions (ANOVA/Bonferonie post hoc)[88]. [Figure panels reproduced from Gottschalk et al., Pflügers Archiv - European Journal of Physiology 2018.]*

3.1.6 MICU1 knock-down leads to CM deceleration in MAM region

MICU1, having a Ca^{2+}-sensing EF-hand motif present in the IBM, was knocked down by siRNA, yielding under control conditions significant decreases of the CM-dynamics of the complete mitochondria as well as in mitochondrial regions in close proximity to the ER (Figure 21)[88]. Histamine treatment of MICU1 knock-down cells resulted in increased CM-dynamics in the complete mitochondria while in MAM-regions no changes compared to control conditions were observed (Figure 21)[88].

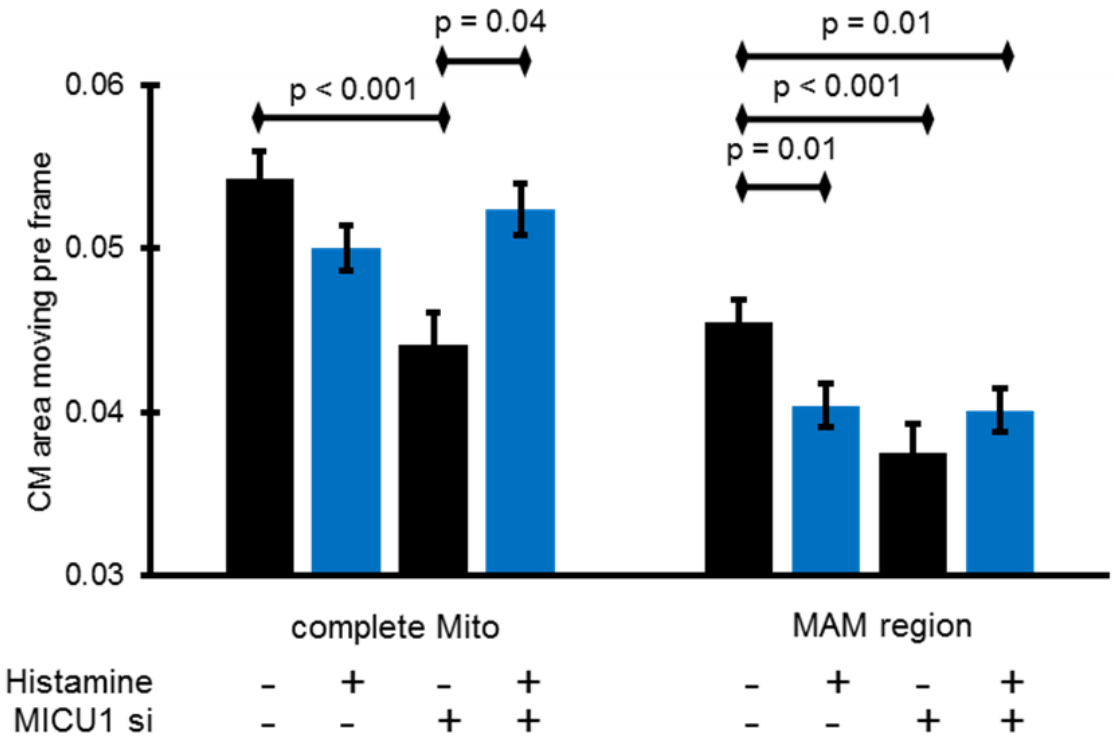

Figure 21: ***Impact of agonist-induced ER Ca^{2+} release on IMM-dynamics in control cells and cells depleted from MICU1.*** *HeLa cells stained with MTG and transfected with ER-RFP and either Control siRNA or MICU1-specific siRNA were imaged with N-SIM. Histamine (100 µM) was added to induce ER Ca^{2+} release. CM-dynamics of the entire IMM surface and that of MAM-related areas (5 iterations) were quantified. Images and analyses were obtained from at least 5 cells in each of the 8 experiments (n = 8). Bars represent mean ± SEM. p vs. indicated conditions (ANOVA/Bonferonie post hoc)[96]. [Figure reproduced from Gottschalk et al., Nature Communication 2019.]*

In MICU1-depleted cells, histamine-induced ER Ca^{2+} release did not affect mitochondrial branching *(Form factor)* while a significant change regarding the control condition could be observed (Figure 22)[88]. The mitochondrial shape *(*Aspect ratio) was not influenced by the MICU1 knock-down (Figure 22)[88].

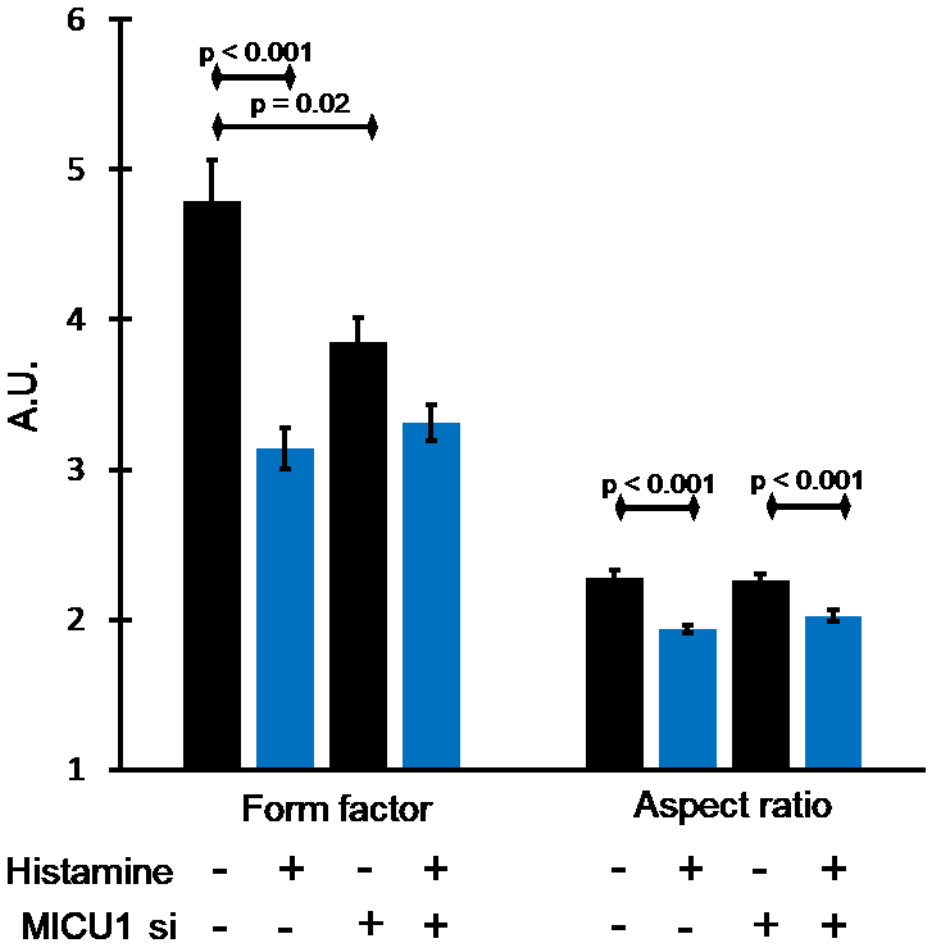

Figure 22: ***Silencing of MICU1 impacts the mitochondrial morphology in HeLa cells.*** *HeLa cells stained with MTG and transfected with ER-RFP and control or MICU1-specific siRNAs were imaged with N-SIM. Histamine (100 µM) was added to induce ER Ca^{2+} release. Form factor and aspect ratio were determined using ImageJ. Images and analyses were obtained from at least 5 cells in each of the 8 experiments (n = 8). Bars represent mean ± SEM. p vs. indicated conditions (ANOVA/Bonferonie post hoc)[96]. [Figure reproduced from Gottschalk et al., Nature Communication 2019.]*

3.1.7 Ca^{2+}-induced deceleration of CM does not require mitochondrial Ca^{2+} uptake

To verify whether or not mitochondrial Ca^{2+} uptake is required for the decrease in the kinetics of MAM-close CM, mitochondrial Ca^{2+} influx was prevented by siRNA-mediated diminution of the expression of MCU. Knock-down of MCU had no impact on the effect of intracellularly released Ca^{2+} on global mitochondrial and MAM-related CM-dynamics (Figure 23)[88]. These findings indicate that the Ca^{2+}-induced inhibition of MAM-close CM-kinetics is independent of mitochondrial Ca^{2+} uptake[88].

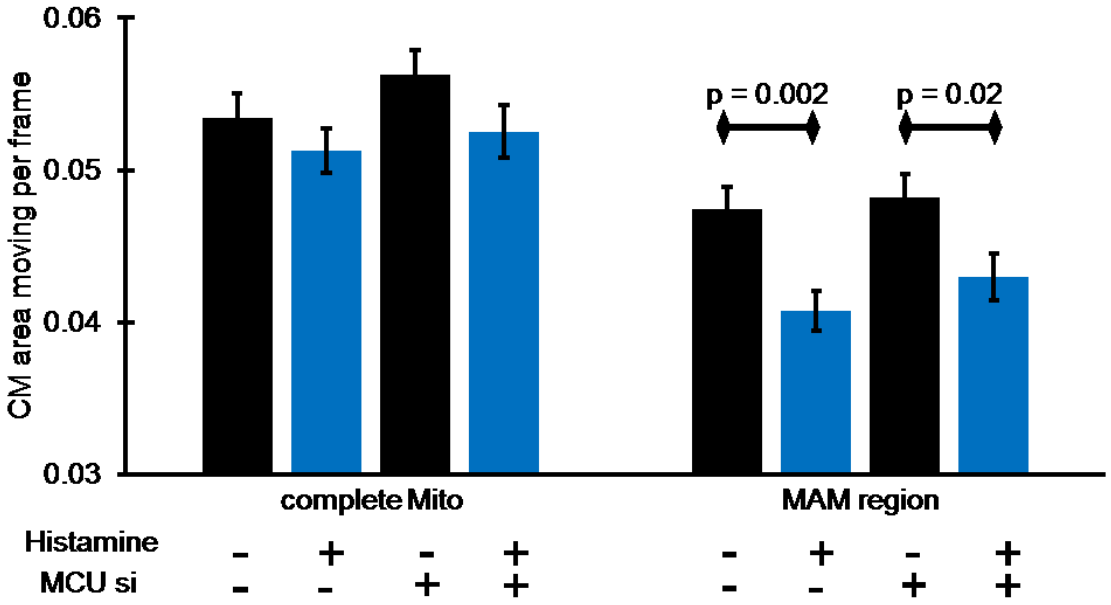

Figure 23: ***Elevations in matrix Ca^{2+} are not involved in ER-Ca^{2+}-release-mediated deceleration of CM in the proximity of MAMs.*** *HeLa cells stained with MTG and transfected with either ER-RFP and Control siRNA or MCU-specific siRNA were imaged with N-SIM. Histamine (100 µM) was added to induce ER Ca^{2+} release. CM-kinetics of the entire IMM surface and that of MAM-related area (5 iterations) were quantified. Images and analyses were obtained from at least 5 cells in each of the 8 experiments (n = 8). Bars represent mean ± SEM. p vs. indicated conditions (ANOVA/Bonferonie post hoc)[88]. [Figure reproduced from Gottschalk et al., Pflügers Archiv - European Journal of Physiology 2018.]*

Hence, depletion of MCU did not affect mitochondrial shape (Aspect ratio) or histamine-influenced mitochondrial branching (Form factor) (Figure 24), thus indicating that Ca^{2+}-induced changes in mitochondrial shape do not require Ca^{2+} influx into the organelle[88].

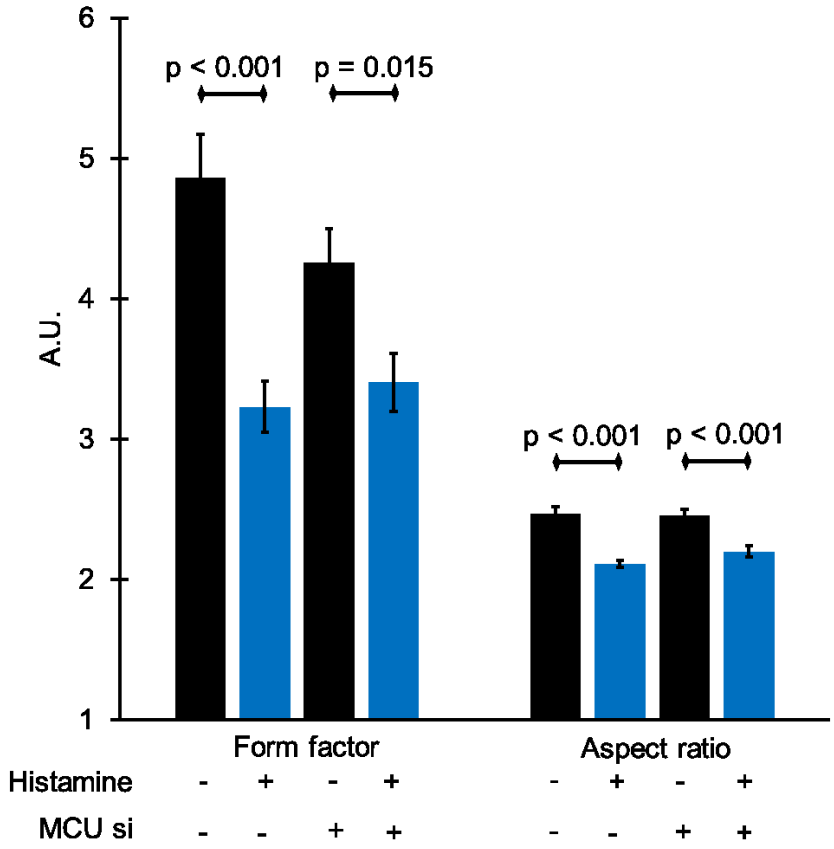

Figure 24: ***Silencing of MCU does not influence mitochondrial morphology in HeLa cells.*** *HeLa cells stained with MTG and transfected with ER-RFP and control or MCU-specific siRNA were imaged with N-SIM. Histamine (100 µM) was added to induce ER Ca^{2+} release. Form factor and aspect ratio were determined using ImageJ. Images and analyses were obtained from at least 5 cells in each of the 8 experiments (n = 8). Bars represent mean ± SEM. p vs. indicated conditions (ANOVA/Bonferonie post hoc)[88]. [Figure reproduced from Gottschalk et al., Pflügers Archiv - European Journal of Physiology 2018.]*

3.2 **MICU1 controls the mitochondrial cristae junction**

The second part of the results section is based on my first author publication (Gottschalk et al. 2019). Dual-color structured illumination microscopy was used to localize MICU1 to the IBM. Further, time lapse imaging and different clones of MICU1 were used to determine which physical properties restrict MICU1 to the IBM and whether the cristae junction is impacted by the occurrence of MICU1.

3.2.1 MICU1 is located to the IBM

HeLa cells expressing MICU1-yellow fluorescent protein (YFP) were stained with Mitotracker Red CMXROS® (MTR-CMX). Then super-resolution images were obtained under resting conditions to compare with images captured after stimulation with histamine, which causes intracellular Ca^{2+} release. These experiments established that MICU1 exclusively localizes to the IBM, and that this distribution does not change in response to histamine (Figure 25). Cells co-expressing both MICU1-YFP and a homolog for the mitochondrial import receptor subunit TOM22 (marker specific for the OMM) fused to the fluorophore mCherry (mCherry-TOM22) were analyzed with SIM to further establish that MICU1 is confined to the IBM. By analyzing the cross section intensity profiles of the two fluorescence channels, a distance of 22 ± 13 nm (mean ± SD) was calculated between the distributions of MICU1 and TOM22 (Figure 25) [96].

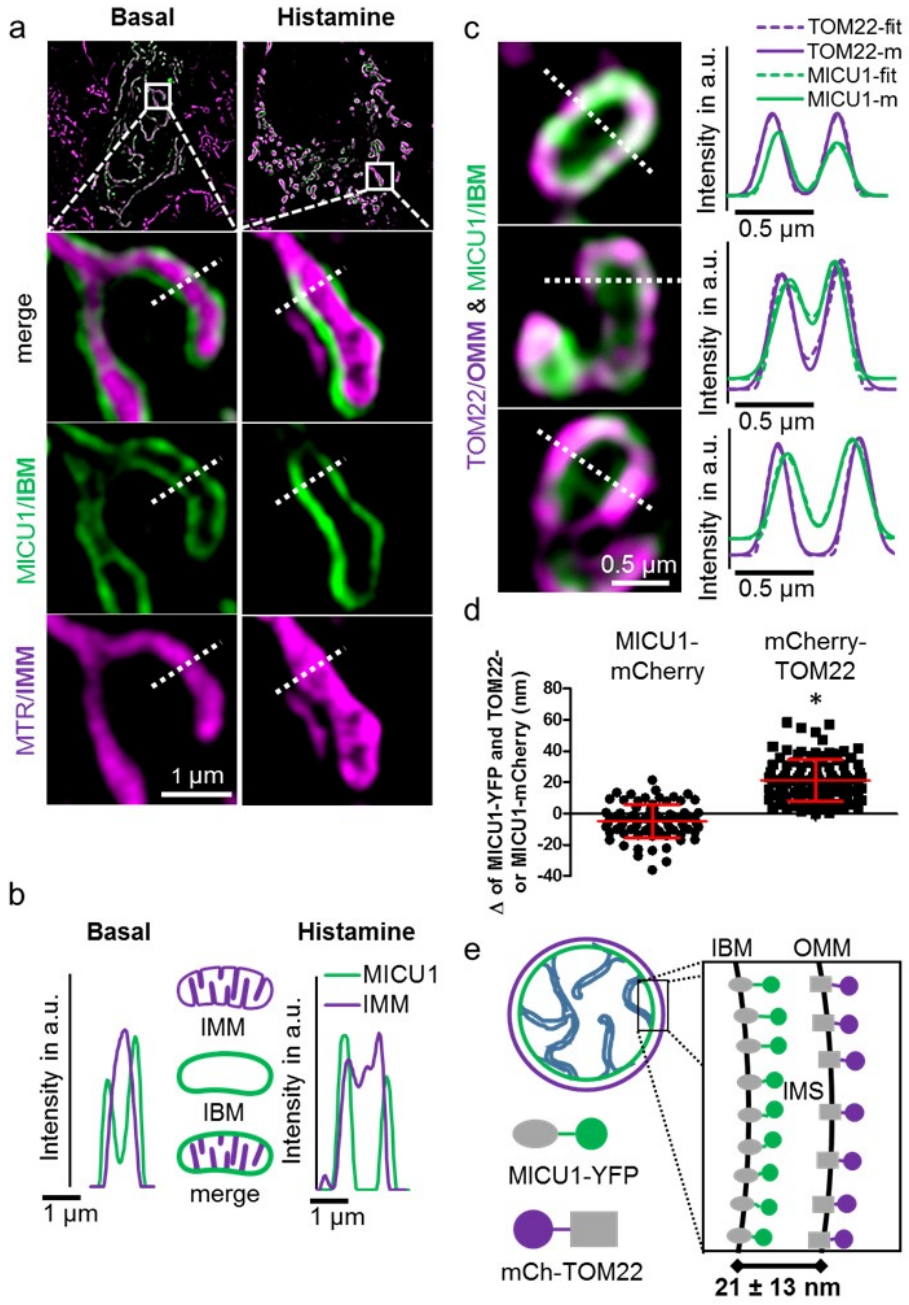

Figure 25: ***Super-resolution SIM microscopy localizes MICU1 to the IBM.*** *(a) Cells were transiently transfected with MICU1-YFP (green), then stained with Mitotracker Red FM® (MTR) (magenta) and examined using simultaneous dual-color 3D-SIM either under resting conditions, or 4 min after stimulation with 100 µM histamine. The upper panels provide an overall view of the mitochondria, and the dashed squares indicate the regions shown magnified below. The figures show merges of MICU1-YFP and MTR, along with MICU1-YFP (MICU1) and IMM (MTR) signals alone. No changes in the distribution of MICU1-YFP (nor IMM staining) were observed upon stimulation with histamine. (b) Line plots of MICU1 and the IMM staining with MTR of regions marked with dashed white lines in (a) are shown. A clear sub-mitochondrial localization of MICU1 to the IBM is visible. (c) HeLa cells transfected with MICU1-YFP (green) and mCherry-TOM22 (magenta) were imaged using simultaneous dual-color 3D-SIM. Left panels show representative images. Right panels show line plots through mitochondria at locations indicated by the white dashed lines. By subjecting both channels (m) to a double Gaussian fit for each individual line (fit) (right panels), the peaks of both distributions could be determined with subpixel accuracy.(d) Quantification of ΔΔdistances of MICU1-YFP and MICU1-mCherry or mCherry-TOM22 fluorescence distributions. (e) Schematic illustration of the mitochondrial inner boundary membrane and outer membrane showing the determined spacing between MICU1 and TOM22 of 21 ± 13 nm (Mean ± SD). This value matches published distances between the OMM and IMM (lower right). Images and analyses were obtained from 4 - 5 mitochondria in at least 3 cells in each of 8 independent experiments ($n_{mCherry\text{-}TOM22}$ = 8/24/105, $n_{MICU1\text{-}mCherry}$ = 8/40/80). *P>0.05 vs. respective control conditions (two sided unpaired t-test)[96]. [Figure reproduced from Gottschalk et al., Nature Communications 2019.]*

More detailed analyses of MICU1 and TOM22 peak-to-peak distances are shown in Figure 26. Both distributions of TOM22 and MICU1 are shown as pairs per mitochondrion measured. A clear trend is visible showing almost a bigger diameter for the TOM22 labeling then for the MICU1 distribution. Mitochondria analyzed were approximately 350 ± 91 nm (mean ± SD) in diameter, using TOM22 as reference (Figure 26) [96].

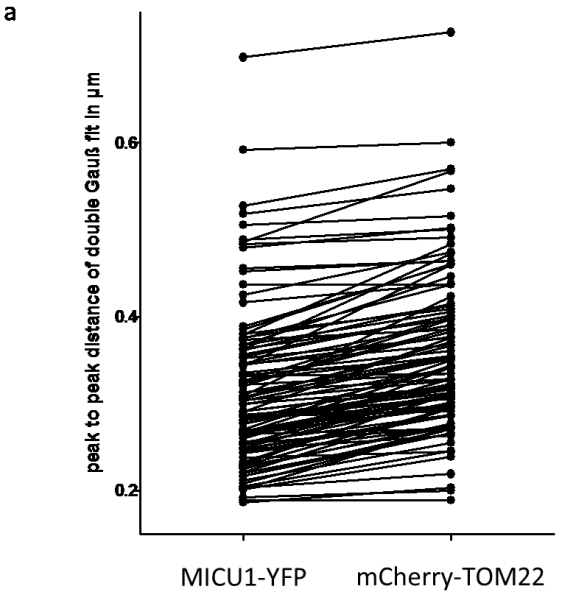

	MICU1-YFP	mCherry-Tom22
Number of values	105	105
Minimum	0.1863 µm	0.1892 µm
25% Percentile	0.2506 µm	0.2953 µm
Median	0.2991 µm	0.3407 µm
75% Percentile	0.3625 µm	0.4072 µm
Maximum	0.6982 µm	0.7271 µm
Mean	0.3171 µm	0.3596 µm
Std. Deviation	0.09390 µm	0.09390 µm
Std. Error	0.009163 µm	0.009164 µm
Lower 95% CI of mean	0.2990 µm	0.3414 µm
Upper 95% CI of mean	0.3353 µm	0.3777 µm

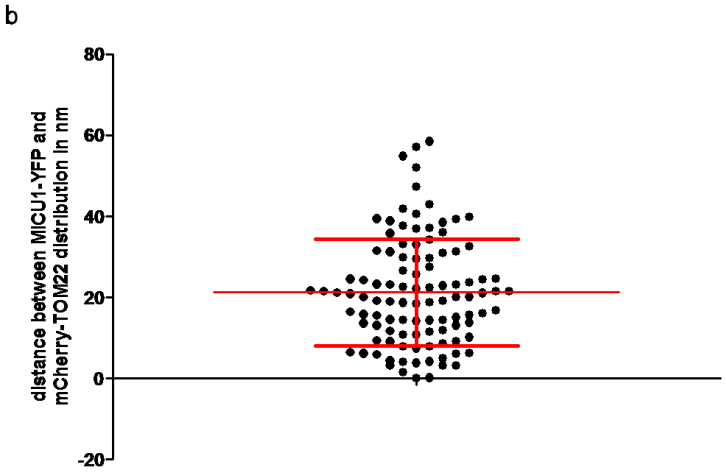

Number of values	105
Minimum	-0.01126 nm
25% Percentile	11.10 nm
Median	20.07 nm
75% Percentile	30.37 nm
Maximum	58.40 nm
Mean	21.21 nm
Std. Deviation	13.22 nm
Std. Error	1.290 nm
Lower 95% CI of mean	18.65 nm
Upper 95% CI of mean	23.76 nm

Figure 26: ***Detailed statistical analysis of MICU1-YFP and mCherry-TOM22 sub-mitochondrial distribution and spatial relation.*** *HeLa cells were transfected with MICU1-YFP and mCherry-TOM22 constructs and imaged with Dual-SIM. (a) (left panel) Peak-to-peak distances of double Gaussian fit of MICU1 and TOM22 line plots were calculated and displayed as pairs. (Right panel) Detailed statistical listing of MICU1-YFP and mCherry-TOM22 peak-to-peak distance distribution. (b) (Left panel) The delta of the peak-to-peak distances of MICU1 and TOM22 line plots were calculated. (Right panel) Detailed statistical listing of the delta between MICU1-YFP and mCherry-TOM22 peak-to-peak distance distribution. Analyses were obtained from 4 - 5 mitochondria in at least 3 cells in each of 8 independent experiments (n = 8/24/105).[96]. [Figure reproduced from Gottschalk et al., Nature Communications 2019.]*

To ensure that the overexpression of MICU1 did not influence mitochondrial morphology, I directly compared HeLa mitochondrial morphology with and without MICU1-YFP expression using 3D confocal microscopy. I could not observe any changes regarding mitochondrial volume, surface, elongation or flatness (Figure 27)[96].

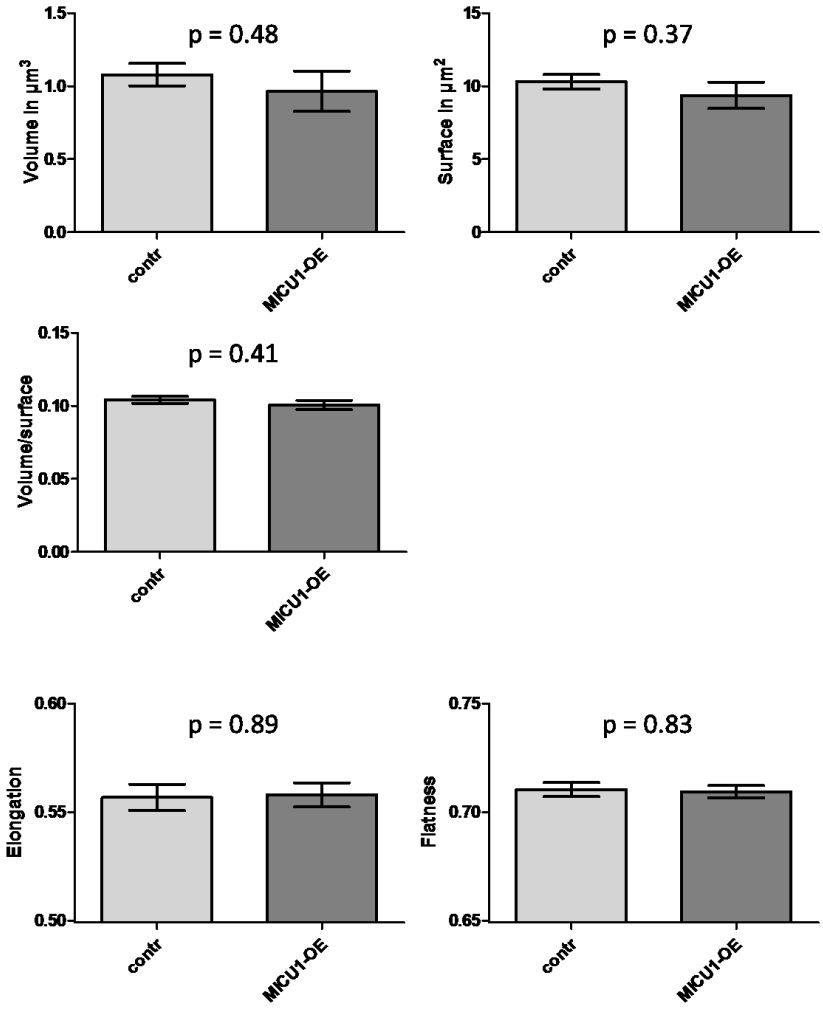

Figure 27: ***MICU1-YFP expression does not change mitochondrial morphology in HeLa cells.*** *HeLa cells transfected with and without MICU1-YFP were stained with MTR. Z-stacks were acquired, blind deconvoluted, background-subtracted (rolling ball method, ImageJ) and analyzed for mitochondrial volume, surface, elongation, and flatness. No significant changes in the mitochondrial morphology between MICU1-YFP and untransfected cells could be measured (n = 9). *P>0.05 vs. respective control conditions (two sided unpaired t-test)[96]. [Figure reproduced from Gottschalk et al., Nature Communications 2019.]*

3.2.2 Characterizing the microscopic setup with regard to spatial inter-color resolution

To ensure that the measurements of mCherry-TOM22 and MICU1-YFP distribution (Figure 25 & Figure 26) were not impacted by chromatic aberration, measurements with 100 nm sized Tetraspec beads were made to analyze the quality and power of the microscopic setup (Figure 28) [96].

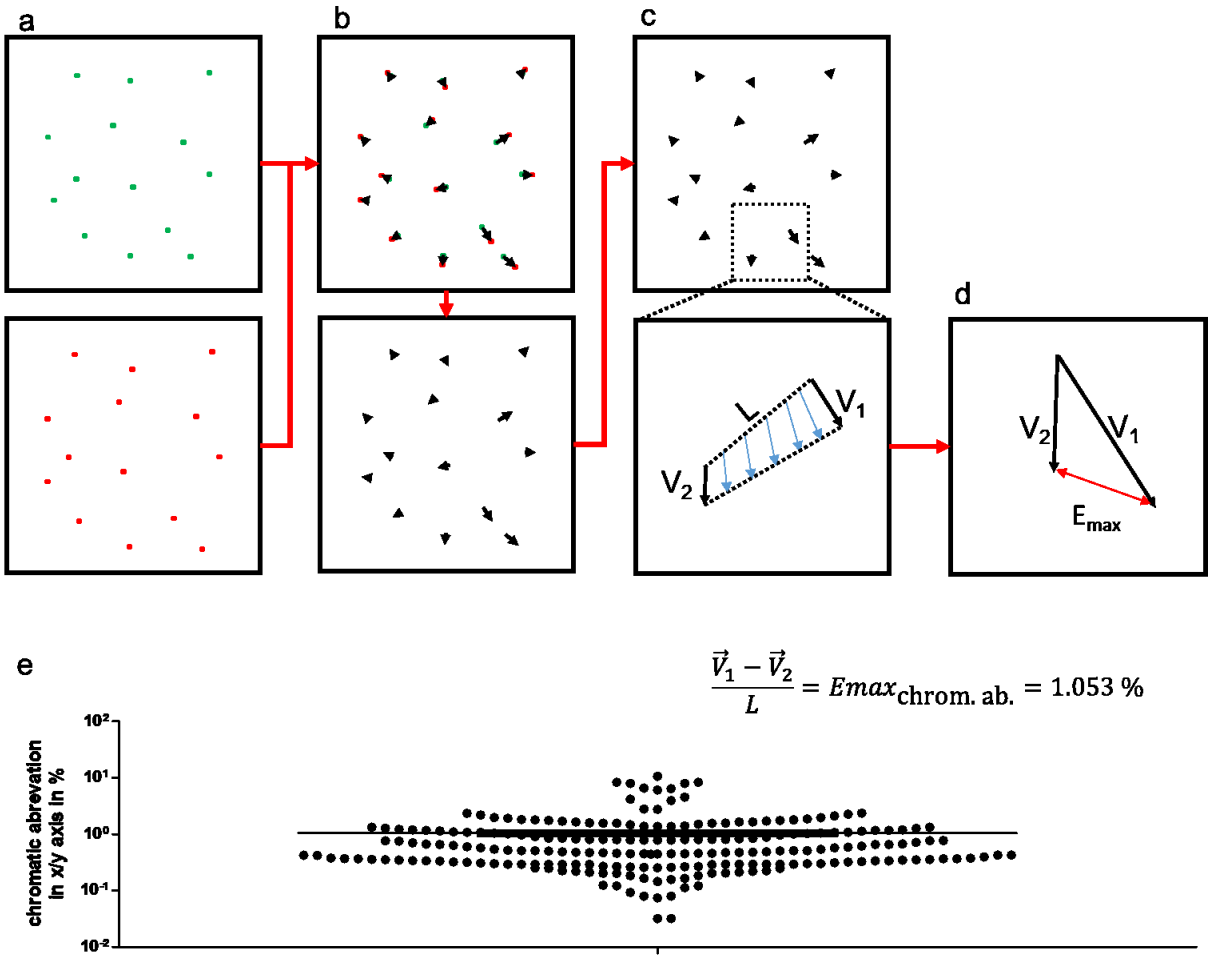

Figure 28: ***Schematic representation of Tetraspec bead measurements to identify the influence of chromatic aberrations on the conducted N-SIM measurements.*** *100 nm Tetraspec beads were immobilized using poly-L-lysine on 1.5H high precision glass cover slips. (a) The Tetraspec beads were imaged using the Two-CAM system and illuminated simultaneously with 488 and 561 nm lasers. (b) Bead pairs in both channels were identified, localized with subpixel accuracy and each pair got a vector assigned describing the local special chromatic abbreviation. (c) The closest neighbor of each bead was identified and the distance (L) was calculated using the green channel. (d) The vector difference of both beads was calculated and normalized to their distance. (e) A mean relative error of 1.053 % was calculated to be the systemic error introduced by chromatic abbreviations. Measuring a peak-to-peak distribution of MICU1-YFP or mCherry-TOM22 of 350 nm with the given setup would result in a systemic error introduction of approximately 3.5 nm. Data are shown as dot plots with the mean +/-SEM as middle line and whiskers, respectively (n = 210)[96]. [Figure reproduced from Gottschalk et al., Nature Communications 2019.]*

By comparing both color channels used, an error of approximately 1 % in measurement accuracy between the 488 and 561 illumination channels was found (Figure 28). This corresponds to 3.5 nm deviation regarding the measurement of a mitochondrion with a diameter of 350 nm, which was measured as the mean mitochondrial diameter (Figure 26) [96].

Since a chromatic aberration in z might affect the peak-to-peak measurements performed for mCherry-TOM22 and MICU1-YFP, the model system of a mitochondrion had to be defined (Figure 29). In this work, the mitochondrion is represented model-wise as a hollow cylinder with the outer barrel being the OMM and the inner barrel the IBM. The cylindrical shape with a diameter of 350 nm was convolved with the simplified PSF (Gaussian distribution) of the microscope. Changing the focal plane from the middle of the mitochondrion 100 nm up or down results in a narrowed peak-to-peak distance of the x-projection line plot (Figure 29) [96].

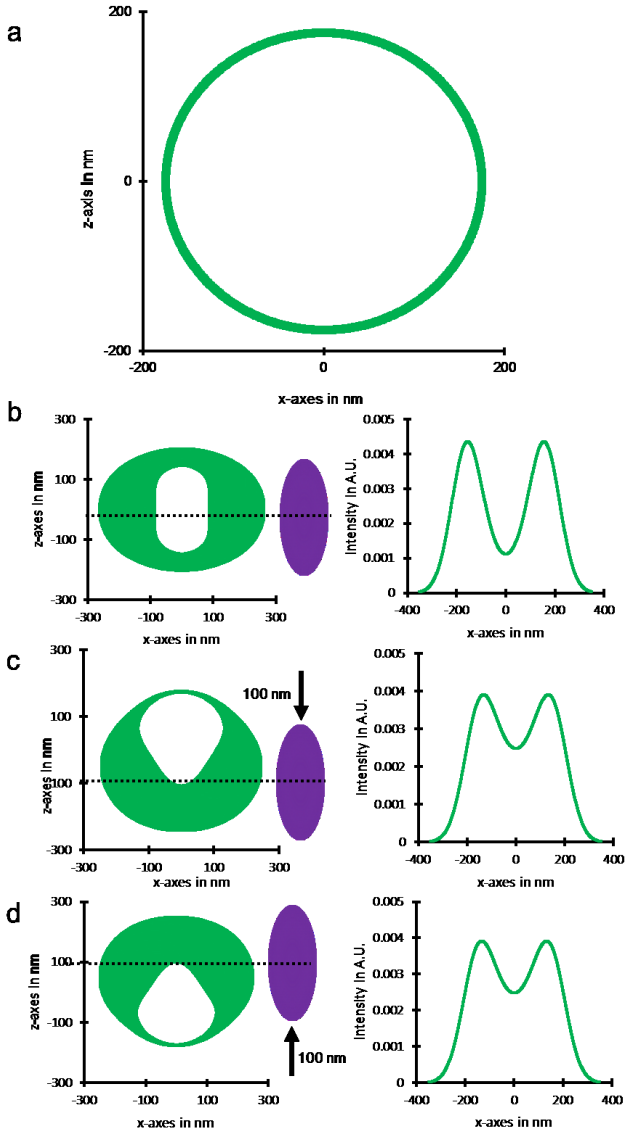

Figure 29: ***Model of the influence of the focus plane on mitochondrial line plots.*** *(A) To evaluate if a different focus plane would change the line plot characteristics of mCherry-TOM22 or MICU1-YFP staining I chose as a model a hollow cylinder with a superficial fluorescent label. (B) The convolution of a hollow cylinder model with the simplified point spread function (magenta ellipse; $FWHM_{x,y}$ = 140 nm; $FWHM_z$ = 260 nm) of the SIM-system in the center of the mitochondrion (black dotted line) yields an inhomogeneous but symmetrical fluorescence detection. This results in an x-projection showing a double peak structure. (C, D) Shifting the focus plane (black dotted line) 100 nm up or down results in inhomogeneous and asymmetrical fluorescence detection and yields a narrower double-peak structure of the x-projection line plot* [96]*. [Figure reproduced from Gottschalk et al., Nature Communications 2019.]*

Further, the chromatic aberration in z was determined with Tetraspec beads. A shift of 45 nm between the 488 and 561 illumination channel was measured. Simulation of the focal plane of the objective in the middle of the mitochondrion leads to a minor shift in peak-to-peak distance of the x-axes projection line plot of 1.59 nm (Figure 30). Shifting the focal plane up or down leads to much more serious changes. However, as the actual focal plane of each image in

relation to the mitochondrial center along the z-axes cannot be determined, despite that during the imaging process, the mitochondria were focused manually as well as possible, as standard distribution around the center can be assumed (Figure 30). This leads to the fact that the mean deviation between the two channels is equal to the deviation at the focal plane of the microscope objective [96].

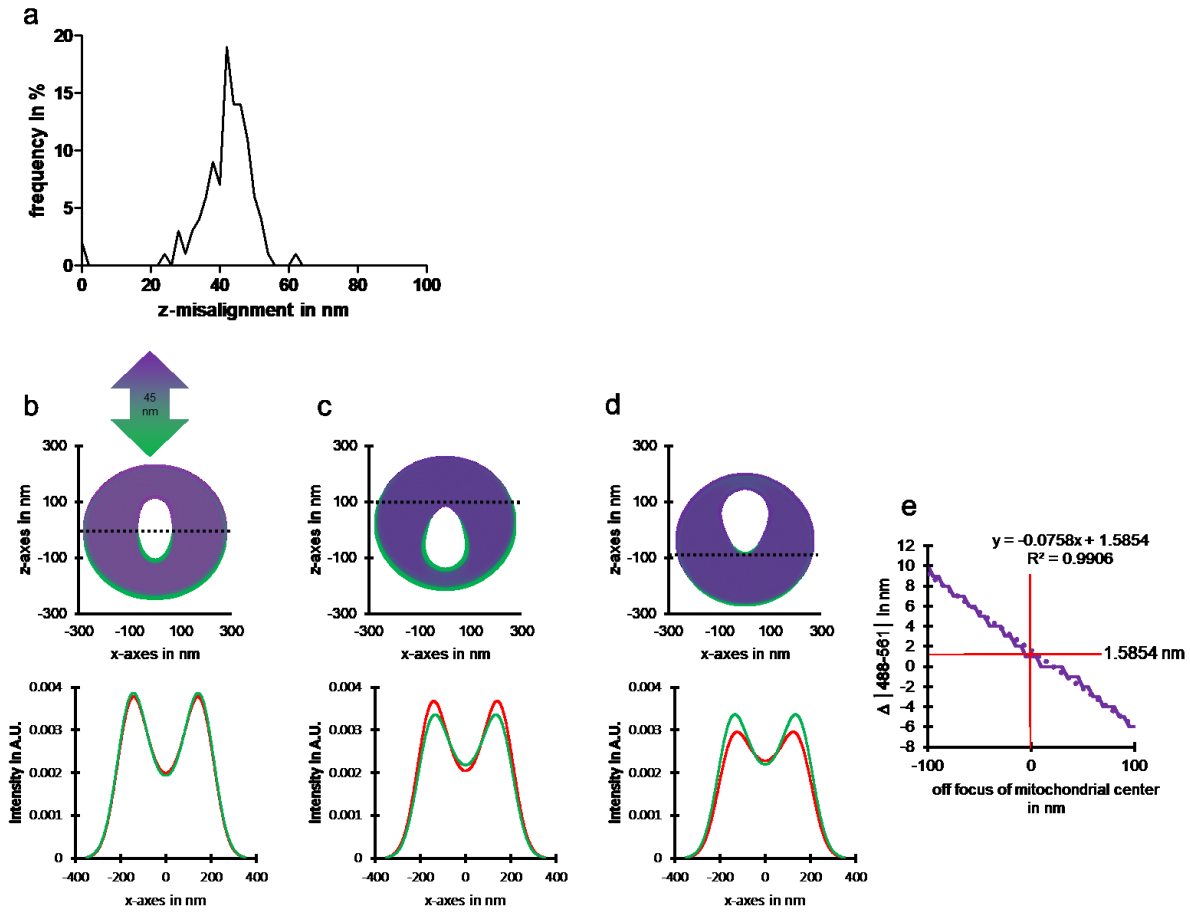

Figure 30: ***Measurement of chromatic aberrations along the z-axes and analysis of the influence on peak-to-peak measurements.*** *(a) Z-stacks of Tetraspec beads were acquired and the z-displacement between both channels was calculated by fitting the z-intensity projection to a Gaussian curve to determine the sub-pixel localization of the bead along the z-axes. The delta in position between both channels was plotted and the mean of 45 nm was used for further calculations. (b-d) Setting the 561 channel (magenta) as a reference and applying a point spread function with a delta along the z-axes of 45 nm to the 488 channel (green) results in a different fluorescence detection pattern resulting in a change of the x-projection line plot and peak-to-peak distance. These changes in fluorescence detection, and peak-to-peak distance appear to be more severe if the focal plane is shifted 100 nm up or down. (e) Modeling the delta of peak-to-peak distances between the 488 and 561 channel dependent on the off-focus in small increments of 5 nm and applying a linear fit leads to a good estimation of the error introduced by chromatic abbreviations along the z-axes. As the focus relative to the mitochondria can be estimated as normally distributed around the center, a standard error of approximately 1.6 nm can be applied [96]. [Figure reproduced from Gottschalk et al., Nature Communications 2019.]*

3.2.3 MICU1 is bound to the IBM by its poly-lysine-domain

To quantify the sub-mitochondrial distribution of wild-type MICU1 as well as MICU1$^{1-140}$ and MICU1$^{1-70}$ mutants, a custom-made macro was written in ImageJ (Fiji) (Material and Methods 2.22; page 34). The macro determines the intensity distribution of a selected analyte between the IBM and the CM of the mitochondrion. It needs a fluorescent label that does not change sub-mitochondrial localization as a reference (Figure 31) [96].

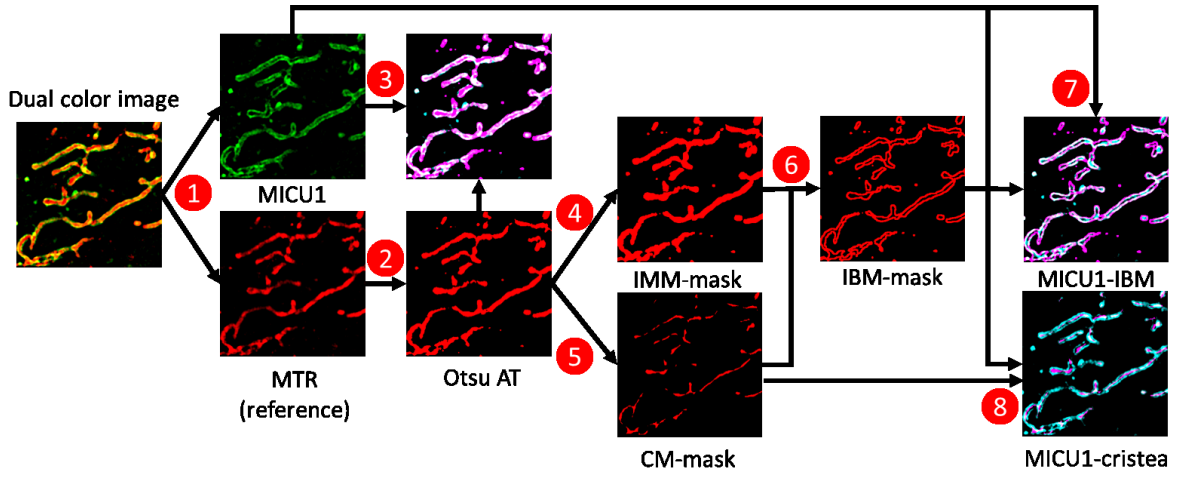

Figure 31: ***Image analysis scheme and description for the differentiation of the sub-mitochondrial protein localization.*** *Dual-color 3D-SIM images were split up into a reference and an object channel. The reference channel (MTR in this particular case) gets Otsu auto-thresholded, followed by both a dilation and erosion. Subtracting the eroded images from the dilated gives a hollow tube binary mask. The mean fluorescence intensity measured within the hollow tube mask divided by the mean fluorescence intensity measured within the eroded binary mask yields a ratio expressing the sub-mitochondrial localization. The lower the ratio, the higher the CM and the lower the IBM localization. A high ratio indicates a high IBM and low CM protein distribution [96]. [Figure reproduced from Gottschalk et al., Nature Communications 2019.]*

To elucidate whether the poly-lysine domain of MICU1 plays an important role in maintaining its IBM-localization, both MICU1$^{1-140}$-YFP and MICU1$^{1-70}$-YFP mutants were expressed in MTR-stained HeLa cells (Figure 32). The quantitative analysis revealed a clear sub-

mitochondrial localization of the MICU1$^{1-140}$-YFP to the IBM while the MICU1$^{1-70}$-YFP was distributed mainly to the cristae (Figure 32) [96].

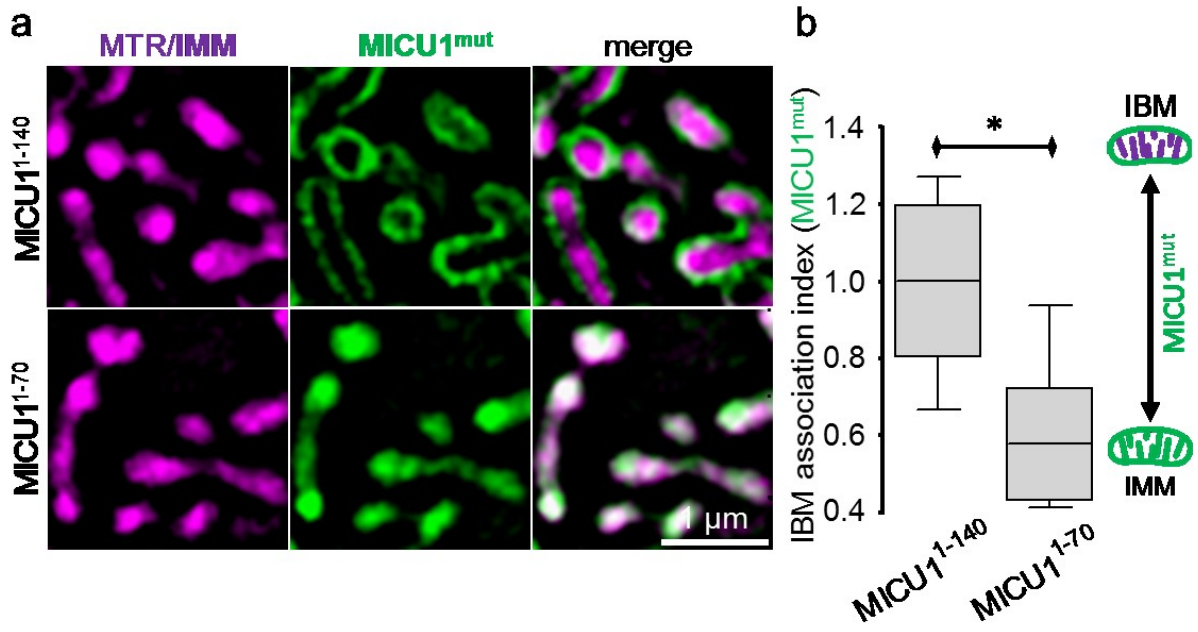

Figure 32: ***Poly-lysine domain of MICU1 is necessary for IBM localization of MICU1.*** *(**a**) Representative Dual-SIM images of HeLa cells stained with MTR (magenta) and expressing MICU1$^{1-140}$-cpEGFP (green, upper panel) or MICU1$^{1-70}$- cpEGFP (green, lower panel). (**b**) Respective statistical analyses of the IBM association index of MICU1$^{1-140}$ and MICU1$^{1-70}$. The sub-mitochondrial distribution of MICU1$^{1-140}$ and MICU1$^{1-70}$ in the IBM and the CM was determined with the IBM association index in these experiments. . Images and analyses were obtained from n = 9 independent experiments, which assessed a total of 45 cells. *P< 0.05 vs. respective control conditions carried out with unpaired double-sided T-test[96]. [Figure reproduced from Gottschalk et al., Nature Communications 2019.]*

HeLa cells were transfected with MICU1-YFP and EMRE-mCherry. Time-lapse experiments were performed applying oligomycin A and antimycin A to the cells. After the application of antimycin A, a fast redistribution of MICU1-YFP could be observed (Figure 33). By taking line plots in between the indicated arrows in Fig. 19 (*left panel*), clear delocalization from the IBM to the cristae can be observed (Figure 33). By determining the ratio of the MICU1-YFP mean IBM intensity and the mean cristae intensity over time, a sharp drop into the cristae localization shortly after the addition of antimycin A could be observed (Figure 33). To confirm a drop in membrane potential, measurements with TMRM were performed indicating a clear drop of the mitochondrial membrane potential after the addition of antimycin A (Figure 33) [96].

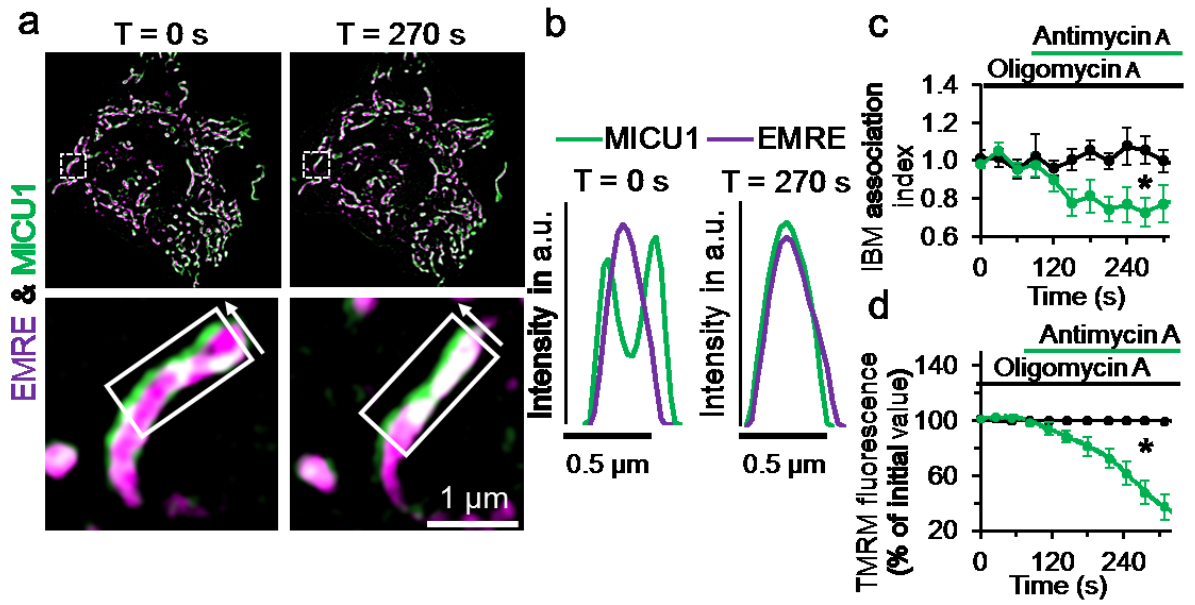

Figure 33: ***High mitochondrial membrane potential and the C-terminal region of MICU1 are required for localizing the protein in the IBM.*** *SIM time-lapse experiments were performed using Hela cells transiently transfected with MICU1-YFP and EMRE-mCherry. Cells were pre-incubated with oligomycin A (2 µM) for 2 min, and image collection began 90 s prior to the addition of antimycin A (4 µM). (a) A representative cell is shown at the time points 0 and 270 s. (b) displays intensity line plots for both fluorescence channels, which were measured in the arrowed boxes indicated in the super-resolved SIM image. (c) A time-course of the IBM association index following pre-incubation with oligomycin A with and without exposure to antimycin A starting at t = 90 s. (nControl=7;nOligomycin/Antimycin=9). Data are shown as the mean ± SEM (d) Corresponding tetramethylrhodamine methyl ester perchlorate (TMRM) fluorescence, which indicates the mitochondrial membrane potential, was imaged using a conventional microscope (nAntimycin=8;nAntimycin/Oligomycin=9). *P<0.05 vs. respective control conditions (two sided unpaired t-test)*[96]*. [Figure reproduced from Gottschalk et al., Nature Communications 2019.]*

Mitochondrial morphology was not altered by oligomycin A or antimycin A treatment of HeLa cells. None of the mitochondrial count, the aspect ratio or form factor changed over time. Mitochondrial integrity was maintained and no fragmentation was observed (Figure 34) [96].

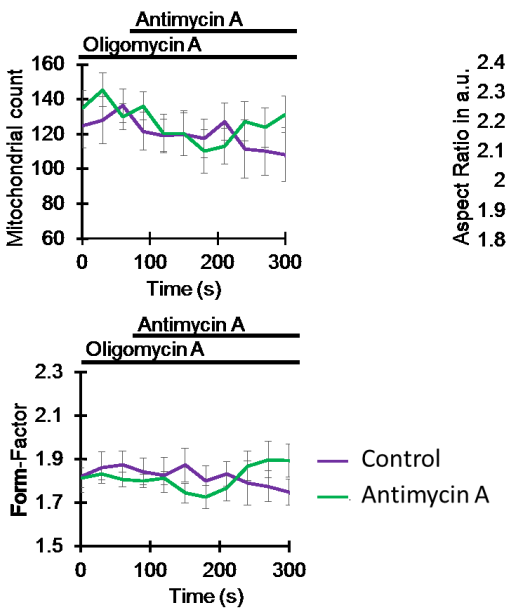

Figure 34: ***Antimycin A and oligomycin A treatments do not affect mitochondrial morphology.*** *The EMRE-mCherry fluorescence was used to confirm mitochondrial integrity over time. None of the observed characteristics was changed significantly after antimycin A addition over time. ($n_{Antimycin}$ = 8; $n_{Antimycin/Oligomycin}$ = 9).Data are shown as mean +/- SEM.* = P<0.05vs. respective control conditions calculated with unpaired double sided T-Test[96]. [Figure reproduced from Gottschalk et al., Nature Communications 2019.]*

As the reorganization of MICU1-YFP during cell treatment with oligomycin A and antimycin A might be related to protein degradation, Western blot experiments were performed to examine whether MICU1-YFP gets degraded. This control experiment verified no MICU1 degradation even after HeLa cells were incubated for 10 min with oligomycin A and antimycin A (Figure 35) [96].

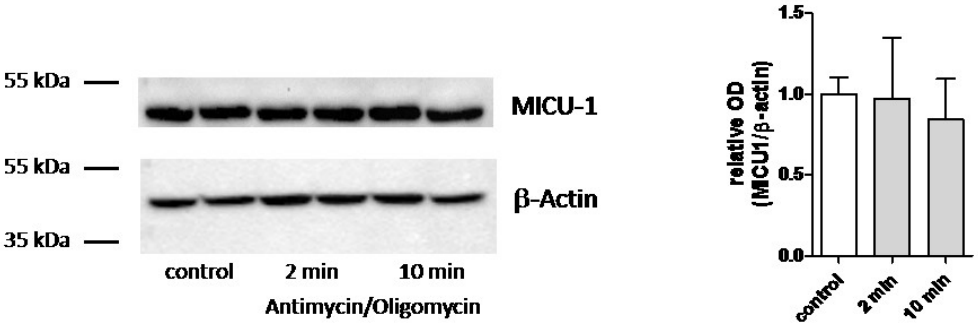

Figure 35: ***MICU1 does not undergo proteolytic cleavage during antimycin A and oligomycin A treatment.*** *HeLa cells transfected with MICU1-YFP were treated for 2 or 10 min with antimycin/oligomycin, and subsequently lysed and analyzed for expression of MICU1 using Western blotting. No antimycin/oligomycin-related degradation was observed. (n=4) [96] [Figure reproduced from Gottschalk et al., Nature Communications 2019.]*

Reportedly, MICU1 interacts with cardiolipin[20], a phospholipid exhibiting high abundance in mitochondria. Therefore, it was tested if a lack of cardiolipin had an influence on the sub-mitochondrial localization of MICU1. Taffazin, an essential enzyme in cardiolipin synthesis and maturation, was silenced in HeLa cells. Knock-down efficiency was determined by qRT-PCR to be approximately 50 % (*Figure 36*). MICU1-YFP expressed in HeLa cells silenced for taffazin showed an abnormal sub-mitochondrial distribution throughout the IMM in contrast to the IBM localization observed under control conditions (*Figure 36*). Further, a slight reduction in mitochondrial form factor could be observed under conditions of taffazin knock-down, indicating mitochondrial fragmentation (*Figure 36*) [96].

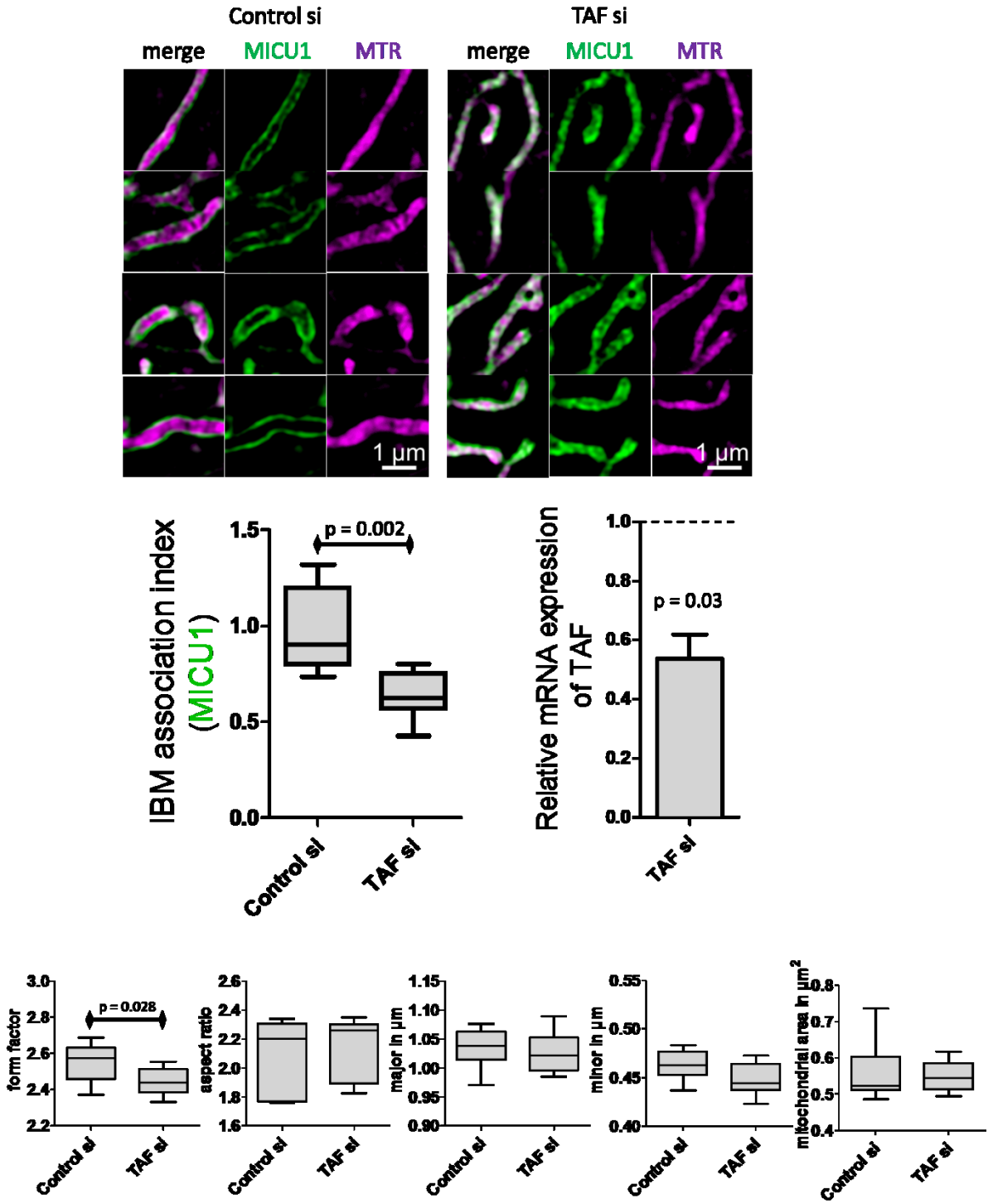

Figure 36: ***Knock-down of Taffazin (TAF) leads to reorganization of MICU1 throughout the whole IMM.*** *HeLa cells transfected with MICU1-YFP and control or TAF siRNA were imaged using structured illumination microscopy. The IBM association factor, as well as mitochondrial morphology, were extracted from the imaging data (n = 9). To verify the knock-down efficacy, qRT-PCR was conducted for control and TAF siRNA-transfected cells (n = 3). P-values presented in the figure are calculated with unpaired double sided T-Test[96]. [Figure reproduced from Gottschalk et al., Nature Communications 2019.]*

3.2.4 The C-terminal domain of MICU1 is involved in IBM localization of MICU1

Because MICU1 can exist either as a hexamer or as a dimer[97], I examined whether the quaternary structure also contributes to its distribution. To do so, a ΔC-MICU1-YFP mutant, which lacks the oligomerization site, was expressed in cells that were depleted of endogenous MICU1. In contrast to the wild-type, the ΔC-mutant was not confined to the IBM but rather was distributed throughout the inner membrane (Figure 37). However, in the presence of endogenous MICU1, the ΔC-mutant occurs only in the IBM (Figure 37). Furthermore, while the wild-type MICU1-YFP localized to the IBM under OPA1 knock-down, the ΔC-mutant occurs only in the cristae (Figure 37). However, all three mutants F-mut, K-mut, and EF-mut showed the same IBM localization as the wild-type (Figure 37) [96].

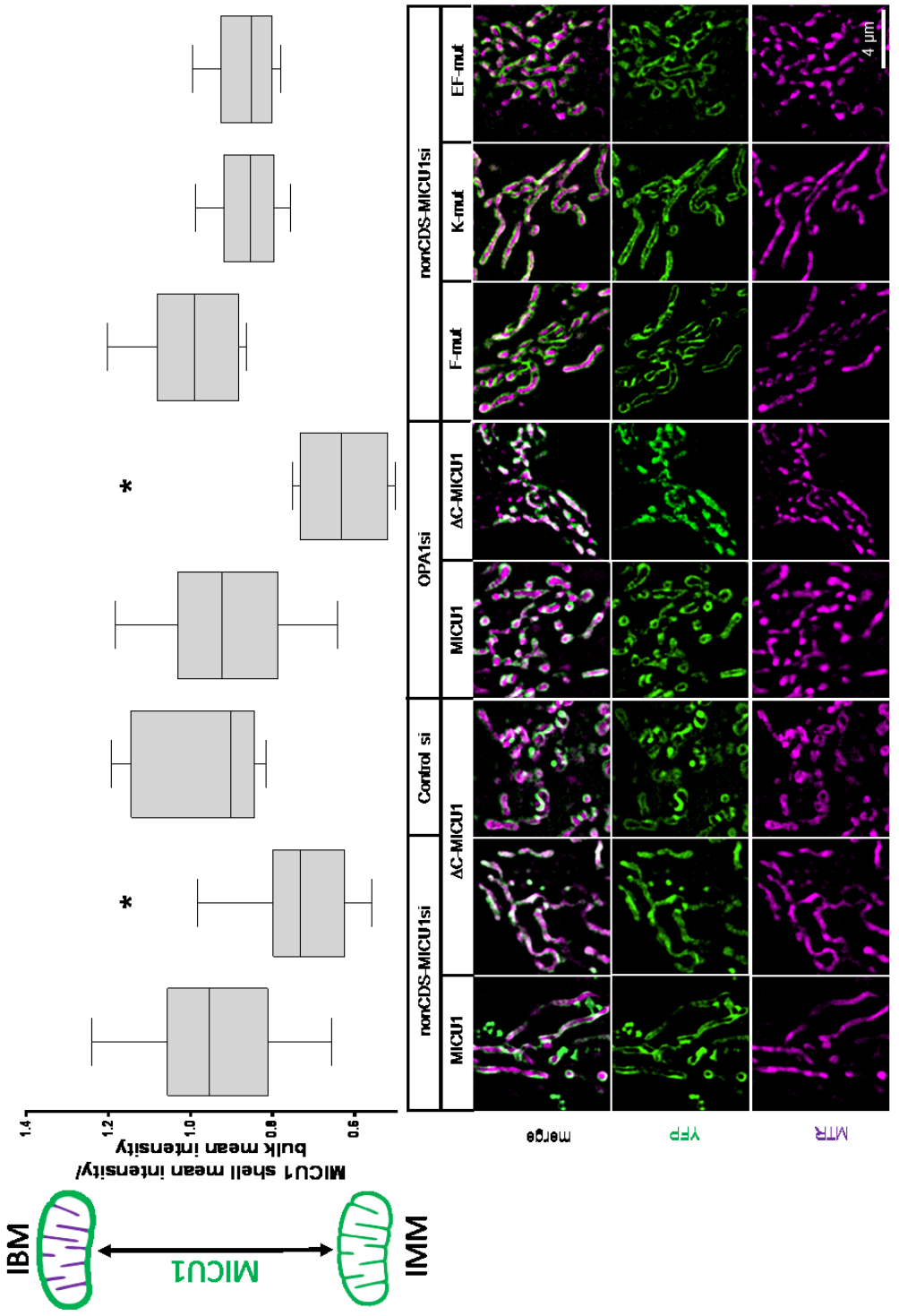

Figure 37: ***C-terminal domain of MICU1 is essential for IBM localization.*** *(Lower panel) Representative SIM images of HeLa cells stained with MTR and expressing MICU1-YFP, ΔC-MICU1-YFP, F-Mut-MICU1-YFP, K-mut-MICU1-YFP, or EF-mut-MICU1-YFP and transfected with either non-coding siRNA against MICU1 (nonCDS-MICU1si), control-siRNA (Control si), or siRNA against OPA1 (OPA1si). (Upper panel) Respective statistical analyses of the distribution of MICU1-YFP, ΔC-MICU1-YFP, F-Mut-MICU1-YFP, K-mut-MICU1-YFP, or EF-mut-MICU1-YFP after knock-down of constitutive MICU1 (nonCDS-MICU1si) or OPA1 (OPA1 si). The sub-mitochondrial distribution of MICU1-YFP, ΔC-MICU1-YFP, F-Mut-MICU1-YFP, K-mut-MICU1-YFP, or EF-mut-MICU1-YFP in the IBM and the CM was determined in these experiments (n_{MICU1}= 13; $n_{MICU1\text{-}K455F}$ = 6; $n_{MICU1\text{-}K455K}$ = 8; $n_{MICU1\text{-}\Delta EF}$ = 6, $n_{\Delta C\text{-}MICU1,control\ si}$ = 8;$n_{\Delta C\text{-}MICU1,nonCDS\ MICU1\ si}$ = 10, $n_{MICU1,\ OPA1si}$ = 16; $n_{\Delta C\text{-}MICU1,\ OPA1si}$ = 8). Bars represent mean ± SEM. *P<0.05 vs. respective control conditions carried out with analysis of variance (ANOVA) with Bonferroni post-hoc test. [96]. [Figure reproduced from Gottschalk et al., Nature Communications 2019.]*

Mitochondrial morphology was investigated for all conditions mentioned above. The expression of R455K-, R455F- and ΔEF-hand-MICU1 mutants did not influence the structure of mitochondria. Form factor, aspect ratio, minor and major diameter did not change (Figure 38) [96].

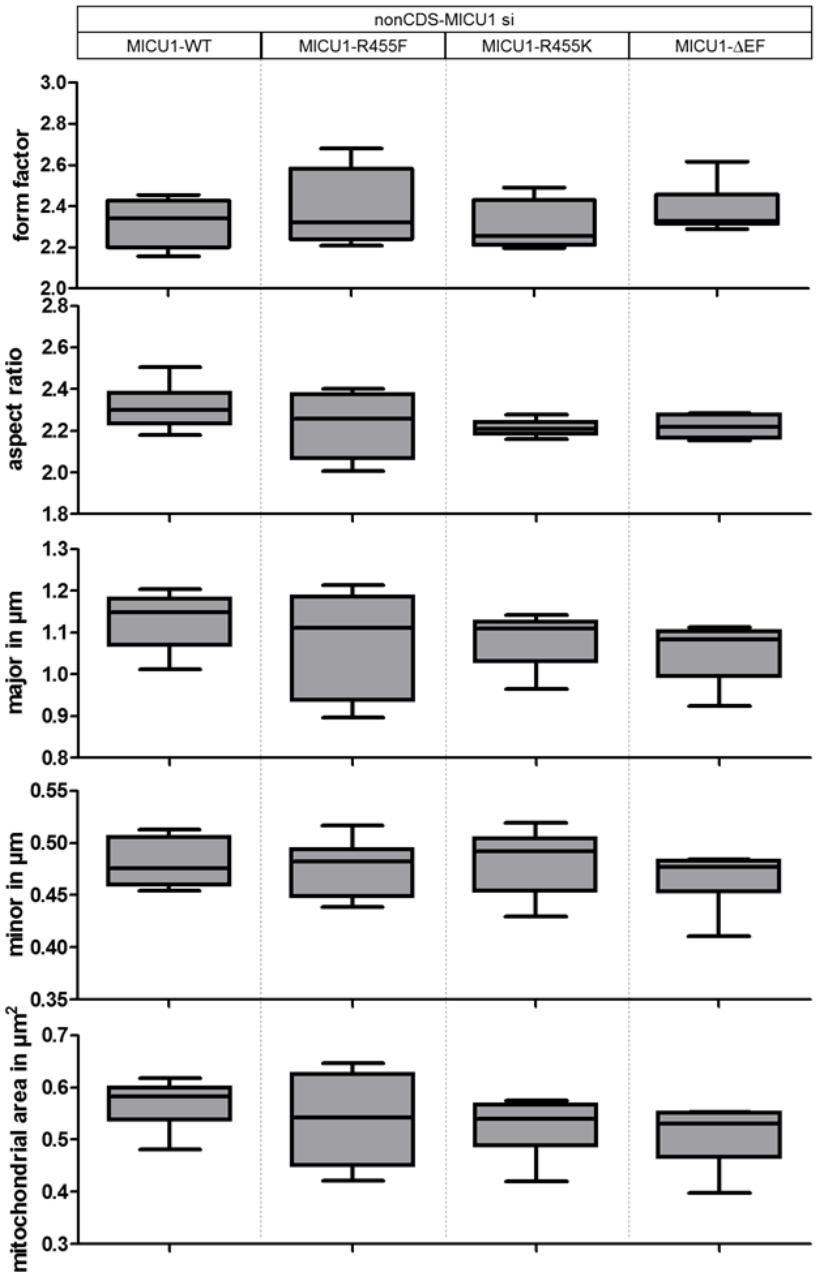

Figure 38: ***MICU1-F, MICU1-K, and MICU1-EF mutant expressing HeLa cells have the same mitochondrial morphology as wild-type MICU1-expressing cells.*** *HeLa cells were transfected with MICU1-WT or MICU1-F, MICU1-K, or MICU1-EF mutants tagged to YFP and stained for 40 min in loading buffer with 0.5 µM MTR. Form factor, aspect ratio, major, minor and mitochondrial area were determined for the MICU1 wild-type and mutants using MTR/IMM staining (n_{MICU1}= 13; $n_{MICU1\text{-}K455F}$ = 6; $n_{MICU1\text{-}K455K}$ = 8; $n_{MICU1\text{-}\Delta EF}$ = 6). *P<0.05 vs. respective control conditions carried out with analysis of variance (ANOVA) with Bonferroni post-hoc test[96]. [Figure reproduced from Gottschalk et al., Nature Communications 2019.]*

While mitochondrial morphology did not show differences between WT-MICU1 and ΔC-MICU-expressing HeLa cells under parallel knock-down of endogenous MICU1, OPA1 silencing affected the mitochondrial structure. Aspect ratio and minor diameter were increased, indicating mitochondrial fragmentation (Figure 39) [96].

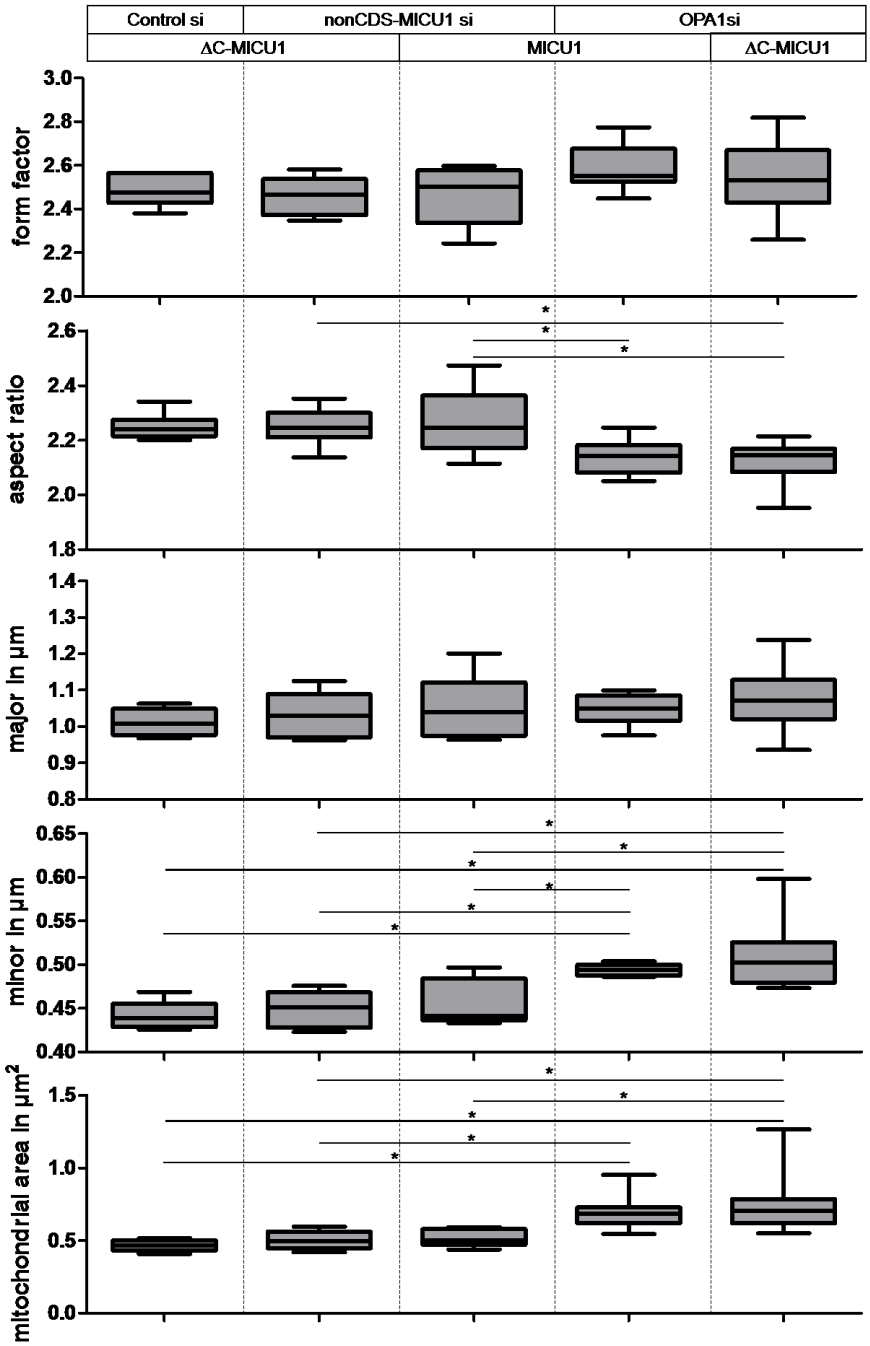

Figure 39: ***Influence of OPA1 and endogenous MICU1 silencing on mitochondrial morphology.*** *HeLa cells stained with MTR (magenta) and expressing ΔC-MICU1-YFP or MICU1-YFP and transfected with either non-coding siRNA against MICU1 (nonCDS-MICU1 si), OPA1 (OPA1 si) or Control siRNA (Control si). Form factor, aspect ratio, major, minor and mitochondrial area were determined for the MICU1 wild-type and mutants using MTR/IMM staining (n = 8). *P<0.05 vs. respective control conditions carried out with analysis of variance (ANOVA) with Bonferroni post-hoc test[96]. [Figure reproduced from Gottschalk et al., Nature Communications 2019.]*

To validate the knock-down of endogenous MICU1, but not plasmid-derived MICU1 constructs, qRT-PCR was conducted. While endogenous MICU1 shows a knock-down of 50 %, parallel transfection of HeLa cells with a MICU1-YFP construct resulted in strongly increased MICU1 mRNA levels (Figure 40) [96].

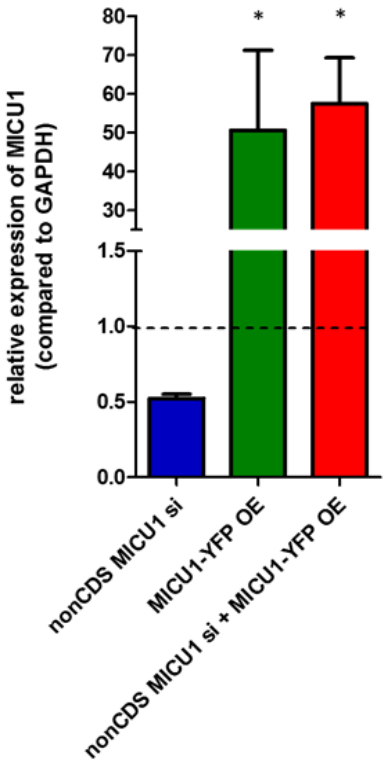

Figure 40: ***Knock-down efficiency and specificity of nonCDS MICU1si.*** *HeLa cells were transfected with MICU1-YFP (OE) and control or nonCDS MICU1 siRNA. qRT-PCR was performed to show knock-down efficiency and specificity of endogenous MICU1. Analyses were obtained from 4 different experiments on 3 independent days (n = 3). *P<0.05vs. respective control conditions carried out with analysis of variance (ANOVA) with Bonferroni post-hoc test [96]. [Figure reproduced from Gottschalk et al., Nature Communications 2019.]*

3.2.5 MICU1 and OPA1 knock-down reduce tightness of CJ

HeLa cells were first transfected with control, OPA1, or MICU1 siRNA, and subsequently fixed and prepared for electron microscopy. The electron microscopy images showed a widening of the CJ in OPA1 and MICU1 knock-down cells compared to Control siRNA (Figure 41**;** *upper panel*). An overlap of the distance from the cristae center to cristae membrane along the distance of the CJ clearly shows a tight CJ in control HeLa cells while the OPA1 and MICU1 knock-down cells have a wider CJ (Figure 41**;** *middle panel*). A direct comparison of the control,

OPA1, and MICU1 siRNA-treated cells results in a significant increase of the intermembrane distance between two opposing cristae membranes in proximity to the CJ (Figure 41; *lower panel*) [96].

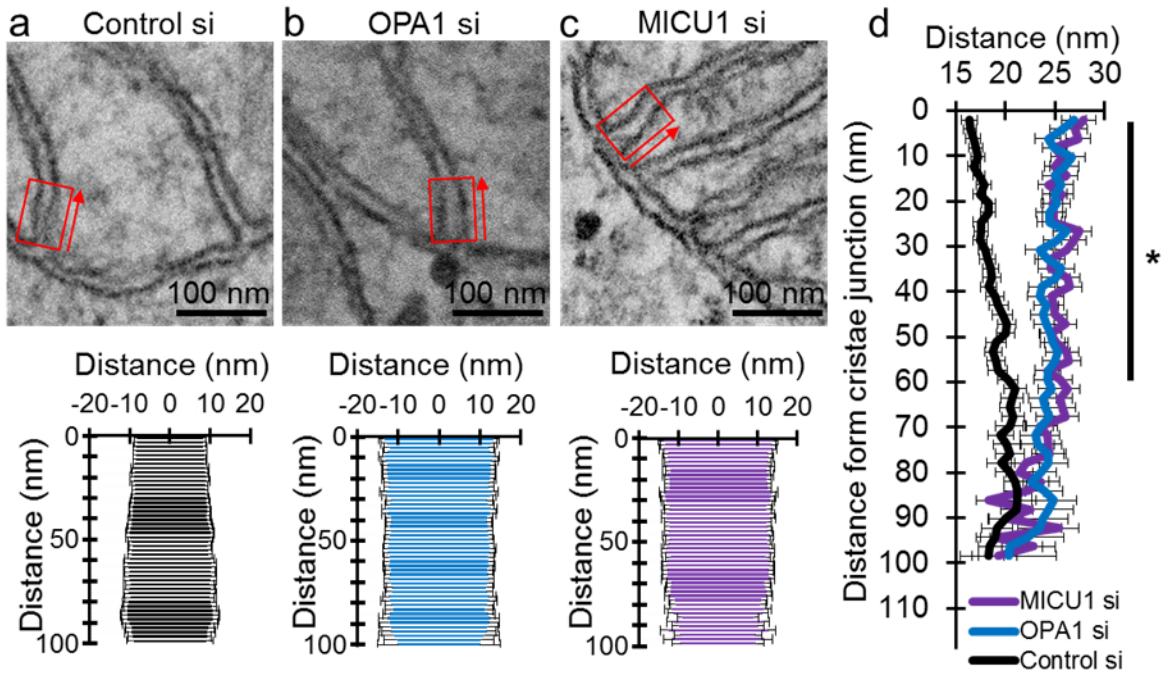

Figure 41: ***OPA1 and MICU1 tighten and stabilize the CJ.*** *(**a**) The upper panel shows a single TEM image of a mitochondrion of HeLa cells transfected with control-siRNA (Control si). To analyze the topology of the cristae junction the cristae width was measured in 2 nm increments starting at the thought prolongation of the IBM and measured into the cristae as indicated with red boxes and arrows in **a**, **b** and **c**. In the lower panel, the distance of the CM to the cristae center is plotted against the distance from the IBM (n = 115). (**b**) Same experiment as in (**a**) but with OPA1-siRNA (OPA1si) (n = 90). (**c**) Same experiment as in (**a**) but with MICU1-siRNA (MICU1si) (n = 106). (**d**) Comparative analysis of the cristae junction topology of Control, MICU1, and OPA1 siRNA-transfected cells. For TEM analysis 2 – 6 CJ were analyzed each in 10 – 12 cells of two independent preparations. *P< 0.05 vs. respective control conditions carried out with analysis of variance (ANOVA) with Bonferroni post hoc test[96]. [Figure reproduced from Gottschalk et al., Nature Communications 2019.]*

MICU1 or OPA1 knock-down do lead to an increase in the basal mitochondrial matrix Ca^{2+} concentration, which might result in mitochondrial membrane structural alterations. To exclude this possibility, electron microscopy experiments were conducted with parallel silencing of MICU1 and the MCU-complex core proteins MCU and EMRE. MCU and EMRE knock-down in HeLa cells did not influence the width of the CJ (Figure 42). Also, parallel silencing of MICU1, EMRE and MCU did not show altered CJ width compared to MICU1 knock-down (Figure 42) [96].

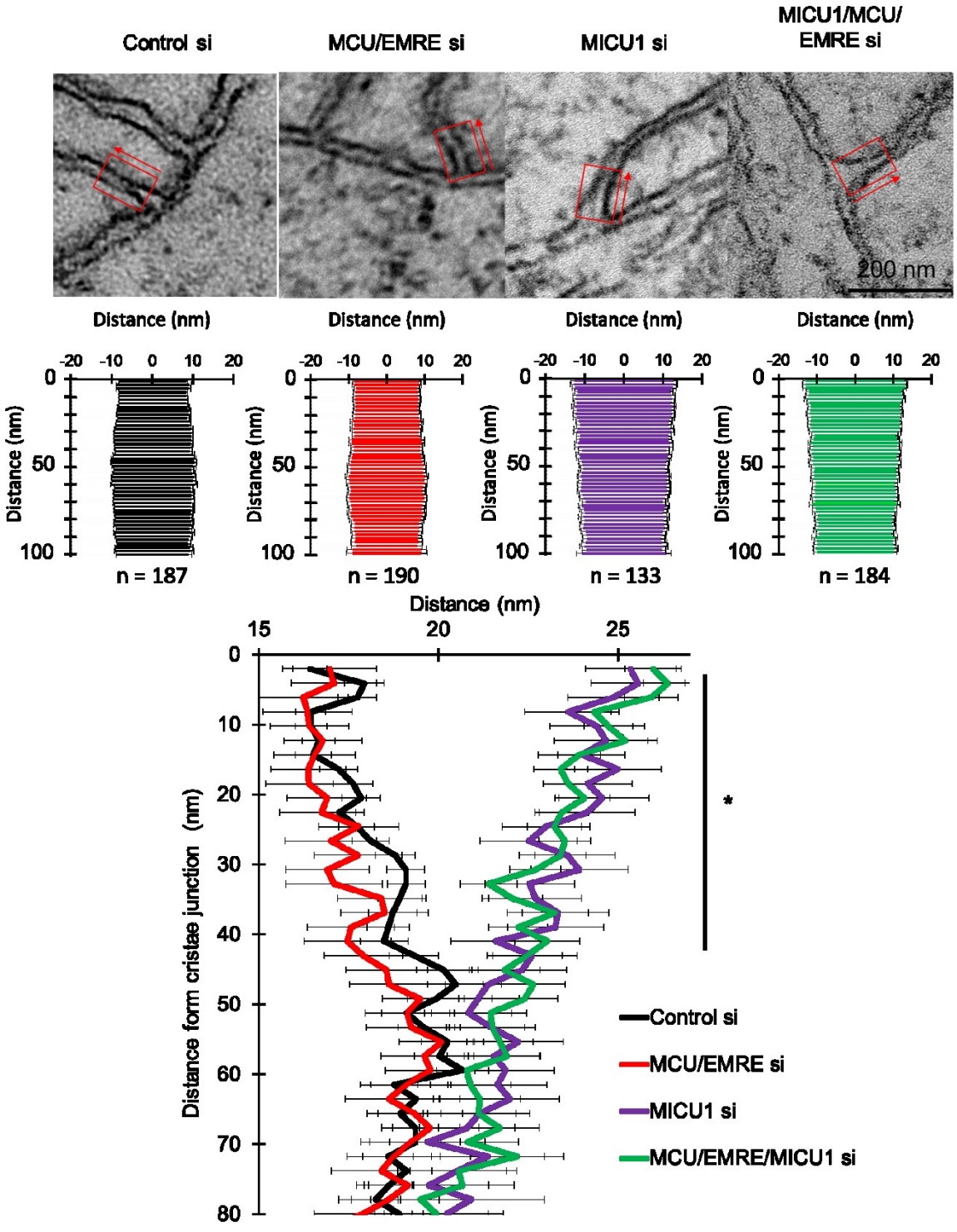

Figure 42: ***MCU/EMRE silencing is not influencing the CJ width.*** *HeLa cells transfected with Control, MICU1, MCU/EMRE or MICU1/MCU/EMRE siRNA were imaged with transmission electron microscopy. To analyze the topology of the cristae junction, the cristae width was measured in 2 nm increments starting at the thought prolongation of the IBM and measured into the cristae as indicated with red boxes and arrows in the upper panel. The comparative analysis shows no influence of MCU/EMRE silencing on the CJ width while MICU1 knock-down increases the CJ width significantly for the first 40 nm of the membrane invagination. For TEM analysis 2 – 6 CJ were analyzed each in 9 – 12 cells of 3 independent preparations ($n_{Control si}$ = 201; $n_{MCU/EMRE\ si}$ = 191; $n_{MICU1\ si}$ = 136; $n_{MCU/EMRE/MICU1\ si}$ = 184). *P<0.05 vs. respective control conditions carried out with analysis of variance (ANOVA) with Bonferroni post-hoc test[96]. [Figure reproduced from Gottschalk et al., Nature Communications 2019.]*

To evaluate the morphological changes of widened CJ in OPA1 and MICU1 knock-down cells and correlate them to mitochondrial function, mitochondrial membrane potential (Figure 43) and sub-mitochondrial localization of cytochrome C were evaluated (Figure 46). MICU1 and OPA1 knock-down significantly reduced the mitochondrial membrane potential. While MICU1-YFP overexpression could recover the phenotype, expression of ΔC-MICU1-YFP was not able to re-establish the membrane potential (Figure 43). Furthermore, the expression of ΔC-MICU1-YFP in cells expressing endogenous MICU1 did not alter the mitochondrial membrane potential (Figure 43). Next, the sub-mitochondrial distribution of cytochrome C was determined under knock-down conditions of OPA1 and MICU1. HeLa cells were stained with MTRCMX, fixed and immunolabeled for cytochrome C (Figure 46) [96].

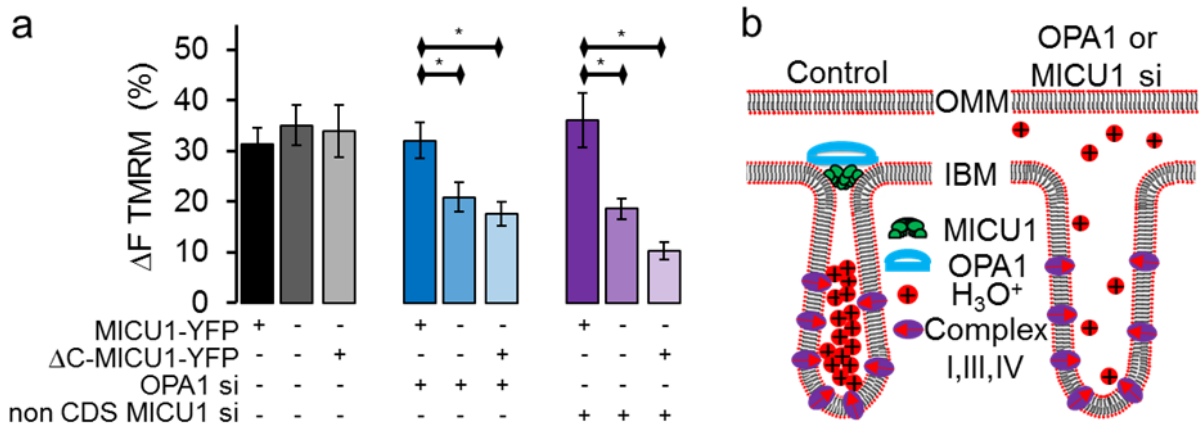

Figure 43: ***Knock-down of OPA1 and MICU1 decreases membrane potential.*** *(**a**) HeLa cells overexpressing MICU1-YFP or ΔC-MICU1-YFP were transfected with Control, OPA1, or MICU1 siRNA. The TMRM Δ fluorescence intensity after addition of 2 µM FCCP was measured ($n_{MICU1\text{-}YFP;Control\ si}$ = 8; $n_{no\text{-}FP;\ Control\ si}$ = 8; $n_{\Delta C\text{-}MICU1\text{-}YFP;\ Control\ si}$ = 8; $n_{MICU1\text{-}YFP;\ OPA1\ si}$ = 9; $n_{no\text{-}FP;\ OPA1\ si}$ = 9; $n_{\Delta C\text{-}MICU1\text{-}YFP;\ OPA1\ si}$ = 9; $n_{MICU1\text{-}YFP;\ nonCDS\ MICU1\ si}$ = 8; $n_{no\text{-}FP;\ nonCDS\ MICU1\ si}$ = 8; $n_{\Delta C\text{-}MICU1\text{-}YFP;\ nonCDS\ MICU1\ si}$ = 9). (**b**) Schematic representation of the impact of MICU1 or OPA1 depletion on the mitochondrial membrane potential caused by enlarged cristae junction. *P< 0.05 vs. respective control conditions carried out with analysis of variance (ANOVA) with Bonferroni post hoc test[96]. [Figure reproduced from Gottschalk et al., Nature Communications 2019.]*

In order to check if knock-down or knockout of MCU or EMRE, respectively, might have an influence on the membrane potential similar to MICU1 and OPA1, TMRM experiments were carried out. Neither MCU-silenced cells nor EMRE knockout cells showed any variation of the mitochondrial membrane potential compared to control cells (Figure 44) [96].

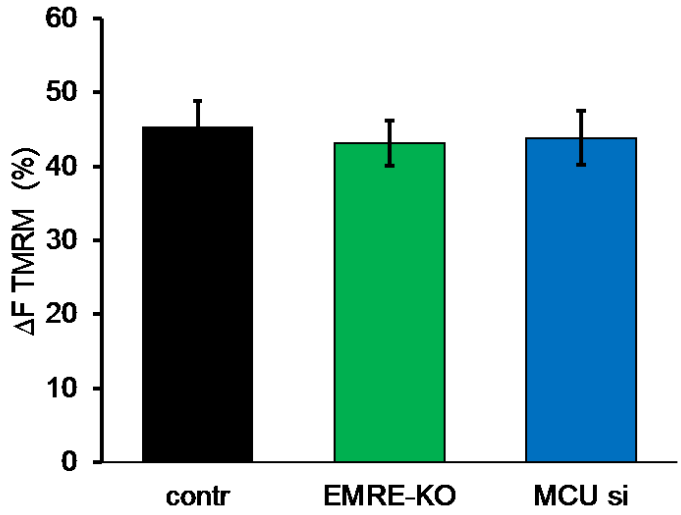

Figure 44: ***Silencing of MCU or knockout of EMRE does not affect mitochondrial membrane potential.*** *HeLa cell transfected with control or MCU siRNA and HeLa-EMRE-KO cells were stained with TMRM. The TMRM Δ fluorescence intensity after addition of 2 µM FCCP was measured (n = 9). *P<0.05 vs. respective control conditions calculated with analysis of variance (ANOVA) with Bonferroni post-hoc test[96]. [Figure reproduced from Gottschalk et al., Nature Communications 2019.]*

The cristae junction separates the cristae lumen from the IBM. Therefore, it was investigated whether a widening of the CJ has a direct influence on sub-mitochondrial calcium homeostasis. Cells transfected with Control siRNA, MICU1 siRNA or OPA1 siRNA and either the IBM sensor IMS-GEMGeCO1 or CL-sensor CL-GEMGeCO1 were imaged under resting conditions and challenged with histamine to provoke ER Ca^{2+} release. Basal CL Ca^{2+} concentrations increased under OPA1 and MICU1 knock-down conditions, while IMS Ca^{2+} levels remained unchanged (Figure 45). Histamine challenging resulted in a strong Ca^{2+} increase for both CL and IMS, regardless of MICU1 or OPA1 silencing (Figure 45) [96].

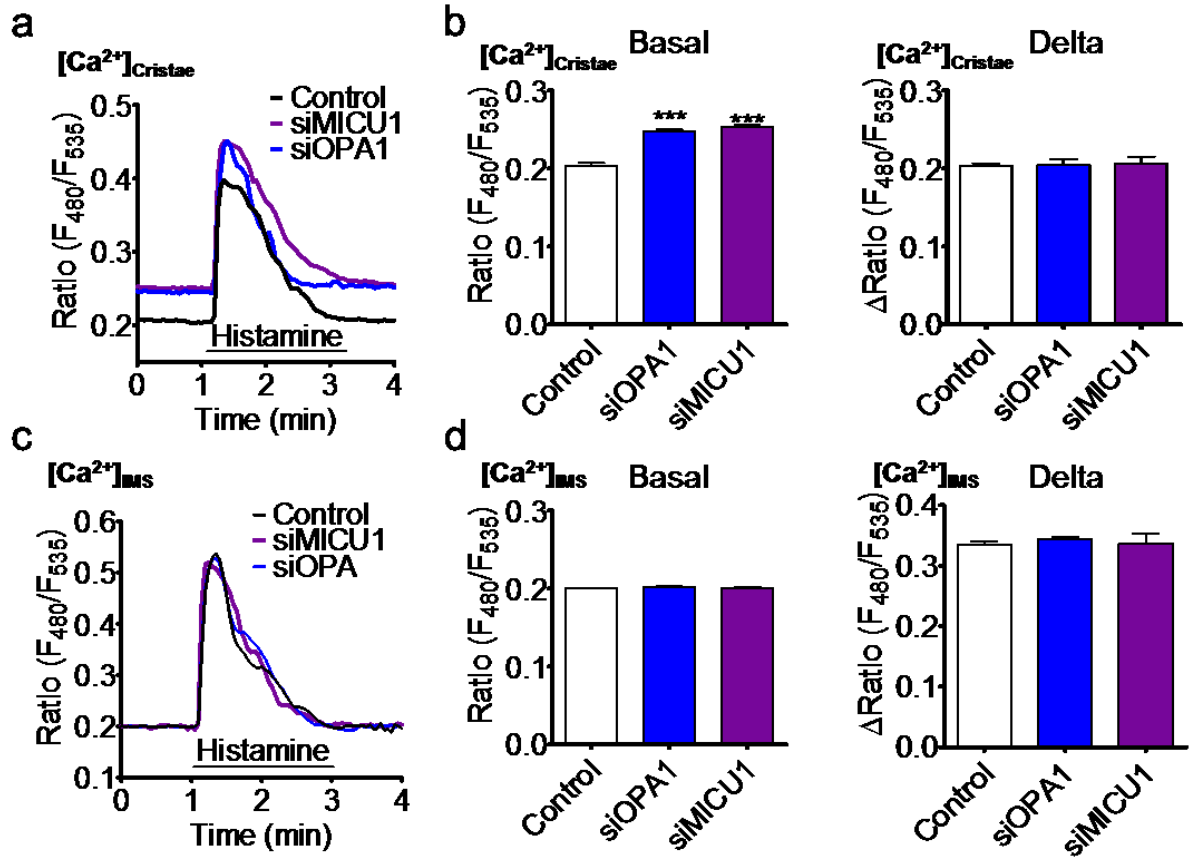

Figure 45: ***Silencing of OPA1 or MICU1 increases basal Ca^{2+} concentration in mitochondrial cristae lumen.*** *(a, b) HeLa cells were transfected with the cristae Ca^{2+} sensor CL-GEMGeCO1 and Control, OPA1, or MICU1 siRNA. Cells were challenged with 100 µM histamine to induce ER Ca^{2+} release ($n_{Control\ si}$ = 9; $n_{OPA1\ si}$ = 10; $n_{MICU1\ si}$ = 10). (c, d) HeLa cells were transfected with the IMS Ca^{2+} sensor IMS-GEMGeCO1 and control, OPA1, or MICU1 siRNA. Cells were challenged with 100µM histamine to induce ER Ca^{2+} release ($n_{Control\ si}$ = 8; $n_{OPA1\ si}$ = 11; $n_{MICU1\ si}$ = 7). *= P<0.05vs. respective control conditions carried out with analysis of variance (ANOVA) with Bonferroni post-hoc test[96]. [Figure reproduced from Gottschalk et al., Nature Communications 2019.]*

For OPA1 and MICU1 knock-down mitochondria, a clear shift of cytochrome C from cristae localization towards the intermembrane space was observed (Figure 46). Including the observation of a widened CJ under MICU1 and OPA1 knock-down, it can be assumed that the open cristae is leading to a disruption of the proton gradient present in the cristae under control conditions, which in turn reduces the mitochondrial membrane potential (Figure 42 **&** Figure 43). The same morphological change in CJ structure might lead to a redistribution of cytochrome C from the CM to the whole IMM (Figure 46) [96].

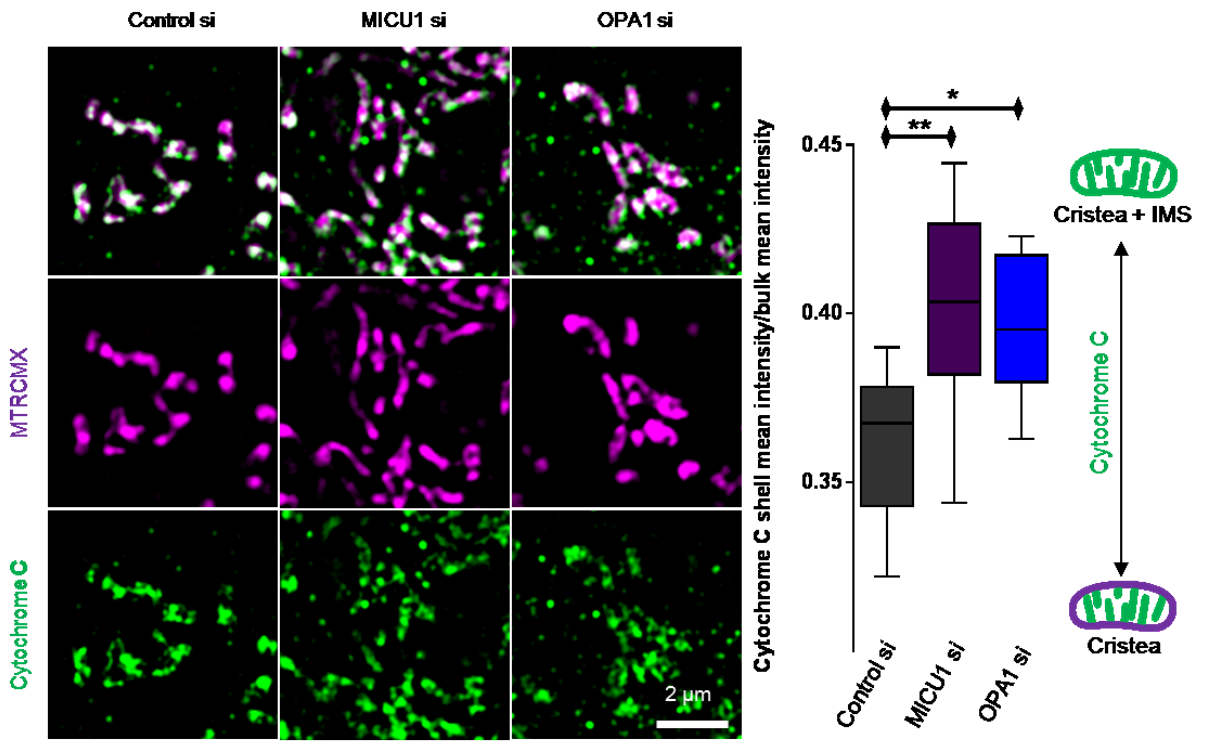

Figure 46: ***Knock-down of MICU1 and OPA1 lead to cytochrome C delocalization.*** *(Right panel) Representative images of HeLa cells transfected with control, OPA1, or MICU1 siRNA, stained with MTRCMX, fixed and immunostained for cytochrome C. (left panel) Quantitative analysis of the sub-mitochondrial distribution of cytochrome C in HeLa cells transfected with control, OPA1, or MICU1 siRNA (n = 12). *P< 0.05 vs. respective control conditions carried out with analysis of variance (ANOVA) with Bonferroni post hoc test[96]. [Figure reproduced from Gottschalk et al., Nature Communications 2019.]*

Release of cytochrome C from the CM into the cytosol leads to caspase activation and apoptosis. In the case of MICU1 and OPA1 knock-down, only a redistribution within the mitochondria was observed. Cell viability and caspase activation assays were performed. Neither decreased viability nor increased caspase activity were measured, validating that cytochrome C only reorganizes within the mitochondria while MICU1 or OPA1 are silenced, but is not released to the cytosol to induce apoptosis (Figure 47) [96].

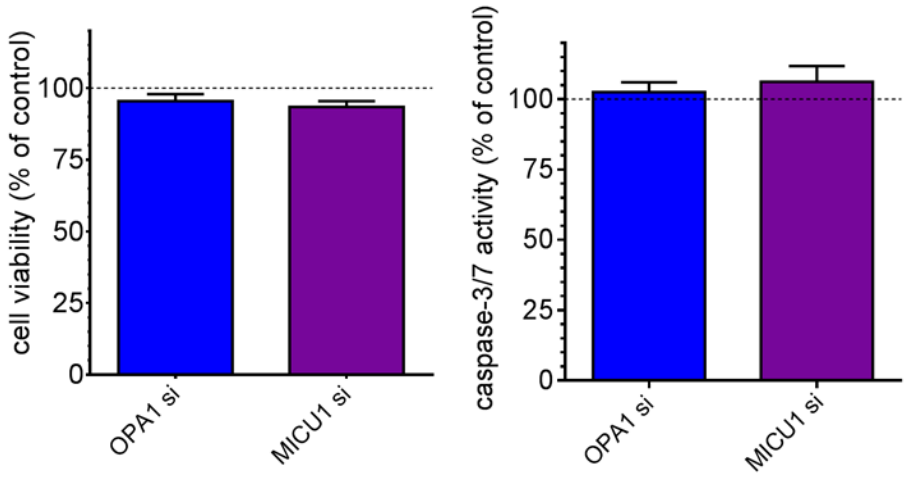

Figure 47: ***Knock-down of OPA1 or MICU1 in HeLa cells does not change the cell viability or caspase-3/7 activity.*** *HeLa cells were transfected with control, MICU1, or OPA1 siRNA. Cell viability and apoptotic levels were measured with CellTiter-Blue® assay (Promega) and Caspase-Glo®-3/7 assay (Promega), respectively. No significant changes in cell viability or caspase activity could be determined. Analyses were obtained from 5 different experiments on 2 independent days (n = 5). * =P<0.05vs. respective control conditions calculated with unpaired double sided T-Test[96]. [Figure reproduced from Gottschalk et al., Nature Communications 2019.]*

3.3 MICU1 acts as a Ca^{2+}-dependent diffusion trap for the MCU-complex

The third part of the results section is based on my first author publication (Gottschalk et al. 2019). MICU1 is the so-called gatekeeper of the mitochondrial Ca^{2+} uniporter[19]. In order to correlate the function of MICU1 with its sub-mitochondrial localization, the MCU-complex core proteins (MCU, EMRE) were investigated with regard to their localization, especially during ER Ca^{2+} signaling. Furthermore, the contribution of UCP2 and PRMT1 on fine-tuning MICU1 function, and the correlation to MCU localization during ER-Ca^{2+} release were investigated.

3.3.1 MCU shuttles from the CM towards the IBM under ER Ca^{2+} release

The discovery of MICU1[10] was followed by the identification of MCU[5,6] which co-immunoprecipitates with it[6]. Next, it was determined whether the restriction of MICU1 to the IBM is likewise a characteristic of MCU, by co-expressing MCU-mCherry together with MICU1-YFP to establish their sub-mitochondrial distributions. It was found that, in contrast to MICU1, MCU is uniformly distributed throughout the IMM in resting cells (Figure 48) [96].

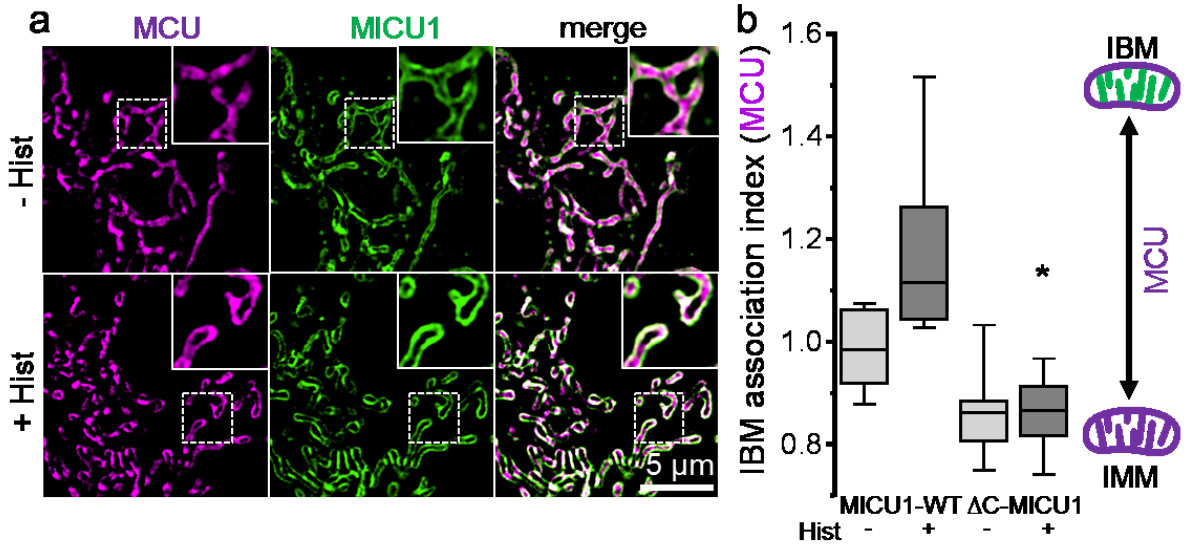

Figure 48: ***MCU shuttles Ca^{2+} and MICU1 dependent to the IBM.*** *(a) HeLa cells were transiently transfected with MCU-mCherry and MICU1-YFP and imaged with SIM under resting conditions (- Hist) and 90 s after stimulation with histamine (100 µM) (+ Hist). Shown are representative SIM captures showing the distribution of MCU-mCherry (magenta) and MICU1-YFP (green). Dotted squares indicate areas shown at high magnification in the upper left corner. (b) Statistical analysis of the sub-mitochondrial MCU-mCherry distribution in MICU1- or ΔC-MICU1-YFP-expressing cells represented as relative distribution of MCU in the IBM vs. CM area (n = 8). *P< 0.05 vs. respective control conditions carried out with unpaired double-sided T-test[96]. [Figure reproduced from Gottschalk et al., Nature Communications 2019.]*

However, after stimulation with histamine, MCU joins MICU1 to exclusively localize in the IBM. Ca^{2+}-induced redistributions of MCU were not observed in cells exclusively expressing the ΔC-mutant of MICU1, which is unable to bind to MCU[97] (Figure 48). These data indicate that, upon elevation of IMS Ca^{2+} concentrations, the active MCU-complex dynamically assembles because MICU1 traps MCU in the IBM. This potential mechanism is further supported by the dependence of mitochondrial Ca^{2+} signals and MCU sub-mitochondrial distribution, which establish a strict correlation between MCU translocations and mitochondrial Ca^{2+} elevation in response to histamine (Figure 49) [96].

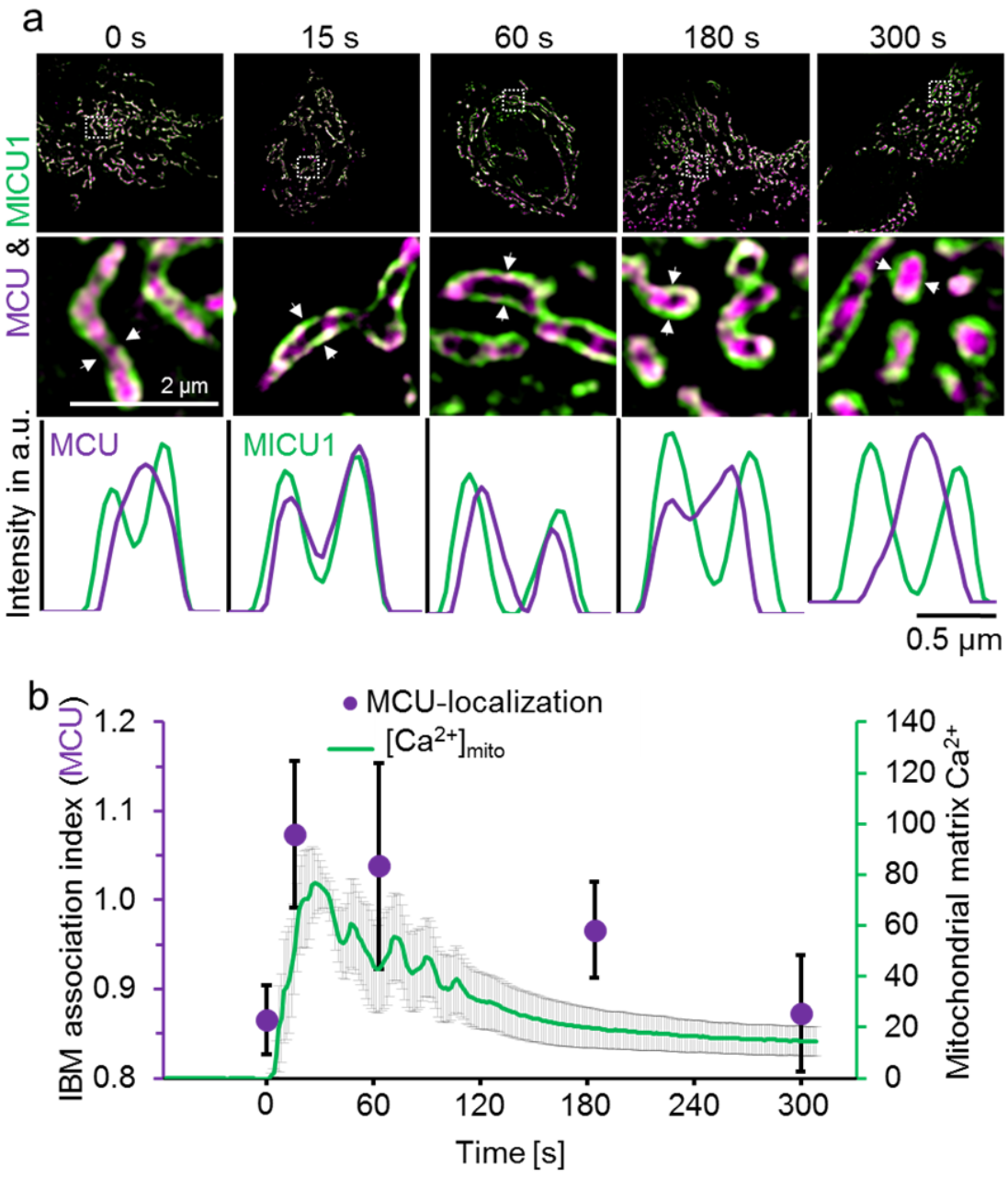

Figure 49: ***Strong correlation between MCU-shuttling and mitochondrial matrix Ca^{2+} concentration.*** *(a) Representative images (top & middle) and line plots (bottom) of MCU-mCherry (magenta) and MICU1-YFP (green) under resting conditions (0 s) and 15, 60, 180 and 300 s after stimulation with histamine (100 µM) in nominally Ca^{2+}-free buffer. (b) Time correlation between the accumulation of MCU in the IBM (magenta points) and mitochondrial Ca^{2+} concentration (green line and gray SD error bars) upon stimulation with 100 µM histamine (n = 9). These cells were transiently transfected with mito-R-GECO1 to measure mitochondrial matrix Ca^{2+} concentrations (n = 8) (green line)[96]. [Figure reproduced from Gottschalk et al., Nature Communications 2019.]*

Besides HeLa cells, other non-excitable cell lines were also investigated to determine whether the MCU shuttling process could be observed with ER Ca^{2+} release. The redistribution of MCU to the IBM after ER Ca^{2+} release was confirmed in HEK, A549, and MCF-7 cells (Figure 50) [96].

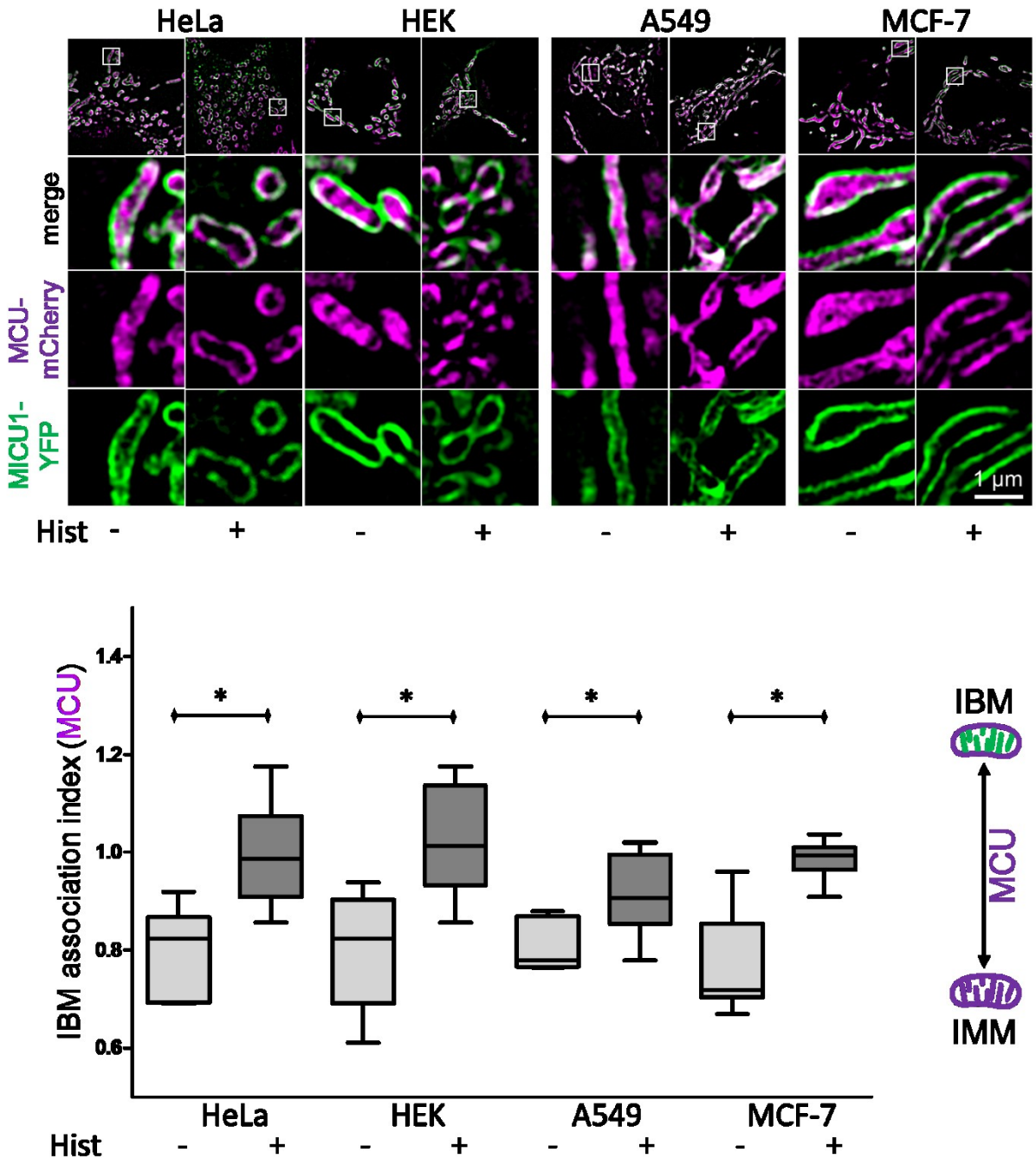

Figure 50: ***MCU-shuttling in non-excitable HeLa, HEK, A549, and MCF-7 cells.*** *Representative images and IBM association factor of HeLa, HEK, A549, or MCF-7 cells transfected with MCU-mCherry and MICU1-YFP treated with and without histamine. Images and analyses were obtained from at least 10 cells in each of 2 different experiments on 4 independent days (n = 8). * = P<0.05 vs. respective control conditions calculated with unpaired double sided T-Test[96]. [Figure reproduced from Gottschalk et al., Nature Communications 2019.]*

Other than the MCU-shuttling process, the mitochondrial morphology of HeLa, HEK, A549, and MCF-7 cells was also compared, with and without the addition of histamine to induce ER Ca^{2+} release. HeLa, HEK and A549 cells showed slight signs of mitochondrial fragmentation expressed as altered form factor or aspect ratio (Figure 51). MCF-7 cells did not undergo

mitochondrial fission, but rather tended to swell, indicated by increasing mitochondrial area as well as minor and major diameter (Figure 51) [96].

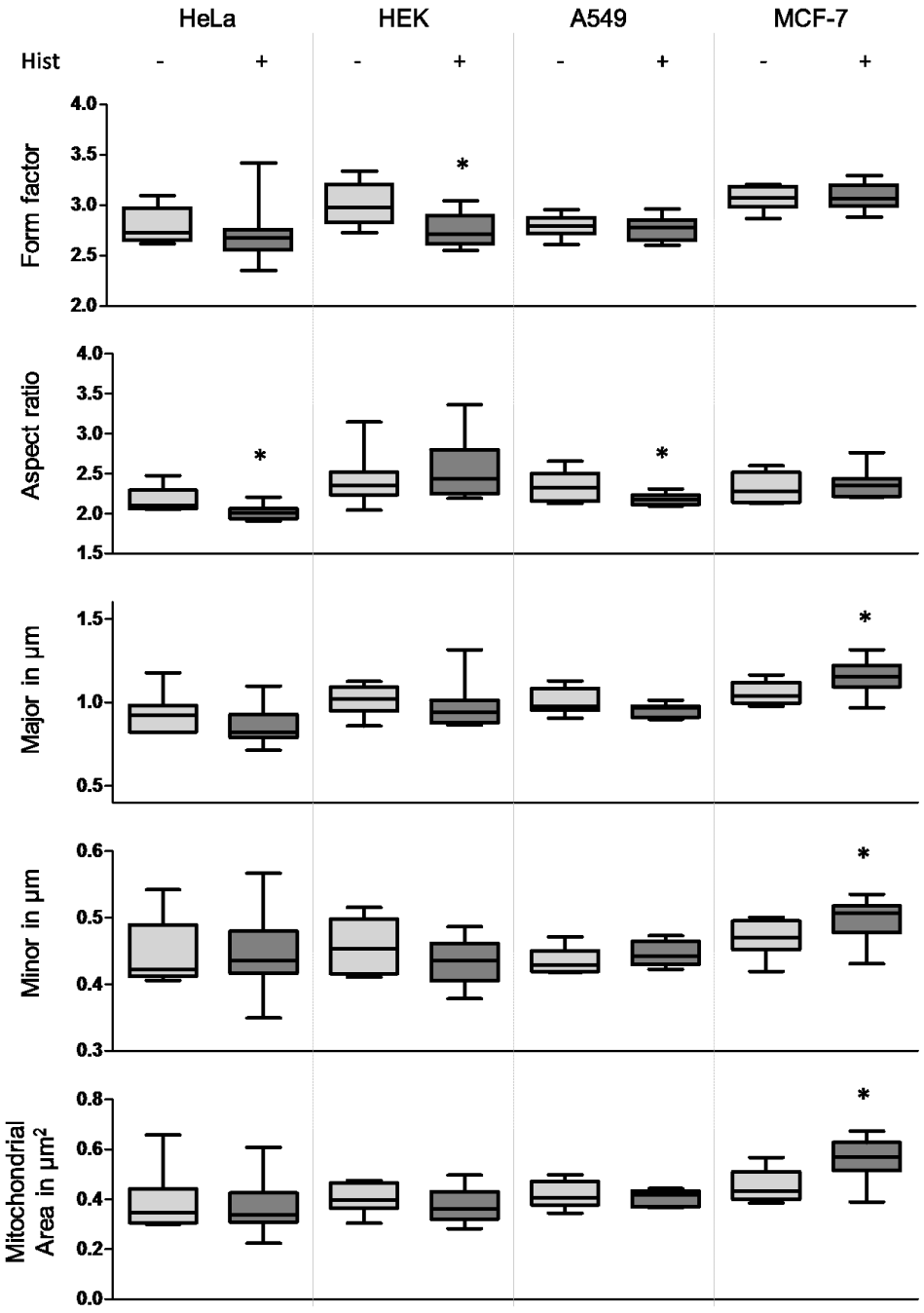

Figure 51: ***Mitochondrial morphology in non-excitable HeLa, HEK, A549, and MCF-7 cells.*** *HeLa, HEK, A549, or MCF-7 cells were transfected with MCU-mCherry and MICU1-YFP and treated with and without histamine. The MICU1-YFP channel was used to analyze mitochondrial form factor, aspect ratio, major/minor diameters as well as the mitochondrial area. Analyses were obtained from at least 10 cells in each of 2 different experiments on 4 independent days (n = 8). * = P<0.05 vs. respective control conditions carried out with analysis of variance (ANOVA) with Bonferroni post-hoc test[96]. [Figure reproduced from Gottschalk et al., Nature Communications 2019.]*

Our results additionally revealed that the redistribution of MCU is independent of extracellular Ca^{2+} by testing the MCU shuttling effect with 2Ca- and 0Ca-buffer (Figure 52). In both cases, a clear shift of MCU into the IBM was observed [96].

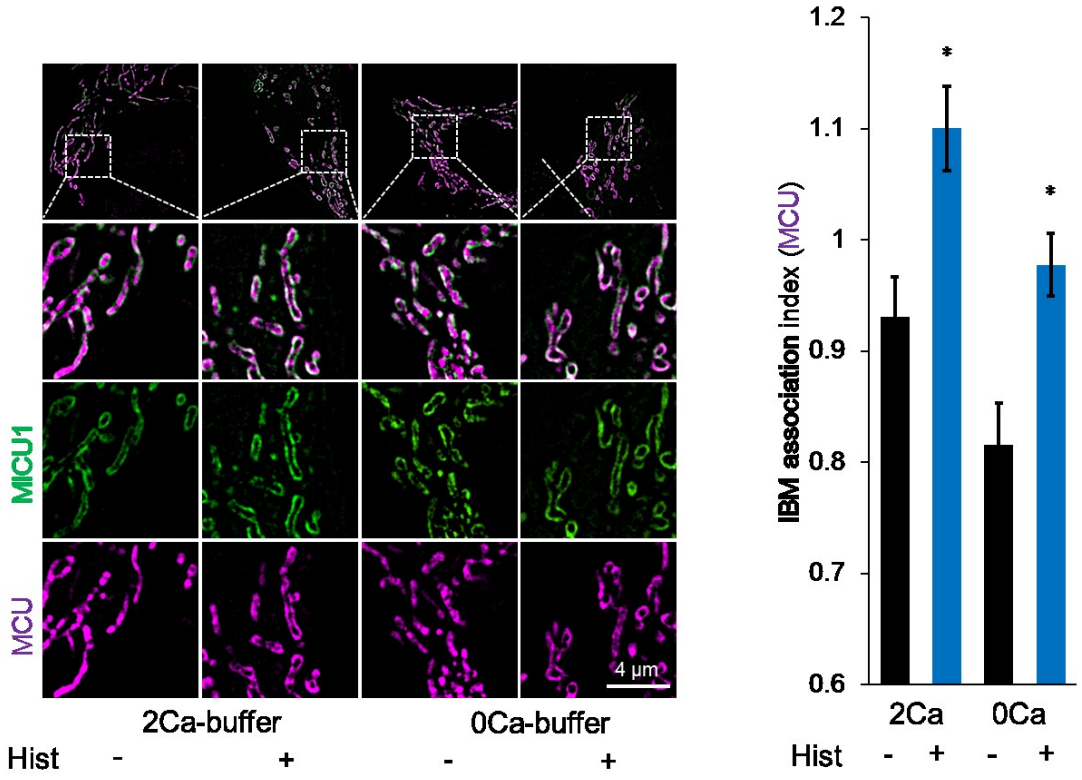

Figure 52: ***MCU shuttling is independent of extracellular Ca^{2+}.*** *HeLa cells transfected with MICU1-YFP and MCU-mCherry imaged with and without the presence of histamine in 2Ca or 0Ca buffer. Images and analyses were obtained from at least 10 cells in 2 different experiments on 4 independent days (n = 8). *P<0.05 vs. respective control conditions calculated with unpaired double sided T-Test[96]. [Figure reproduced from Gottschalk et al., Nature Communications 2019.]*

Overexpression of MCU-mCherry with and without the non-labeled MICU1 in HeLa cells labeled with MTG showed a clear dependency of MCU shuttling upon MICU1 expression (Figure 53). These findings together indicate that cytosolic Ca^{2+} triggers anchoring of MCU to MICU1 in the IBM [96].

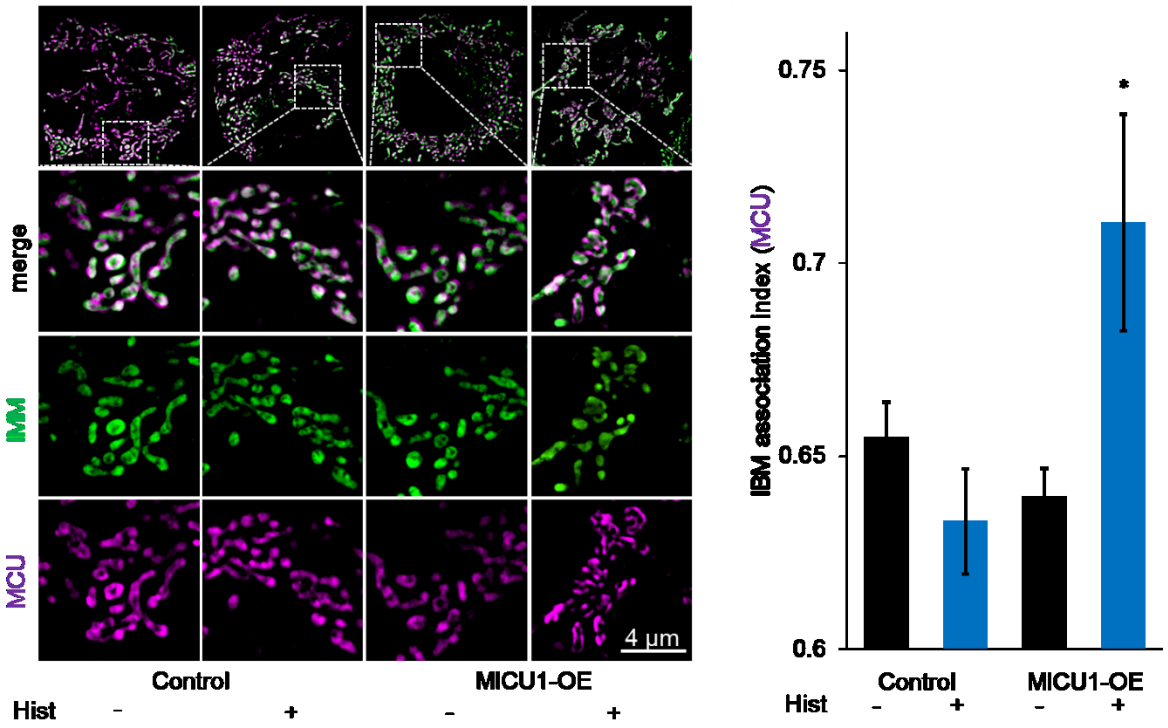

Figure 53: ***MCU IBM recruitment is dependent on MICU1.*** *Representative images of HeLa cells transfected with MCU-mCherry, stained with MTG and transfected with or without MICU1-OE vector imaged with and without the presence of histamine. Images and analyses were obtained from at least 10 cells in 2 different experiments on 4 independent days (n = 8). *P<0.05 vs. respective control conditions calculated with unpaired double sided T-Test[96]. [Figure reproduced from Gottschalk et al., Nature Communications 2019.]*

Notably, MICU1-YFP expression did not change the arrangement of the IMM-marker Mitotracker RedFM© (MTR) in either resting or stimulated cells, indicating that the integrity of the IMM was maintained throughout our experimental conditions (Figure 54) [96].

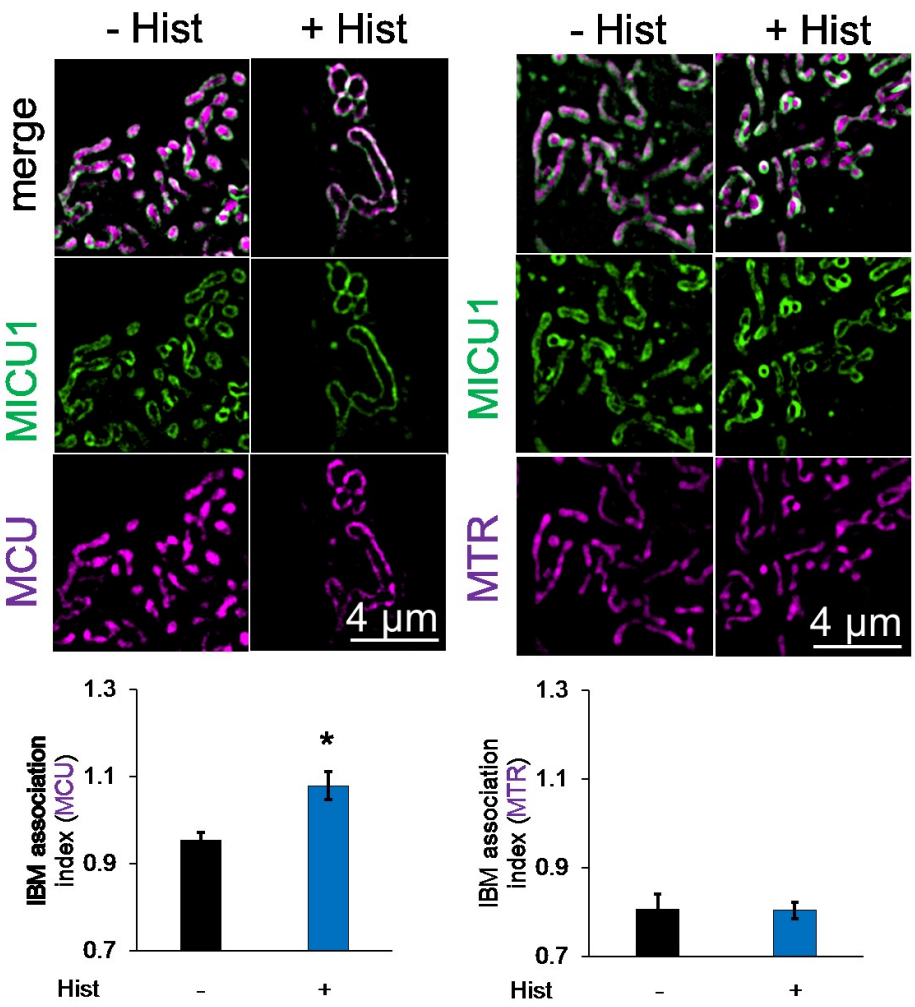

Figure 54: ***The integrity of the IMM is not disrupted by MICU1-YFP expression in either resting or histamine-stimulated cells.*** *Representative images of HeLa cells transfected with MICU1-YFP and MCU-mCherry or stained with MTR and imaged with and without the presence of histamine. Sub-mitochondrial localization was determined. Images and analyses were obtained from at least 10 cells in 2 different experiments on 4 independent days (n = 8). *P<0.05 vs. respective control conditions calculated with unpaired double sided T-Test[96]. [Figure reproduced from Gottschalk et al., Nature Communications 2019.]*

3.3.2 EMRE shuttling is MICU1 and MCU dependent

Next, the distribution of the second pore-forming protein of the MCU-complex, EMRE, was mapped to further characterize the dynamics of MCU-complex assembly during cell stimulation. Like our approach with MCU, an EMRE-mCherry construct was co-expressed with MICU1-YFP. Under basal conditions, EMRE was distributed throughout the entire IMM; this distribution did not change upon stimulation with histamine (Figure 55) [96].

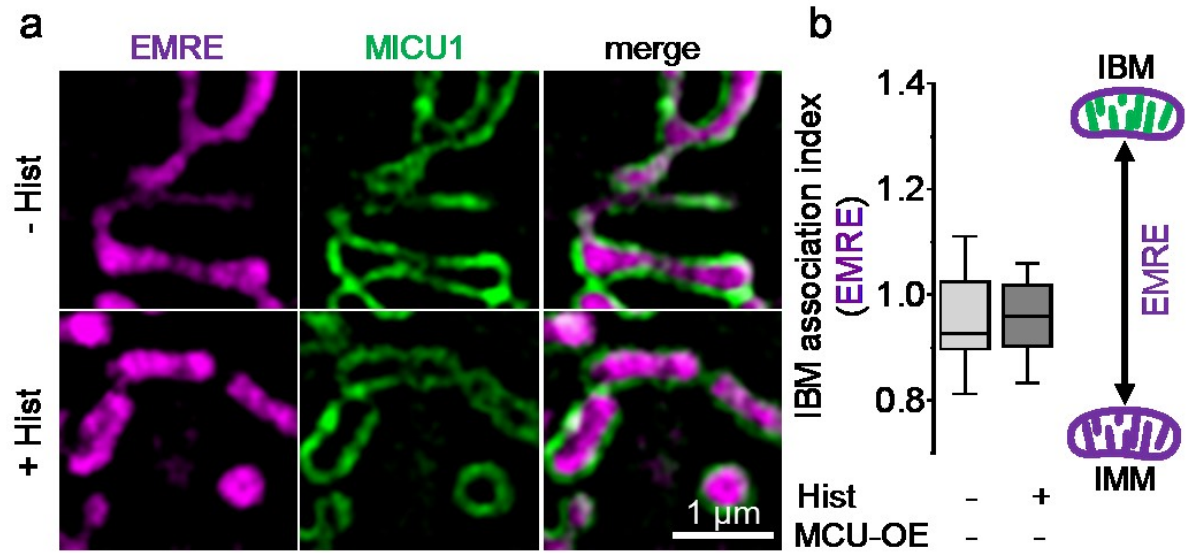

Figure 55: ***EMRE re-distributes to the IBM under ER Ca^{2+} release conditions.*** *(a) Representative SIM images of HeLa cells that were transiently transfected with EMRE-mCherry (magenta) and MICU1-YFP (green) under resting conditions and 90 s after stimulation with 100 µM histamine. (b) Sub-mitochondrial localization of EMRE-mCherry under resting conditions (-Hist) and 90 s after treatment with histamine (100 µM) (+Hist) was determined by the IBM association index (n = 8). *P< 0.05 vs. respective control conditions carried out with unpaired double-sided T-test[96]. [Figure reproduced from Gottschalk et al., Nature Communications 2019.]*

This finding is unexpected because EMRE strongly binds to MCU[7]. However, because EMRE-MCU stoichiometry could contribute to this result, experiments were pursued involving the co-expression of MCU, MICU1-YFP, and EMRE-mCherry. Under these conditions of increased MCU levels, EMRE now accumulated in the IBM upon Ca^{2+} mobilization (Figure 56) [96].

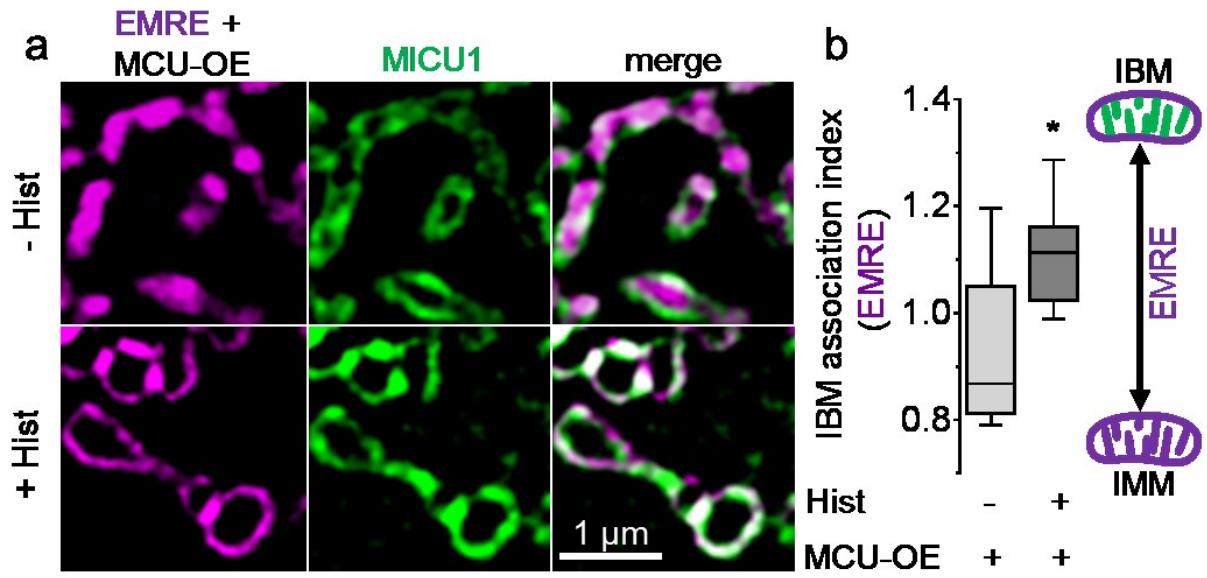

Figure 56: ***EMRE re-distribute in an MCU-dependent manner to the IBM under ER Ca^{2+} release conditions.*** *(a) Identical experiments as those in Figure 55 but using cells that overexpressed wild-type MCU. (b) Identical experiments as those in Figure 55 but using cells that overexpressed wild-type MCU. Images and analyses were obtained from at least 10 cells in each of the 8 experiments (n = 8). *P< 0.05 vs. respective control conditions carried out with unpaired double-sided T-test[96]. [Figure reproduced from Gottschalk et al., Nature Communications 2019.]*

To validate the functional activity of the EMRE-mCherry construct, recovery experiments in EMRE knockout HeLa cells were conducted. While EMRE knockout cells showed drastically decreased basal Ca^{2+} levels and Ca^{2+} uptake after challenging the cells with histamine, EMRE-mCherry expression could fully recover mitochondrial Ca^{2+} uptake to a level equal to control cells (Figure 57). EMRE-mCherry expression in control HeLa cells resulted in increased Ca^{2+} basal and delta uptake levels (Figure 57). Further co-immunoprecipitation experiments were conducted with MICU1-Flag, EMRE-mCherry-His, and MCU-mCherry-His constructs. MICU1-Flag binds to EMRE-mCherry-His as well as to MCU-mCherry-His validating that the mCherry-tag is not influencing the binding capabilities of EMRE and MICU1 (Figure 57) [96].

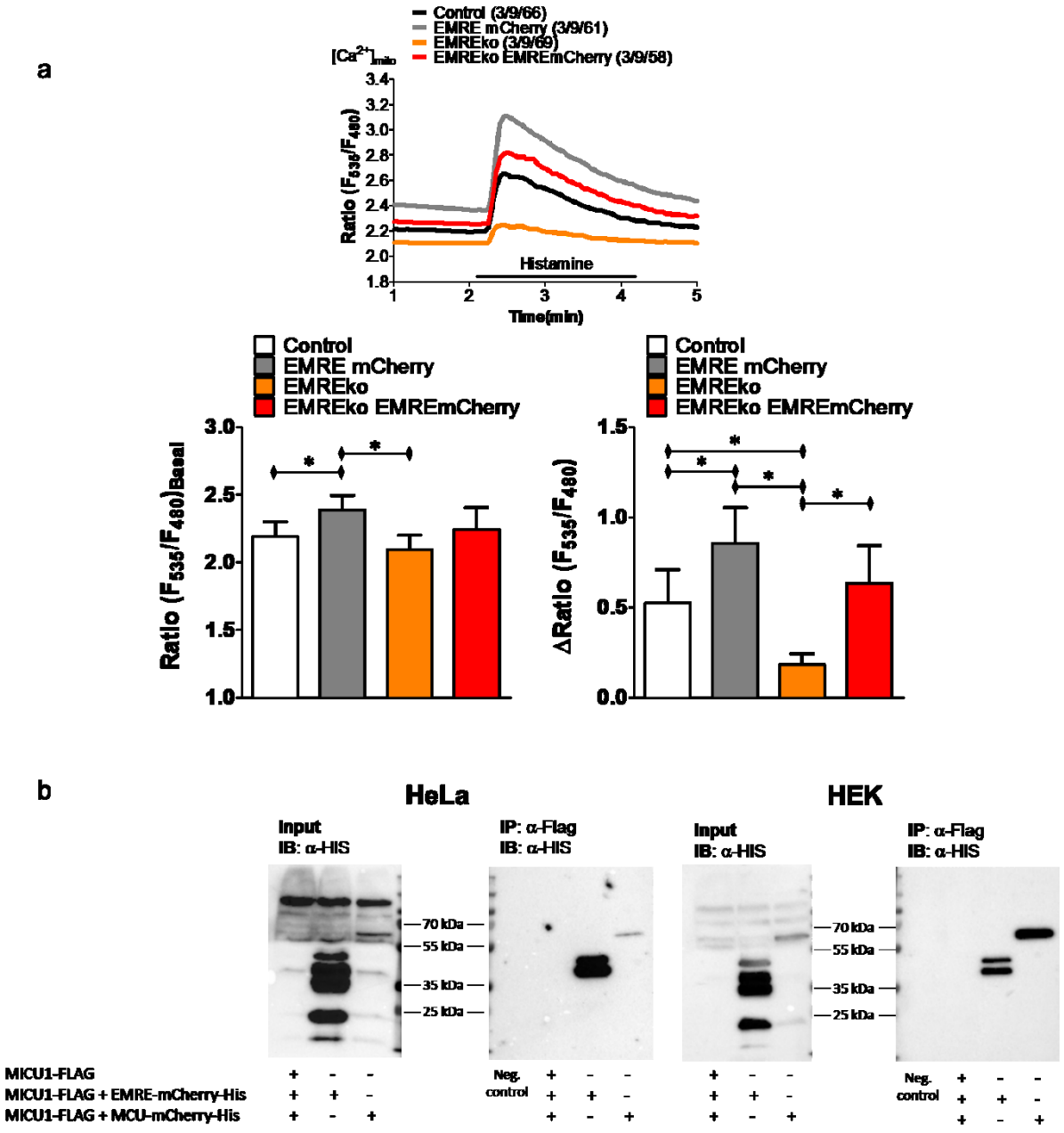

Figure 57: ***EMRE-mCherry is functionally active and binds to MICU1.*** *(a) HeLa cells and HeLa-EMRE-KO cells were transfected with the mitochondrial matrix Ca^{2+} sensor 4mt3cpv and with or without EMRE-mCherry. The basal and maximal delta Ca^{2+} signals induced by histamine were analyzed. Analyses were obtained from 3 different experiments on 3 independent days (n = 9). (b) HeLa or HEK cells were transfected with MICU1-FLAG alone or in combination with MCU-mCherry-His or EMRE-mCherry-His. MICU1 was immunoprecipitated using the FLAG-tag from whole cell lysate and the co-precipitated proteins were immunoblotted with a His-antibody (n = 3). *P< 0.05 vs. respective control conditions carried out with unpaired double-sided T-test[96]. [Figure reproduced from Gottschalk et al., Nature Communications 2019.]*

3.3.3 UCP2 facilitates MCU anchoring to methylated MICU1 in the IBM

Recent findings established that asymmetric methylation of MICU1 by arginine M-methyltransferase 1 (PRMT1) desensitizes its binding to Ca^{2+}, thereby causing decreased mitochondrial Ca^{2+} uptake through the uniporter complex[14]. Uncoupling protein 2 (UCP2) can

specifically bind to methylated MICU1, and in doing so restore Ca^{2+} influx into the mitochondrion. Accordingly, the roles PRMT1 and UCP2 play in sub-mitochondrial MCU dynamics during Ca^{2+} mobilization were examined. These experiments were accomplished by generating a UCP-2 knockout (UCP2-KO) HeLa cell line that expresses MCU-mCherry. In contrast to control cells, MCU did not localize to the IBM in response to histamine stimulation of these cells (Figure 58) [96].

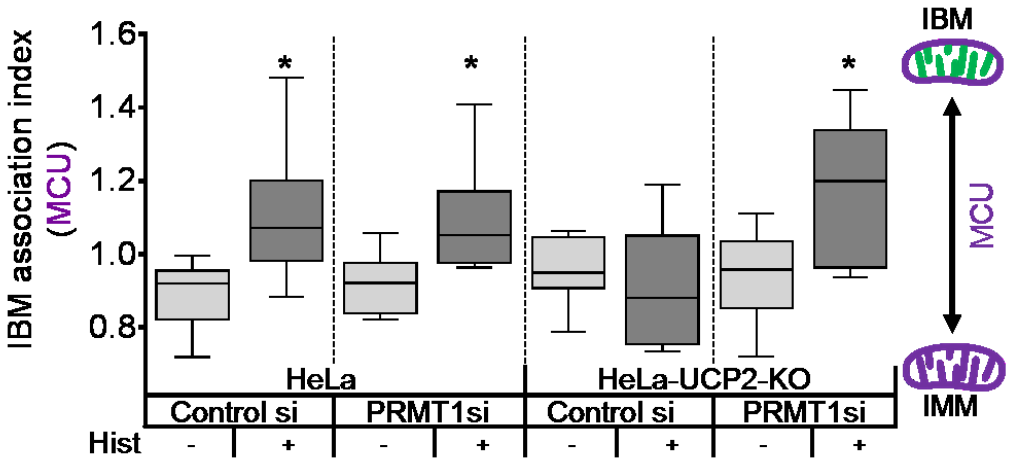

Figure 58: ***MCU shuttling is regulated by PRMT1 and UCP2.*** *Statistical analyses of the sub-mitochondrial localization of MCU-mCherry were carried out on control (HeLa) and UCP2$^{-/-}$ (HeLa-UCP2-KO) cells with and without PRMT1 knock-down under resting conditions and 90 s after stimulation with 100 µM histamine. Analyses were obtained from at least 5 cells each in 8 experiments (n = 8). *P< 0.05 vs. respective control conditions carried out with unpaired double-sided T-test[96]. [Figure reproduced from Gottschalk et al., Nature Communications 2019.]*

Furthermore, mitochondrial Ca^{2+} uptake following histamine treatment was clearly reduced in UCP2-KO cells (Figure 58), even though strong cytosolic Ca^{2+} signals occurred as expected (Figure 59). Knock-down of PRMT1 in UCP2-depleted cells, however, restored Ca^{2+}-evoked MCU accumulation in the IBM (Figure 58) as well as mitochondrial Ca^{2+} uptake (Figure 59) [96].

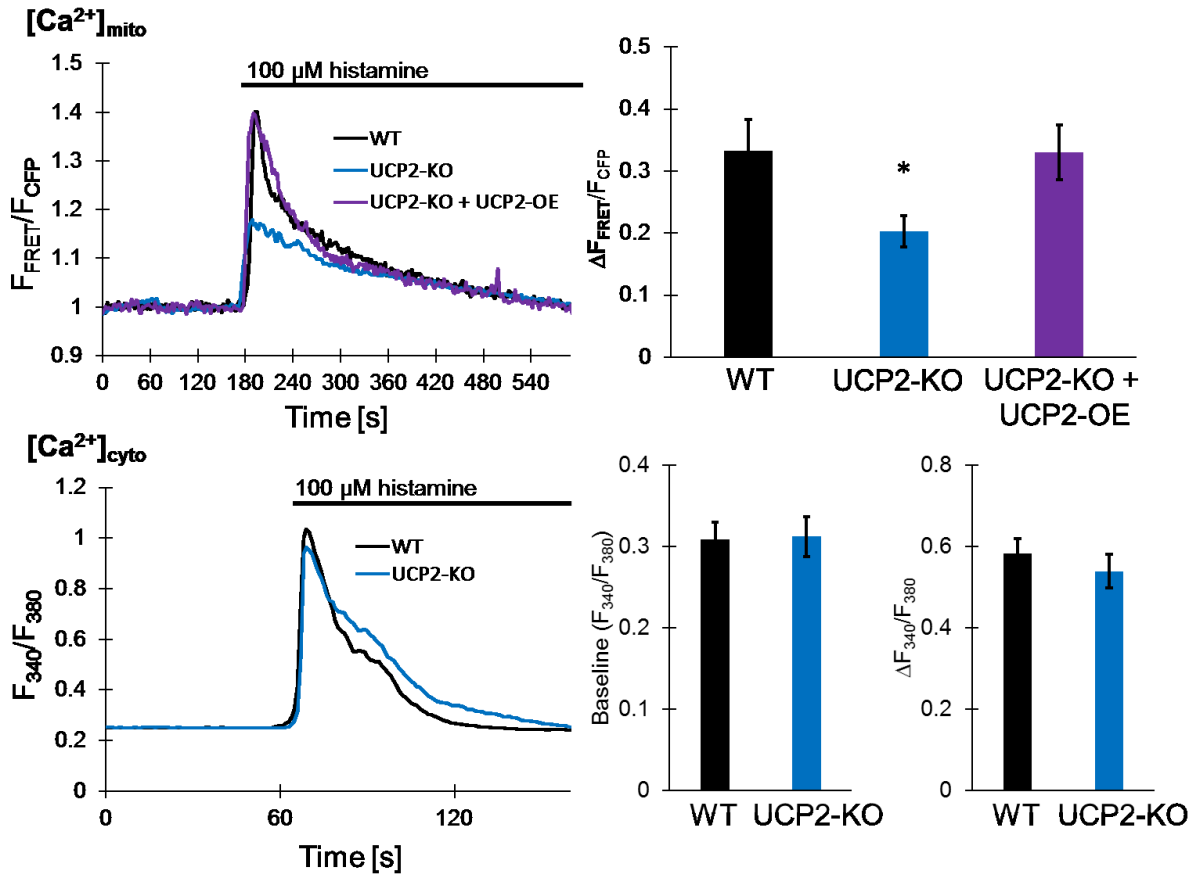

*Figure 59: Mitochondrial Ca^{2+} concentrations are decreased while cytosolic Ca^{2+} signals upon histamine stimulation are not altered in HeLa UCP-KO cells. (Upper panel) HeLa or HeLa-UCP2-KO cells were transfected with 4mt3cpv while HeLa-UCP2-KO cells were co-transfected with or without an UCP2-overexpression plasmid. Cells were treated with 100 µM histamine and mitochondrial Ca^{2+} signals were recorded over time. The upper panel shows representative experiments of HeLa, HeLa-UCP2-KO and the UCP2 recovery in HeLa-UCP2-KO cells. Bars represent maximal Δ FRET ratio values (mean ± SEM) extracted from curves ($n_{Control}$ = 11; $n_{UCP2\text{-}KO}$ = 18; $n_{UCP2\text{-}KO/UCP2\text{-}OE}$ = 12). (Lower panel) HeLa or HeLa-UCP2-KO cells were incubated with Fura-2 and cytosolic Ca^{2+} signals were recorded upon treatment with 100 µM histamine. The lower panel shows representative experiments of HeLa and HeLa-UCP2-KO cells. Bars represent baseline measurements F340/F380 and maximal ΔF340/F380 ratio values (mean ± SEM) extracted from curves. Time-lapse traces and analyses were obtained from at least 3 cells in 4 different experiments on 3-4 independent days ($n_{Control}$ = 9; $n_{UCP2\text{-}KO}$ = 9). *= P<0.05vs. respective control conditions carried out with analysis of variance (ANOVA) with Bonferroni post-hoc test[96]. [Figure reproduced from Gottschalk et al., Nature Communications 2019.]*

The overexpression of PRMT1 in either control or UCP2-KO cells did not influence the sub-mitochondrial localization of MCU nor MICU1 (Figure 60) [96].

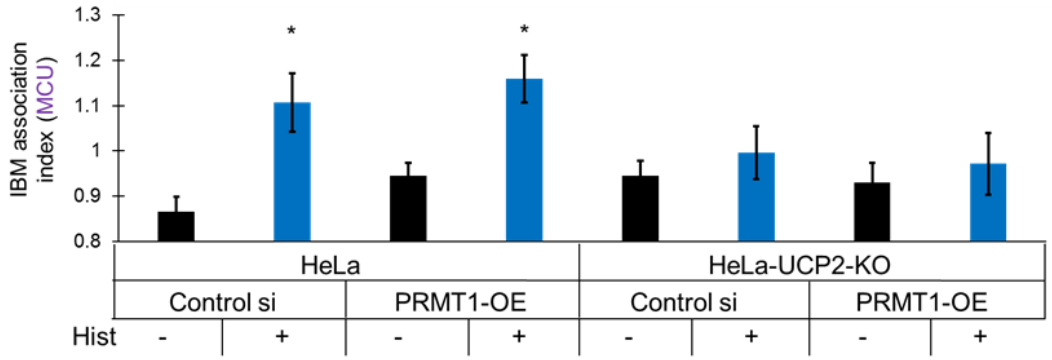

Figure 60: ***PRMT1-OE does not change the sub-mitochondrial localization of MCU in HeLa cells.*** *MICU1-YFP and MCU-mCherry were expressed in control HeLa and UCP2-KO-HeLa cells with and without PRMT1 knock-down. Sub-mitochondrial localization of MCU-mCherry was analyzed with and without histamine treatment. Images and analyses were obtained from at least 10 cells in 2 different experiments on 4 independent days (n = 8). *P<0.05 vs. respective control conditions calculated with unpaired double sided T-Test[96]. [Figure reproduced from Gottschalk et al., Nature Communications 2019.]*

Our next experiments examined the distribution of UCP2-mCherry in Mitotracker Green® (MTG)-stained cells under resting conditions, and during stimulation with histamine. For this purpose, HeLa cells were used that have high levels of methylated MICU1 and therefore require UCP2 for MCU-complex activation. Like MCU, UCP2 occurred throughout the IMM of these cells under basal conditions but accumulated in the IBM upon Ca^{2+} mobilization (Figure 61). Depletion of either MICU1 or PRMT1 prevented this Ca^{2+}-evoked redistribution of UCP2 (Figure 61), pointing to a dynamic interaction of methylated MICU1 dimers with UCP2 [96].

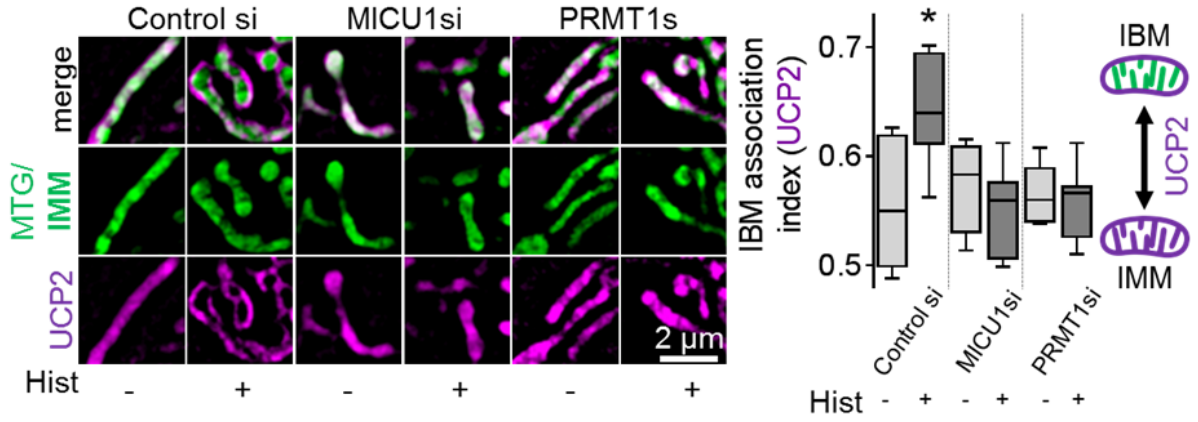

Figure 61: ***UCP2 shuttles to the IBM in a Ca^{2+}, MICU1, and PRMT1-dependent manner.*** *(Left panel) Representative SIM images of cells expressing UCP2-mCherry (magenta) and stained with MTG (green) in the presence (Control si) or absence of endogenous MICU1 (MICU1si) or PRMT1 (PRMT1si) under resting conditions (-) and 90 s after stimulation with 100 µM histamine (+). (Right panel) Analysis of the sub-mitochondrial localization of UCP2 during the experiments described in the left panel (n = 8). *P< 0.05 vs. respective control conditions carried out with unpaired double-sided T-test[96]. [Figure reproduced from Gottschalk et al., Nature Communications 2019.]*

Overexpression of PRMT1 did not change the shuttling characteristics of UCP2 or MCU in HeLa or UCP2-KO cells (Figure 60 and Figure 62) [96].

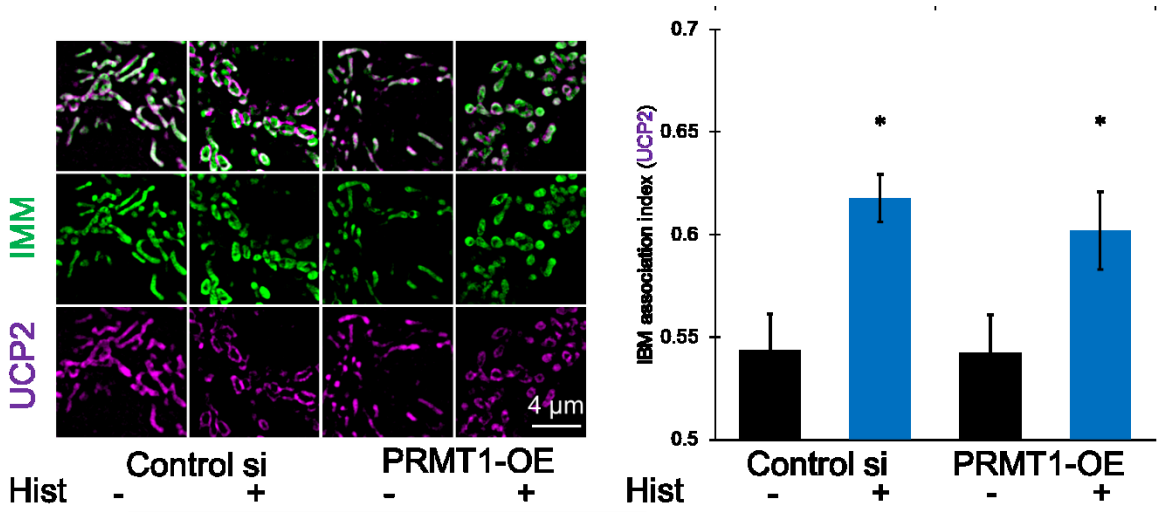

*Figure 62: **PRMT1-OE does not change the sub-mitochondrial localization of UCP2 in HeLa cells.** HeLa cells transfected with UCP2-mCherry with or without parallel overexpression of PRMT1 and stained with MTG. They were imaged with 3D-SIM with or without the presence of histamine. Sub-mitochondrial localization of UCP2-mCherry was analyzed. Images and analyses were obtained from at least 10 cells in 2 different experiments on 4 independent days (n = 8). *P<0.05 vs. respective control conditions calculated with unpaired double sided T-Test[96]. [Figure reproduced from Gottschalk et al., Nature Communications 2019.]*

The arginine at position 455 of MICU1 has been identified as a PRMT1 methylation site that is crucial for the engagement of UCP2, and consequently, mitochondrial Ca^{2+} uptake[14]. Therefore, HeLa cells were transfected to express MICU1-R455F-YFP or MICU1-R455K-YFP, which are mutants that either mimic or prevent methylation of the protein, respectively. In agreement with our previous work, depletion of PRMT1 in cells expressing the MICU1-R455F-YFP mutant did not affect the accumulation of UCP2 in response to histamine stimulation (Figure 63). In contrast, Ca^{2+} mobilization did not cause UCP2 translocation to the IBM in MICU1-R455K-YFP-expressing cells, despite substantial constitutive PRMT1 activity [96].

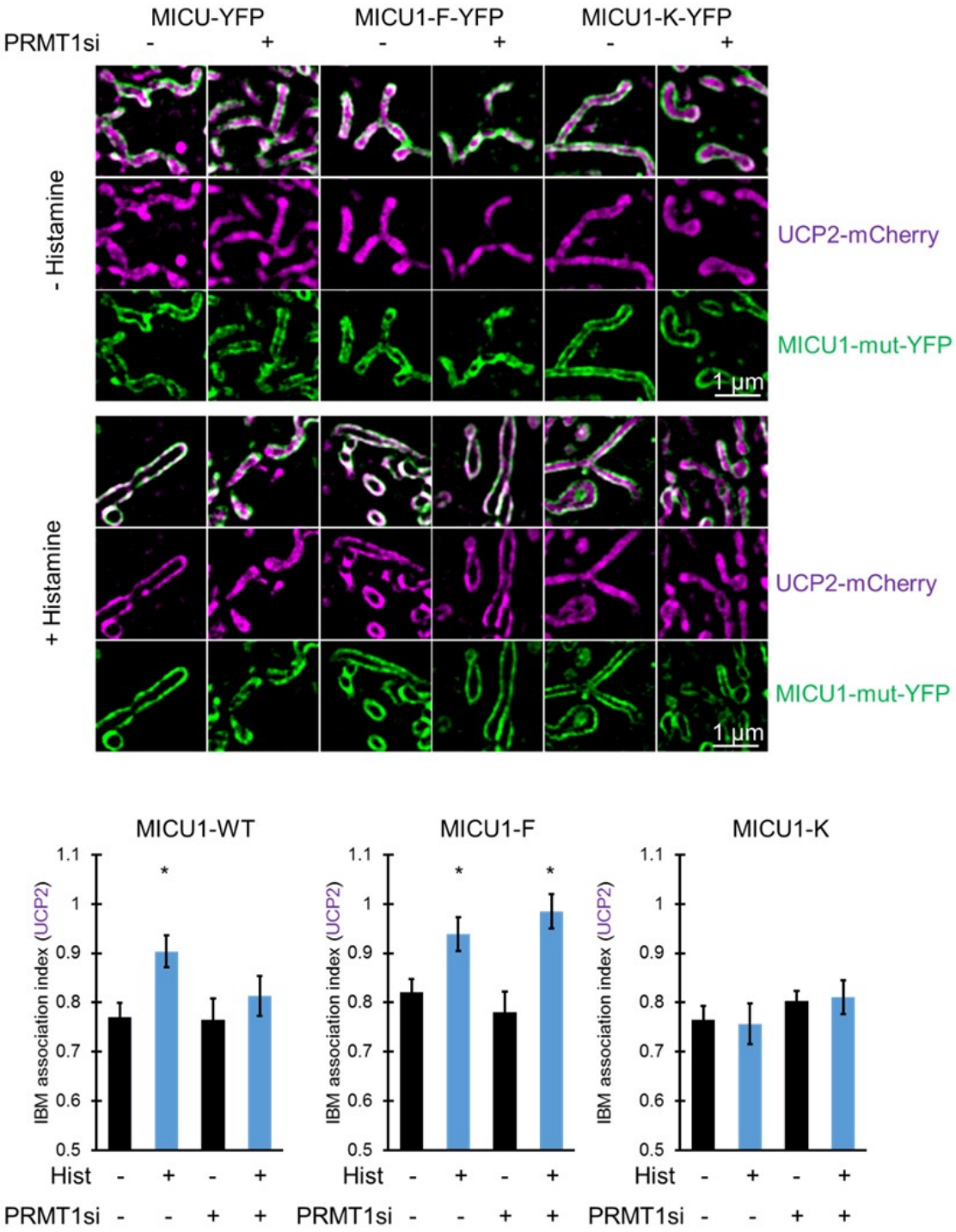

Figure 63: ***UCP2 translocation is influenced by MICU1-K and MICU1-F expression in HeLa cells.*** *HeLa cells were transfected with UCP2-mCherry and ether MICU1-YFP, or the MICU1 Mutants MICU1-K-mut-YFP or MICU1-F-mut-YFP while endogenous MICU1 was knocked down with nonCDSMICU1 siRNA. Additionally, cells were treated with or without PRMT1 siRNA and imaged with and without histamine treatment. The upper panel shows representative images of mitochondria under various conditions. In the lower panel, the quantitative analysis of UCP2-mCherry sub-mitochondrial localization in cells expressing MICU1-YFP, MICU1-K-mut-YFP or MICU1-F-mut-YFP with and without PRMT1 knock-down and with and without histamine treatment is shown. Images and analyses were obtained from at least 10 cells in 2 different experiments on 3 independent days (n = 6). *P<0.05 vs. respective control conditions calculated with unpaired double sided T-Test[96]. [Figure reproduced from Gottschalk et al., Nature Communications 2019.]*

4 Discussion

As proof of principle, structured illumination microscopy was used in this study to determine the sub-mitochondrial localization of different mitochondrial proteins tagged with the fluorescent protein mCherry. MCU, UCP2, and ERME were located at the IMM indicated by co-localization with the IMM-marker MTG. TOM22 on the other side localized to the IBM creating a mitochondrial surrounding corona indicating the OMM localization. Further, SIM was used to discriminate between the IMM and the mitochondrial matrix. A dual-color SIM time lapse of cells labeled with MTG and transfected with MtDsRed was acquired. Due to the higher resolution of SIM compared to confocal or wide field imaging clear IMM structures and their dynamics can be observed. Additionally, the MTG and MtDsRed staining were excluding themselves, principally demonstrating the power of spatial discrimination of dual-color SIM.

The spatial power in resolution and the organelle-specific fluorophore MTG in combination with a robust and sensitive image processing strategy were utilized to elaborate whether IMM-dynamics, in particular CM-dynamics, have a correlation with physiological alterations of IMM-structure proteins like OPA1 or if the kinetics are influenced by Ca^{2+} signaling. The knock-down of OPA1 resulted in a reduction of CM-dynamics while the IBM-dynamics was not altered. A knock-down of OPA1 is associated with a broadening of CJ [29,33,98] allowing a Ca^{2+} influx into the cristae and increasing mitochondrial matrix Ca^{2+} [99], impairs respiratory chain super-complexes and, thus, respiration [34], and increase the susceptibility of the organelle for apoptotic stimuli [28,33]. The facts of widened CJ and reduced CM-dynamics in OPA1 knock-down cells indicate that the widened cristae structure establishes a higher diffusion resistance of the cristae invaginations, thus, yielding reduced CM-dynamics (Figure 64).

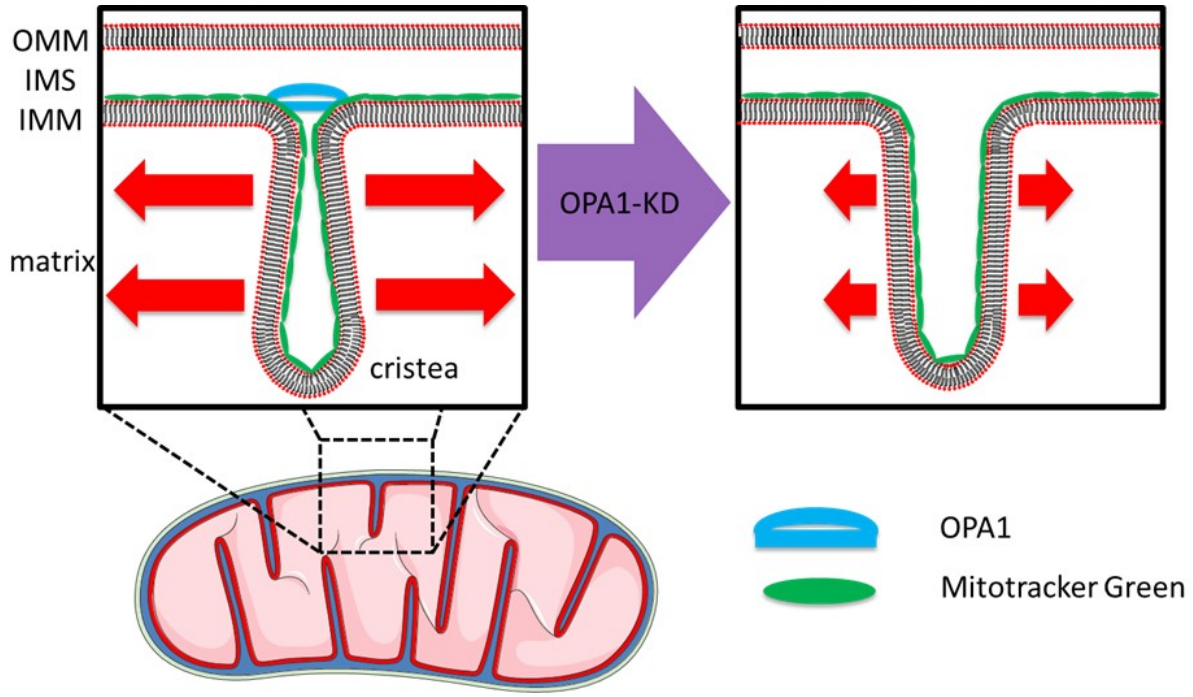

Figure 64: ***Schematic representation of the opening of the CJ in case of OPA1 knock-down****. The IMM kinetics slow down because of the increase of the CJ and the accompanied higher diffusion resistance.*

Inter-organelle exchange of information and metabolites between mitochondria and the endoplasmic reticulum is mediated predominantly through mitochondria-associated ER membranes. A tight coupling between the outer mitochondrial membrane and the ER facilitated by e.g. mitofusin 2[100], the inositol 1,4,5-trisphosphate receptors (IP_3R-Grp75-VDAC complex [45], or VDACs (voltage-dependent anion channels) [37], enables an efficient mitochondrial Ca^{2+} intake upon IP_3-mediated ER Ca^{2+} release [101,102]. Our results show that the kinetics of the IMM movement in close proximity to the ER are significantly slower compared to the whole mitochondrial IMM. This could be explained by two different possible scenarios. **(I)** In the case of mitochondria-mitochondria interaction sites, it was shown that the IMM, specifically the CM, is aligning between different mitochondria[103]. One probable scenario would be that the IMM, in particular the CM, is tethered to the ER-membrane and thereby the movement of the CM in close proximity to the ER is hindered in lateral movement. **(II)** Otherwise, like the reduced CM-kinetics in OPA1 knock-down cells could be interpreted as a cristae opening and accompanied deceleration of CM-dynamics due to higher CJ diameter, the reduced CM-kinetics in close proximity to MAMs might be a result of CJ opening in MAM areas as well.

Measurements of CM dynamics after ER Ca^{2+} release show a significant reduction in CM-kinetics in MAMs, pointing to a Ca^{2+} controlled mechanism of CM dynamics. MAMs are known to be Ca^{2+} hotspots[104]. Chelation of Ca^{2+} by BAPTA normalized CM dynamics in the proximity of MAMs to that of the global mitochondria. This potentially represents an involvement of spatially localized Ca^{2+} in the regulation of CM dynamics within the MAMs even under resting conditions.

Furthermore, it was tested whether the mitochondrial matrix Ca^{2+} was involved in the control of CM-kinetics. Knock-down of MCU did not show any influence on CM-dynamics stating that a reduced mitochondrial Ca^{2+} uptake is not affecting CM-kinetics neither in whole mitochondria nor in mitochondria in close proximity to ER.

MICU1 (mitochondrial calcium uptake 1), a key regulator of MCU [10], owning gatekeeper properties towards MCU and sensing Ca^{2+} with its both EF-Hand motives in the intermembrane space [20,22,97], was knocked down in HeLa cells. A clear reduction of CM-kinetics could be observed under resting conditions in whole mitochondria and mitochondria in close proximity to the ER likewise to an OPA1 knock-down. Additionally, mitochondrial branching was significantly reduced in MICU1 knock-down cells, again with high similarities to OPA1 knock-down cells. This indicates a role of MICU1 within the CJ formation and stabilization and a CM-kinetics regulation emerging from the mitochondrial intermembrane space Ca^{2+} concentration.

MICU1 is known to form hexamers or oligomers in its resting condition. Upon Ca^{2+} elevation in the IMS, MICU1 binds Ca^{2+} with its EF-Hands and forms dimers [12]. The K_d value of MICU1 dimer formation was estimated to be 4.4 µM Ca^{2+} in HeLa cells [12]. MAMs were identified as Ca^{2+} hot spots with elevated Ca^{2+} concentration between 3.78 and 16.42 µM after challenging with the IP_3 generating agonist histamine[104] compared to cytosolic Ca^{2+} concentration after ER Ca^{2+} release of 0.5 – 1.0 µM[105]. The K_d of MICU1 dimer formation and MAM Ca^{2+} levels after histamine treatment lead to the assumption that the differential CM-kinetics observed in between whole mitochondria and MAM related areas might be driven by a MICU1 dimer/hexamer equilibrium shifted more towards dimer formation in MAMs.

To further elaborate whether MICU1 is involved in the CM-dynamics and whether it has similar functions like OPA1 regarding CJ-stability the sub-mitochondrial localization of MICU1 was investigated. HeLa cells were transfected with MICU1-YFP, counterstained with MTR and imaged with dual-SIM. While the MTR staining revealed a clear cristae structure, the MICU1-YFP localized to the outer shell of the mitochondria creating a corona like structure. To clarify whether the MICU1-YFP construct was not miss targeted to the OMM, HeLa cells were co-transfected with MICU1-YFP and TOM22-mCherry. TOM22 is a part of the outer mitochondrial membrane protein import machinery and is known to localize to the OMM[106]. A distance between the MICU1-YFP and TOM22-mCherry staining of approximately 22 nm could be measured matching the distance in between the IBM and OMM measured by electron microscopy [23]. As the measured differences of MICU1 and TOM22 were well below the resolution limit of our microscopic setup, extensive models and calculations, as well as a thorough characterization of the imaging system, were done. These measurements confirmed the ability of the microscopic setup to measure below the resolution limit applying a hollow barrel model and double Gaussian fits. Being sure about the localization of MICU1-YFP the emerging key questions were how MICU1-YFP could maintain its localization at the IBM? Especially, with the background in mind that MICU1 was located previously by electron microscopy to the entire IMM[107], and what functional property is covered by its IBM localization?

MICU1 has two crucial properties emerging from its poly-lysine-domain and helical C-terminal domain which give rise to its unusual localization at the IBM in mitochondria. (i) The C-terminal domain is essential for MICU1 oligomerization[97]. The absence of this region leads to a drastic reduction of mitochondrial membrane potential likewise the absence of endogenous MICU1 or OPA1. Further, a knock-down of MICU1 or OPA1 leads to a rearrangement of the C-terminal truncated mutant of MICU1 into the CM and to an increase of the CJ width. These results manifest the assumption that MICU1 is stabilizing the CJ while its IBM localization is dependent on a closed and tight CJ, pointing to a self-containing mechanism of MICU1. (ii) It is anticipated, while still not experimentally confirmed, that the cristae lumen has a pH lower than the IMS

reasoned by the localization of the electron transport chain complexes I, III, and IV and F_0F_1-ATP-synthase to the CM[26,27]. Recently a pH gradient was observed between the F_0F_1-ATP synthase and complex IV using genetically encoded pH-sensors[108], pointing at least to the possibility of different IMM characteristics across sub mitochondrial segments like suggested by Klotzsch et al [61]. The poly-lysine-domain adds a positive charge to MICU1, is located within the protein structure close to the proposed mitochondrial targeting sequence of MICU1 [10,97], and the peptide motive, in general, is known to interact with membranes [109–111]. The fact that MICU1 IBM localization is dependent on the intact membrane potential and that mutants lacking the poly-lysine domain localize throughout the IMM lead to the conclusion that MICU1 is binding to the IMM by its poly-lysine domain depending on the local pH environment. While the phosphate groups of phospholipids (in particular of cardiolipin with a pK_s of 7.5 [112]) in the low cristae pH are protonated and cannot interact with the poly-lysine domain, the IBM , due to the CJ compartmentation, has a proposed higher pH resulting in non-protonated phosphate groups leading to electrostatic interaction between the basic poly-lysine domain and the IBM. Further evidence for this theory is delivered by reports of direct MICU1 and cardiolipin interaction [20] and by taffazin [113] knock-down experiments conducted in this study showing a strong correlation of MICU1 IBM localization and the abundance of cardiolipin. MICU1 is supporting the CJ stability with its hexameric structure but is dependent on the compartmentation of the cristae lumen and IMS in regard to the pH and subsequent interaction of MICU1 with the IBM. Both the poly-K and C-terminal domain are essential components of the self-containing mechanism restricting MICU1 to the IBM (Figure 65).

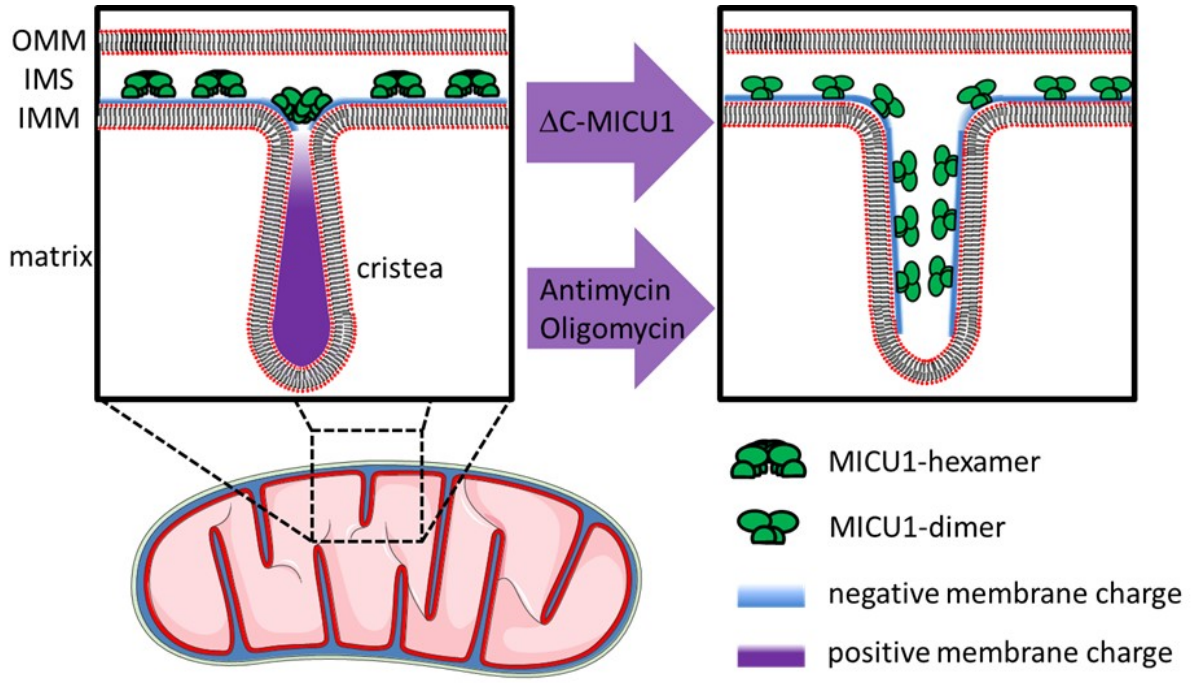

Figure 65: ***Schematic representation of the impact of ΔC-MICU1 expression or antimycin A/oligomycin A treatment of Hela cells on the mitochondrial membrane potential and pH-gradient across the CJ.*** *While the knock-down of wt-MICU1 and expression of ΔC-MICU1, lead to a permanent weakening of the CJ and disturbance of the membrane potential leading to the homogenous distribution of ΔC-MICU1 across the IMM, the direct application of antimycin A and oligomycin A destroys the membrane potential and enable MICU1 to diffuse into the CM.*

Additionally, the Ca^{2+} dependent impact of MICU1 on the CJ might explain the different IMM-kinetics in close proximity to the ER compared to the rest of the mitochondria, higher mitochondrial fragmentation, and lower branching. High Ca^{2+} levels, especially reached in MAMs[104] could lead to a higher local shift of a MICU1 oligomer to dimer ratio after ER-Ca^{2+} release, increasing the opening probability of the CJ in MAMs and leading to the observed reduction of IMM-kinetics under histamine induced ER-Ca^{2+} release conditions compared to the rest of the mitochondrion (Figure 66). The local opening of the CJ in the MAMs also might explain the increased fragmentation of mitochondria after ER-Ca^{2+} release. Several reports showed that mitochondrial fission appears especially in MAMs[48] while the influence of the IMM structure and especially CJ was not taken into consideration so far.

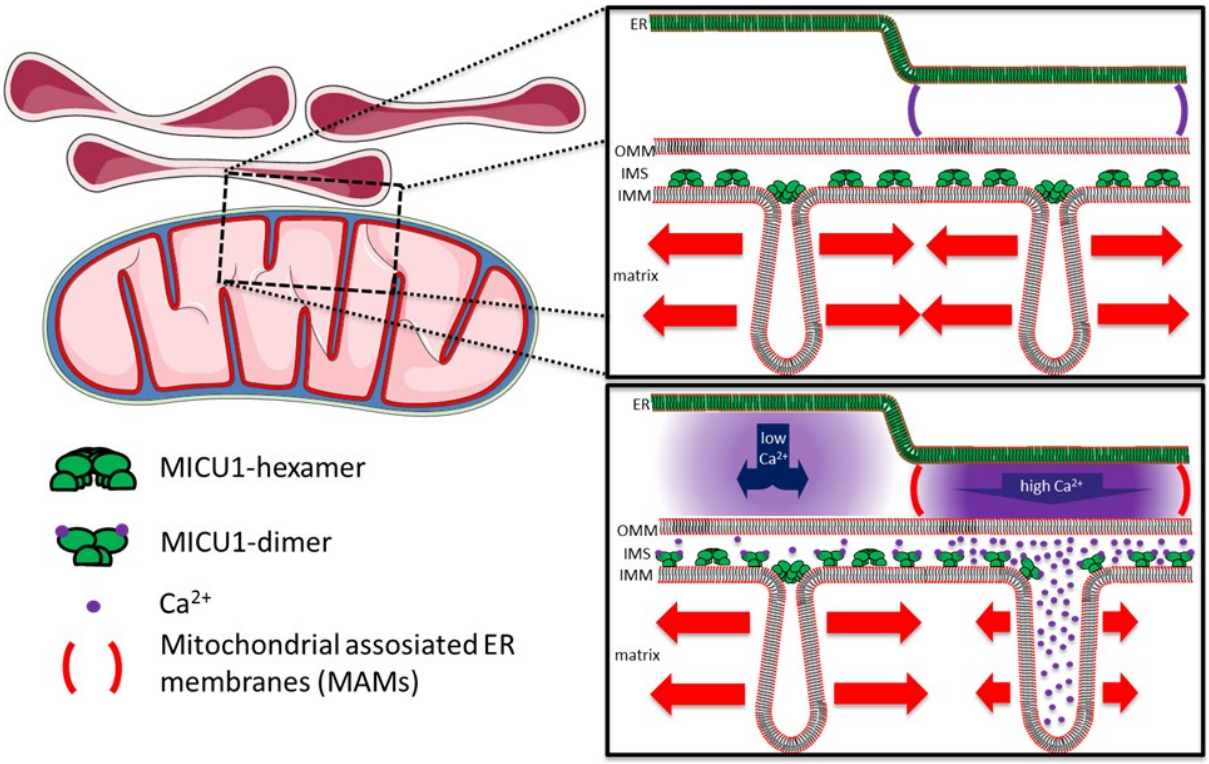

Figure 66: ***Schematic representation of MICU1 influence on cristae kinetic regulation upon ER Ca^{2+} release.*** *During ER Ca^{2+} release mitochondrial-ER junctions represent cytosolic areas with highly increased Ca2+ concentrations. As the OMM is permeable for Ca^{2+} these concentrations directly apply to the IBM and IMS. High concentrations of Ca^{2+} in regions with close proximity to MAMs lead to a complete disassemble of MICU1 at the CJ. Due to the lack of MICU1 stabilization the CJ widens and the cristae kinetics stall in MAM areas and increase fission activity. Ca^{2+} concentrations in non-MAM areas are not sufficient to disassemble MICU1 completely, but rather partially, leaving the CJ intact, protecting from loss of membrane potential, rearrangement of cytochrome c and excessive cristae lumen Ca^{2+} uptake.*

The widening of the CJ observed with electron microscopy in MICU1 or OPA1 silenced HeLa cells was not influenced by parallel knock-down of MCU and EMRE highlighting that CJ width is independent of basal Ca^{2+} elevation in the mitochondrial matrix. The widening of the CJ as a result of MICU1 or OPA1 knock-down leads to a reduction of the mitochondrial membrane potential (Figure 67), a release of cytochrome c from the cristae lumen into the IMS (Figure 67) and an increase of the basal cristae Ca^{2+} concentration (Figure 67). All these factors are involved into the process of the induction of apoptosis and shed some light on recent studies stating higher cell death of MICU1 knock-down tumor-derived cells compared to controls when treated with the cytotoxin Cisplatin [114]. Furthermore, *in vitro,* an increase in oxygen consumption rates, decreased lactate production, inhibition of clonal growth and migration and invasion of ovarian cancer cells were observed[114]. While the knock-down of MICU1 alone might not induce apoptosis or decrease cell viability shown by our results, the vulnerability of cells

with reduced stability of CJ combined with cell toxic drugs leads to increased apoptosis. Recent reports also showed that developmental lethality of MICU1 knockout flies to apoptotic stimuli could not be recovered by parallel knockout of MCU or EMRE [115]. This implicates that increased apoptosis in MICU1-KO flies is not directly correlated to increased matrix Ca^{2+} levels and overflow, but rather to a Ca^{2+} independent mechanism like the release of cytochrome c from the cristae.

The finding of increased basal cristae lumen Ca^{2+} concentrations, while IMS Ca^{2+} remained unchanged, in MICU1 or OPA1 silenced HeLa cells are in line with reports of increased mitochondrial initial Ca^{2+} uptake velocity in cells depleted from MICU1 or OPA1[99,116]. Anyhow, the rapid increase of the cristae lumen Ca^{2+} upon intercellular Ca^{2+} release even in the presence of MICU1 points to a Ca^{2+} regulated gatekeeper function of MICU1 in the CJ. In line with increased cristae lumen Ca^{2+}, matrix Ca^{2+} is elevated in MICU1 or OPA1 knock-down cells as well. Most likely the widened CJ allows penetration of Ca^{2+} into the cristae where active (not negatively controlled by MICU1) MCU-complexes are located.

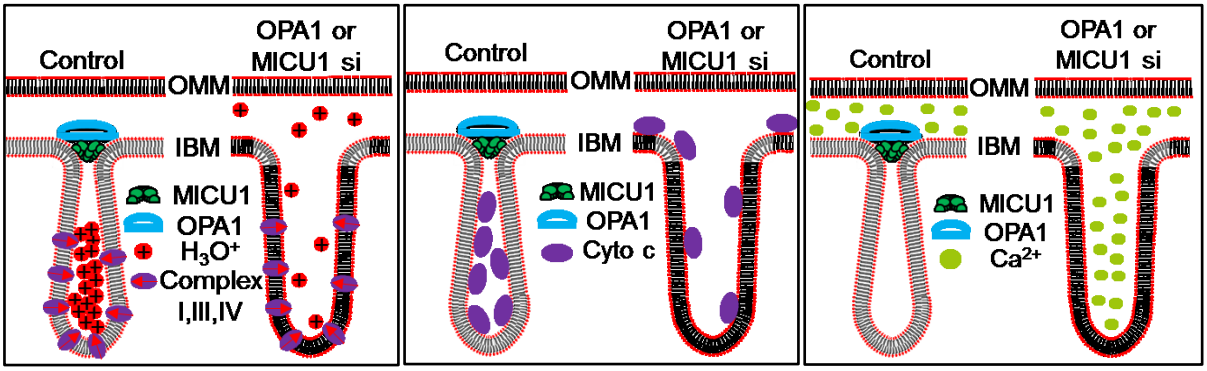

Figure 67: ***Schematic representation of the influence of OPA1 or MICU1 knock-down on the CJ.*** *Opening of the CJ by silencing of OPA1 or MICU1 leads to a loss of membrane potential (left panel), redistribution of cytochrome c (middle panel) and increased basal Ca^{2+} in the cristae lumen (right panel) [96]. [Figure reproduced from Gottschalk et al., Nature Communication 2019.]*

MCU, EMRE, and UCP2 are located to the entire IMM under resting conditions (passage 3.1.1; page 36). This finding was contradicting findings of close interaction and binding of MICU1 to MCU[10,117] as MICU1 was found exclusively in the IBM in this study. However, after stimulation with histamine MCU relocalizes predominantly into the IBM joining MICU1. MCU shuttling was only observed in MICU1-YFP or MICU1 overexpression situations, pointing on a mechanism

in need of specific stoichiometric MICU1/MCU ratio. These results indicate a dynamic assembly of the MCU-complex at the IBM in a MICU1 and Ca^{2+} dependent manner. Furthermore, EMRE was found to shuttle to the IBM only in situations of MCU and MICU1 co-expression. In conclusion, this work shows that MCU binds in a Ca^{2+} dependent manner to MICU1 while EMRE binds to MCU and not MICU1. That finding stands in conflict with reports showing direct binding of EMRE to MICU1, potentially by electrostatic interaction of the polybasic domain of MICU1 with the C-terminus of EMRE[22,118]. However, the group of Kevin Foskett determined a matrix orientation of the EMRE C-terminal region[13], and therefore not able to interact with MICU1, which is localized in the IMS/IBM[11]. Combining these results with the finding of no observable interaction of MICU1 and EMRE in living cells leads to the conclusion that interactions of EMRE and MICU1 found by co-immunoprecipitation are the result of a lysis and membrane permeabilization artifact. The process of protein extraction leads at least to distorted and fragmented membrane structures in which EMRE resides. Interactions of proteins might be detected with co-immunoprecipitation, which under physiological conditions due to trans-membrane orientations are not binding to each other directly. Anyhow, the localization of MICU1 to the IBM depends as shown in this work on its poly-lysine domain, which is a potential binding motive for cardiolipin[20]. While MICU1 interaction with cardiolipin might explain the IBM restriction, interaction with EMRE could not, as EMRE resides in the whole IMM.

MCU did not distribute to the IBM when co-expressed with ΔC-MICU1 under endogenous knock-down of MICU1. As ΔC-MICU1 is not binding to MCU[97] the MCU shuttling is specifically dependent on the interaction of MICU1 and MCU. Further, the dynamic assembly of the MCU-complex after histamine treatment at the IBM of time was measured, showing a high temporal correlation with mitochondrial Ca^{2+} signals. The MCU-shuttling process was also confirmed in HEK, MCF-7 and A549 cells proving the mechanistic principle in non-excitable cell lines. While the dynamic translocation of MCU into the IBM was never shown before, Dong et al. published an article describing the activation of MCU by hydrogen peroxide and its accompanied redistribution in the IBM with STED and STORM microscopy[119]. The dynamic assembly of

MCU in the IBM is independent of extracellular Ca^{2+} but requires a rise in cytosolic and IMS Ca^{2+} as well as the presence of MICU1. In fact, Ca^{2+} increase in the IMS triggers MICU1 dimerization[12] which in turn acts as a Ca^{2+} inducible and reversible diffusion trap for the MCU-complex at the IBM. A plausible implication of the mechanism is a constant activity of the MCU-complex, graded by the MICU1 dependent stability of the CJ.

Several non-excitable cells like HeLa, HEK, A549, or MCF-7 cell lines were confirmed for the MCU-shuttling process. Excitable cells like neurons, myocytes or insulin-secreting β-cells might rely on altered or different processes and mechanisms of mitochondrial Ca^{2+} signaling and parallel cell protection dependent on the abundance of MCU-complex members (e.g. MICU2 and MICU3)[18,120], posttranslational modifications (phosphorylation, methylation, and oxidation)[11,14,119], the stoichiometry of MCU-complex members[15] or the abundance of cardiolipin[113].

Recent findings established a decrease in Ca^{2+} binding affinity of MICU1 when methylated by PRMT1 (protein arginine methyltransferase 1), which inhibits its ability to dimerize[14]. MICU1 methylation reduced mitochondrial Ca^{2+} uptake mediated by MCU. UCP2 (uncoupling protein 2) is able to bind specifically to methylated MICU1, restore its Ca^{2+} sensitivity and in consequence MCU Ca^{2+} uptake[14].

PRMT1 is generally highly expressed in HeLa cells[14]. UCP2-knockout cells derived from this cell line were not able to shuttle MCU into the IBM during intercellular Ca^{2+} release. Silencing of PRMT1 in UCP2-KO cells recovered the MCU-shuttling process. A high correlation of the MCU shuttling mechanistic with previous findings of MCU mediated Ca^{2+} entry into mitochondria controlled by UCP2 and PRMT1 can be drawn[14].

Besides the work of the group of Elena Pohl that reported an IBM localization of UCP4[61], other members of the UCP family were not characterized in regard to their sub-mitochondrial localization. Results in this work show UCP2 to be localized in the whole IMM under resting conditions but it undergoes relocation to the IBM in a PRMT1 and MICU1 dependent manner

after ER Ca^{2+} release and cytosolic Ca^{2+} increase. These results confirm previous results of specific binding of UCP2 to PRMT1 methylated MICU1[14].

The PRMT1 arginine methylation site of MICU1 at position 455 is essential for UCP2 binding to MICU1 [14]. Two mutants of MICU1, MICU1-R455F, and MICU1-R455K, either mimicking or preventing PRMT1 derived methylation[14], respectively, were used to examine the role of MICU1 in UCP2 translocation to the IBM after ER Ca^{2+} release. UCP2 translocation into the IBM upon ER-Ca^{2+} release was independent of PRMT1 activity when MICU1- R455F was co-expressed. In contrary MICU1- R455K disabled UCP2 shuttling with or without PRMT1 silencing. In conclusion, methylation of MICU1 at position R455 is a prerequisite for the relocation of UCP2 to the IBM and confirm a fundamental role for UCP2 in the assembly and activation of the MCU-complex under conditions of elevated PRMT1 activity[14].

Overall, our data presented here significantly change the current model of the organization, localization, and processes of stimulation of the MCU-complex (Figure 68 & Figure 69).

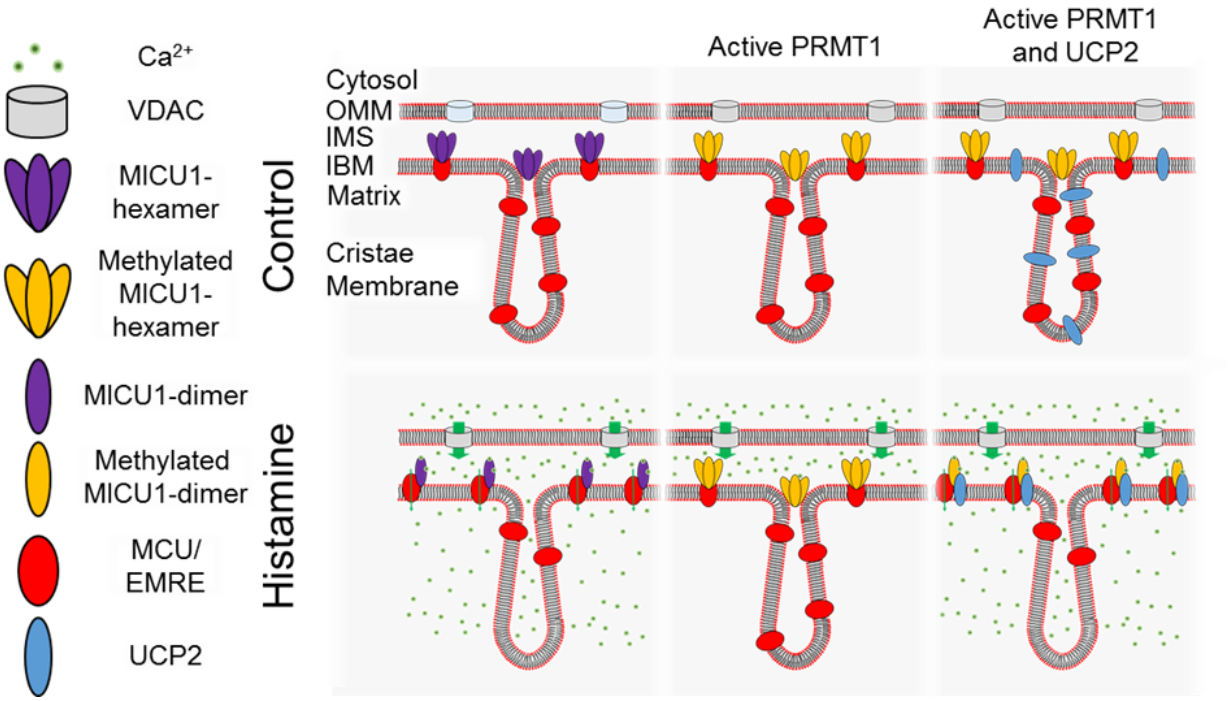

Figure 68: ***Schematic representation of the model of action and regulation of the MCU shuttling process in close proximity to the ER.*** *Model for the sub-mitochondrial localization of MICU1, and localization and assembly of the MCU-complex in regions with close proximity to the ER under resting conditions (Control) and upon IP_3-mediated intracellular Ca^{2+} release (Histamine) in cells with low PRMT1 activity (left), in cells with active PRMT1 lacking UCP2 (middle), and in cells with active PRMT1 and in the presence of UCP2 (right). In the absence of PRMT1 activity, Ca^{2+} spikes in the intermembrane space restructure MICU1 hexamers into dimers in the IBM, where they act as diffusion traps for MCU. These molecules can now anchor EMRE in the IBM, thus assembling MCU-complexes there. In the absence of UCP2, PRMT1 prevents the reorganization of MICU1 into dimers upon intracellular Ca^{2+} release, thus no shuttling of MCU (nor EMRE) to the IBM takes place and no functional MCU-complexes are assembled. However, the presence of UCP2 allows the dimerization of MICU1 even in the presence of elevated PRMT1 activity, and thus restores the diffusion trap capabilities of MICU1 by either stabilizing the methylated MICU1 dimer or preventing the methylated MICU1 oligomer from disrupting it. Consequently, the MCU-complex is assembled and mitochondrial Ca^{2+} uptake is restored [96]. [Figure reproduced from Gottschalk et al., Nature Communication 2019.]*

In particular, MICU1 is exclusively localized in the IBM due to its C-terminal oligomerization and poly-lysine domain. The mitochondrial membrane potential of the IMM and the potential interaction with cardiolipin lead to a self-containing mechanism restricting MICU1 to the IBM where it essentially contributes to the stability of the CJ. By controlling the CJ in a Ca^{2+} dependent manner it is involved in maintaining the membrane potential, restricts cytochrome c to the cristae lumen and protects mitochondria from Ca^{2+} overload. However, ER Ca^{2+} release activates the MCU-complex by MICU1 dissociation into dimers that serve as a diffusion trap for MCU in the IBM. Either MCU anchors subsequently EMRE to the IBM or the MCU core complex (including EMRE and MCU) is already established in the cristae upfront and delocalized to the IBM together. Methylation of MICU1 by PRMT1 desensitizes MICU1 to bind

Ca^{2+}, prevents MICU1 dimerization and MCU trapping at the IBM. However, interaction and binding of UCP2 to MICU1 enables dimerization and MCU-complex assembly (Figure 69). Further, as the process of MICU1 dimerization is critically Ca^{2+} dependent, additionally to the MCU shuttling process, the CJ opens in MAM regions with very high local Ca^{2+} concentrations enabling high Ca^{2+} uptake and potentially mitochondrial fission on the level of the IMM (Figure 68). This new model seamlessly meshes existing data with new findings and provides an advanced perspective on the dynamic organization of mitochondrial ion regulation and how MICU1 by contributing to CJ integrity is essential for maintaining the proton gradients, and, thus, the organelle's energetic functions.

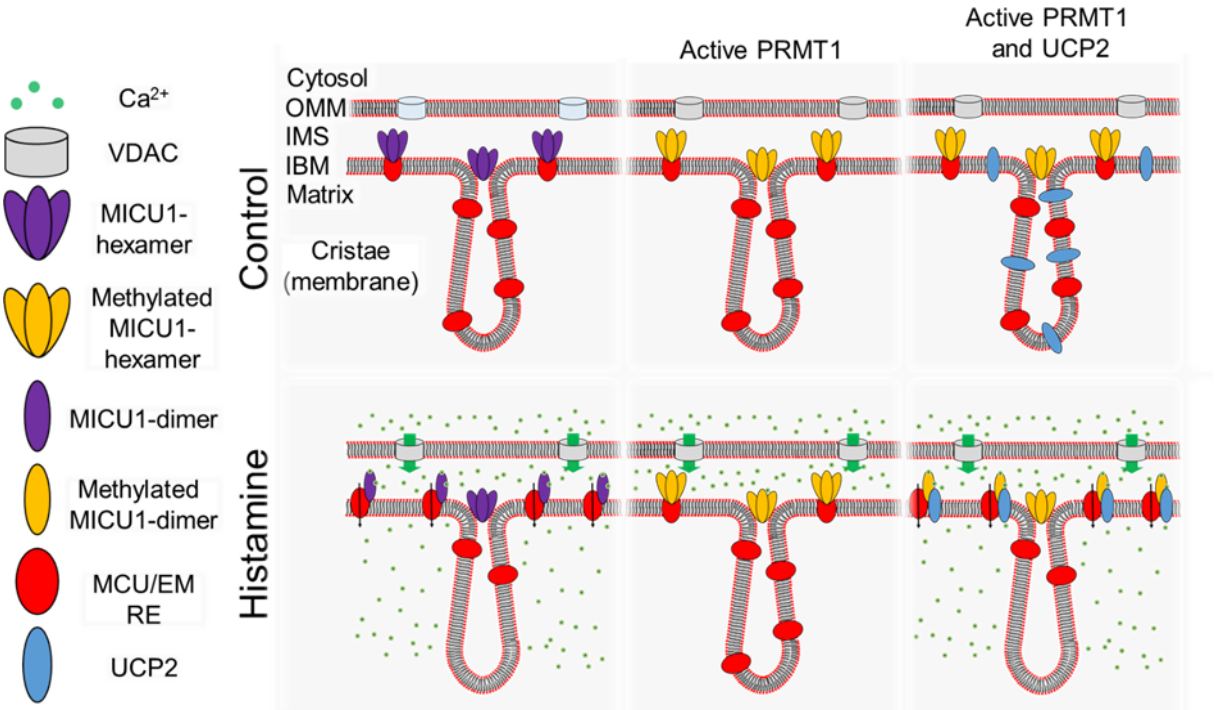

Figure 69: ***Schematic representation of the model of action and regulation of the MCU shuttling process in distance to mitochondrial-ER junctions.*** *Same model as shown in figure 43, but since the Ca^{2+} concentration in regions without close proximity to the ER is lower compared to MAM-close regions, not all MICU1 hexamers are converted to dimers, preserving the CJ intact.*

5 References

1. Rizzuto, R., Stefani, D. de, Raffaello, A. & Mammucari, C. Mitochondria as sensors and regulators of calcium signalling. *Nature reviews. Molecular cell biology* **13,** 566–578; 10.1038/nrm3412 (2012).
2. Walsh, C. *et al.* Modulation of calcium signalling by mitochondria. *Biochimica et biophysica acta* **1787,** 1374–1382; 10.1016/j.bbabio.2009.01.007 (2009).
3. Liu, J. C. *et al.* The In Vivo Biology of the Mitochondrial Calcium Uniporter. *Advances in experimental medicine and biology* **982,** 49–63; 10.1007/978-3-319-55330-6_3 (2017).
4. Kamer, K. J. & Mootha, V. K. The molecular era of the mitochondrial calcium uniporter. *Nature reviews. Molecular cell biology* **16,** 545–553; 10.1038/nrm4039 (2015).
5. Stefani, D. de, Raffaello, A., Teardo, E., Szabò, I. & Rizzuto, R. A forty-kilodalton protein of the inner membrane is the mitochondrial calcium uniporter. *Nature* **476,** 336–340; 10.1038/nature10230 (2011).
6. Baughman, J. M. *et al.* Integrative genomics identifies MCU as an essential component of the mitochondrial calcium uniporter. *Nature* **476,** 341–345; 10.1038/nature10234 (2011).
7. Sancak, Y. *et al.* EMRE is an essential component of the mitochondrial calcium uniporter complex. *Science (New York, N.Y.)* **342,** 1379–1382; 10.1126/science.1242993 (2013).
8. Raffaello, A. *et al.* The mitochondrial calcium uniporter is a multimer that can include a dominant-negative pore-forming subunit. *The EMBO journal* **32,** 2362–2376; 10.1038/emboj.2013.157 (2013).
9. Mallilankaraman, K. *et al.* MCUR1 is an essential component of mitochondrial Ca^{2+} uptake that regulates cellular metabolism. *Nature cell biology* **14,** 1336–1343; 10.1038/ncb2622 (2012).
10. Perocchi, F. *et al.* MICU1 encodes a mitochondrial EF hand protein required for $Ca^{(2+)}$ uptake. *Nature* **467,** 291–296; 10.1038/nature09358 (2010).
11. Marchi, S. *et al.* Akt-mediated phosphorylation of MICU1 regulates mitochondrial Ca^{2+} levels and tumor growth. *The EMBO journal* **38**; 10.15252/embj.201899435 (2019).
12. Waldeck-Weiermair, M. *et al.* Rearrangement of MICU1 multimers for activation of MCU is solely controlled by cytosolic $Ca^{(2+)}$. *Scientific reports* **5,** 15602; 10.1038/srep15602 (2015).
13. Vais, H. *et al.* EMRE Is a Matrix $Ca^{(2+)}$ Sensor that Governs Gatekeeping of the Mitochondrial $Ca^{(2+)}$ Uniporter. *Cell reports* **14,** 403–410; 10.1016/j.celrep.2015.12.054 (2016).
14. Madreiter-Sokolowski, C. T. *et al.* PRMT1-mediated methylation of MICU1 determines the UCP2/3 dependency of mitochondrial $Ca^{(2+)}$ uptake in immortalized cells. *Nature communications* **7,** 12897; 10.1038/ncomms12897 (2016).
15. Paillard, M. *et al.* Tissue-Specific Mitochondrial Decoding of Cytoplasmic Ca^{2+} Signals Is Controlled by the Stoichiometry of MICU1/2 and MCU. *Cell reports* **18,** 2291–2300; 10.1016/j.celrep.2017.02.032 (2017).

16. Petrungaro, C. *et al.* The $Ca^{(2+)}$-Dependent Release of the Mia40-Induced MICU1-MICU2 Dimer from MCU Regulates Mitochondrial $Ca^{(2+)}$ Uptake. *Cell metabolism* **22,** 721–733; 10.1016/j.cmet.2015.08.019 (2015).

17. Kamer, K. J. & Mootha, V. K. MICU1 and MICU2 play nonredundant roles in the regulation of the mitochondrial calcium uniporter. *EMBO reports* **15,** 299–307; 10.1002/embr.201337946 (2014).

18. Patron, M., Granatiero, V., Espino, J., Rizzuto, R. & Stefani, D. de. MICU3 is a tissue-specific enhancer of mitochondrial calcium uptake. *Cell death and differentiation* **26,** 179–195; 10.1038/s41418-018-0113-8 (2019).

19. Mallilankaraman, K. *et al.* MICU1 is an essential gatekeeper for MCU-mediated mitochondrial $Ca^{(2+)}$ uptake that regulates cell survival. *Cell* **151,** 630–644; 10.1016/j.cell.2012.10.011 (2012).

20. Kamer, K. J., Grabarek, Z. & Mootha, V. K. High-affinity cooperative Ca^{2+} binding by MICU1-MICU2 serves as an on-off switch for the uniporter. *EMBO reports* **18,** 1397–1411; 10.15252/embr.201643748 (2017).

21. MacEwen, M. J.S. *et al.* Molecular basis of EMRE-dependence of the human mitochondrial calcium uniporter. *bioRxiv*; 10.1101/637918 (2019).

22. Phillips, C. B., Tsai, C.-W. & Tsai, M.-F. The conserved aspartate ring of MCU mediates MICU1 binding and regulation in the mitochondrial calcium uniporter complex. *eLife* **8**; 10.7554/eLife.41112 (2019).

23. Perkins, G. *et al.* Electron tomography of neuronal mitochondria. Three-dimensional structure and organization of cristae and membrane contacts. *Journal of structural biology* **119,** 260–272; 10.1006/jsbi.1997.3885 (1997).

24. Harner, M. *et al.* The mitochondrial contact site complex, a determinant of mitochondrial architecture. *The EMBO journal* **30,** 4356–4370; 10.1038/emboj.2011.379 (2011).

25. Vogel, F., Bornhövd, C., Neupert, W. & Reichert, A. S. Dynamic subcompartmentalization of the mitochondrial inner membrane. *The Journal of cell biology* **175,** 237–247; 10.1083/jcb.200605138 (2006).

26. Davies, K. M. *et al.* Visualization of ATP synthase dimers in mitochondria by electron cryo-tomography. *Journal of visualized experiments : JoVE,* 51228; 10.3791/51228 (2014).

27. Golic, I. *et al.* Methods for studying the localization of mitochondrial complexes III and IV by immunofluorescent and immunogold microscopy. *Arch biol sci (Beogr)* **68,** 767–772; 10.2298/ABS150618061G (2016).

28. Frezza, C. *et al.* OPA1 controls apoptotic cristae remodeling independently from mitochondrial fusion. *Cell* **126,** 177–189; 10.1016/j.cell.2006.06.025 (2006).

29. Varanita, T. *et al.* The OPA1-dependent mitochondrial cristae remodeling pathway controls atrophic, apoptotic, and ischemic tissue damage. *Cell metabolism* **21,** 834–844; 10.1016/j.cmet.2015.05.007 (2015).

30. Amutha, B., Gordon, D. M., Gu, Y. & Pain, D. A novel role of Mgm1p, a dynamin-related GTPase, in ATP synthase assembly and cristae formation/maintenance. *The Biochemical journal* **381,** 19–23; 10.1042/BJ20040566 (2004).

31. Cipolat, S., Martins de Brito, O., Dal Zilio, B. & Scorrano, L. OPA1 requires mitofusin 1 to promote mitochondrial fusion. *Proceedings of the National Academy of Sciences of the United States of America* **101,** 15927–15932; 10.1073/pnas.0407043101 (2004).

32. Merkwirth, C. *et al.* Prohibitins control cell proliferation and apoptosis by regulating OPA1-dependent cristae morphogenesis in mitochondria. *Genes & development* **22,** 476–488; 10.1101/gad.460708 (2008).

33. Olichon, A. *et al.* Loss of OPA1 perturbates the mitochondrial inner membrane structure and integrity, leading to cytochrome c release and apoptosis. *The Journal of biological chemistry* **278,** 7743–7746; 10.1074/jbc.C200677200 (2003).

34. Cogliati, S. *et al.* Mitochondrial cristae shape determines respiratory chain supercomplexes assembly and respiratory efficiency. *Cell* **155,** 160–171; 10.1016/j.cell.2013.08.032 (2013).

35. Eisner, V., Csordás, G. & Hajnóczky, G. Interactions between sarco-endoplasmic reticulum and mitochondria in cardiac and skeletal muscle - pivotal roles in Ca^{2+} and reactive oxygen species signaling. *Journal of cell science* **126,** 2965–2978; 10.1242/jcs.093609 (2013).

36. Hajnóczky, G. *et al.* Reliance of ER-mitochondrial calcium signaling on mitochondrial EF-hand Ca^{2+} binding proteins. Miros, MICUs, LETM1 and solute carriers. *Current opinion in cell biology* **29,** 133–141; 10.1016/j.ceb.2014.06.002 (2014).

37. Stefani, D. de *et al.* VDAC1 selectively transfers apoptotic Ca^{2+} signals to mitochondria. *Cell death and differentiation* **19,** 267–273; 10.1038/cdd.2011.92 (2012).

38. Glater, E. E., Megeath, L. J., Stowers, R. S. & Schwarz, T. L. Axonal transport of mitochondria requires milton to recruit kinesin heavy chain and is light chain independent. *The Journal of cell biology* **173,** 545–557; 10.1083/jcb.200601067 (2006).

39. Wang, X. & Schwarz, T. L. The mechanism of Ca^{2+} -dependent regulation of kinesin-mediated mitochondrial motility. *Cell* **136,** 163–174; 10.1016/j.cell.2008.11.046 (2009).

40. Gazaryan, I. G. & Brown, A. M. Intersection between mitochondrial permeability pores and mitochondrial fusion/fission. *Neurochemical research* **32,** 917–929; 10.1007/s11064-006-9252-2 (2007).

41. Rossignol, R. *et al.* Energy substrate modulates mitochondrial structure and oxidative capacity in cancer cells. *Cancer research* **64,** 985–993 (2004).

42. NavaneethaKrishnan, S., Rosales, J. L. & Lee, K.-Y. Loss of Cdk5 in breast cancer cells promotes ROS-mediated cell death through dysregulation of the mitochondrial permeability transition pore. *Oncogene* **37,** 1788–1804; 10.1038/s41388-017-0103-1 (2018).

43. Twig, G. *et al.* Fission and selective fusion govern mitochondrial segregation and elimination by autophagy. *The EMBO journal* **27,** 433–446; 10.1038/sj.emboj.7601963 (2008).

44. Szabadkai, G. *et al.* Drp-1-dependent division of the mitochondrial network blocks intraorganellar Ca^{2+} waves and protects against Ca^{2+}-mediated apoptosis. *Molecular cell* **16,** 59–68; 10.1016/j.molcel.2004.09.026 (2004).

45. Szabadkai, G. *et al.* Chaperone-mediated coupling of endoplasmic reticulum and mitochondrial Ca^{2+} channels. *The Journal of cell biology* **175,** 901–911; 10.1083/jcb.200608073 (2006).

46. Pennanen, C. *et al.* Mitochondrial fission is required for cardiomyocyte hypertrophy mediated by a Ca^{2+}-calcineurin signaling pathway. *Journal of cell science* **127,** 2659–2671; 10.1242/jcs.139394 (2014).

47. Huang, Q. *et al.* Mitochondrial fission forms a positive feedback loop with cytosolic calcium signaling pathway to promote autophagy in hepatocellular carcinoma cells. *Cancer letters* **403,** 108–118; 10.1016/j.canlet.2017.05.034 (2017).

48. Friedman, J. R. *et al.* ER tubules mark sites of mitochondrial division. *Science (New York, N.Y.)* **334,** 358–362; 10.1126/science.1207385 (2011).

49. Losón, O. C., Song, Z., Chen, H. & Chan, D. C. Fis1, Mff, MiD49, and MiD51 mediate Drp1 recruitment in mitochondrial fission. *Molecular biology of the cell* **24,** 659–667; 10.1091/mbc.E12-10-0721 (2013).

50. Arasaki, K. *et al.* A role for the ancient SNARE syntaxin 17 in regulating mitochondrial division. *Developmental cell* **32,** 304–317; 10.1016/j.devcel.2014.12.011 (2015).

51. Chang, C.-R. & Blackstone, C. Cyclic AMP-dependent protein kinase phosphorylation of Drp1 regulates its GTPase activity and mitochondrial morphology. *The Journal of biological chemistry* **282,** 21583–21587; 10.1074/jbc.C700083200 (2007).

52. Jeyaraju, D. V., Cisbani, G. & Pellegrini, L. Calcium regulation of mitochondria motility and morphology. *Biochimica et biophysica acta* **1787,** 1363–1373; 10.1016/j.bbabio.2008.12.005 (2009).

53. Irajizad, E., Ramachandran, R. & Agrawal, A. Geometric instability catalyzes mitochondrial fission. *Molecular biology of the cell* **30,** 160–168; 10.1091/mbc.E18-01-0018 (2019).

54. Stepanyants, N. *et al.* Cardiolipin's propensity for phase transition and its reorganization by dynamin-related protein 1 form a basis for mitochondrial membrane fission. *Molecular biology of the cell* **26,** 3104–3116; 10.1091/mbc.E15-06-0330 (2015).

55. Santel, A. & Fuller, M. T. Control of mitochondrial morphology by a human mitofusin. *Journal of cell science* **114,** 867–874 (2001).

56. Eura, Y., Ishihara, N., Yokota, S. & Mihara, K. Two mitofusin proteins, mammalian homologues of FZO, with distinct functions are both required for mitochondrial fusion. *Journal of biochemistry* **134,** 333–344 (2003).

57. Ishihara, N., Eura, Y. & Mihara, K. Mitofusin 1 and 2 play distinct roles in mitochondrial fusion reactions via GTPase activity. *Journal of cell science* **117,** 6535–6546; 10.1242/jcs.01565 (2004).

58. Song, Z., Chen, H., Fiket, M., Alexander, C. & Chan, D. C. OPA1 processing controls mitochondrial fusion and is regulated by mRNA splicing, membrane potential, and Yme1L. *The Journal of cell biology* **178,** 749–755; 10.1083/jcb.200704110 (2007).

59. Anand, R. *et al.* The i-AAA protease YME1L and OMA1 cleave OPA1 to balance mitochondrial fusion and fission. *The Journal of cell biology* **204,** 919–929; 10.1083/jcb.201308006 (2014).

60. Ehses, S. *et al.* Regulation of OPA1 processing and mitochondrial fusion by m-AAA protease isoenzymes and OMA1. *The Journal of cell biology* **187,** 1023–1036; 10.1083/jcb.200906084 (2009).

61. Klotzsch, E. *et al.* Superresolution microscopy reveals spatial separation of UCP4 and F_0F_1-ATP synthase in neuronal mitochondria. *Proceedings of the National Academy of Sciences of the United States of America* **112,** 130–135; 10.1073/pnas.1415261112 (2015).

62. Gold, V. A. M. *et al.* Visualizing active membrane protein complexes by electron cryotomography. *Nature communications* **5,** 4129; 10.1038/ncomms5129 (2014).

63. Liu, W. *et al.* Breaking the Axial Diffraction Limit. A Guide to Axial Super-Resolution Fluorescence Microscopy. *Laser & Photonics Reviews* **12,** 1700333; 10.1002/lpor.201700333 (2018).

64. Rego, E. H. *et al.* Nonlinear structured-illumination microscopy with a photoswitchable protein reveals cellular structures at 50-nm resolution. *Proceedings of the National Academy of Sciences of the United States of America* **109,** E135-43; 10.1073/pnas.1107547108 (2012).

65. Gustafsson, M. G. L. Surpassing the lateral resolution limit by a factor of two using structured illumination microscopy. SHORT COMMUNICATION. *J Microsc* **198,** 82–87; 10.1046/j.1365-2818.2000.00710.x (2000).

66. Littleton, B. *et al.* Coherent super-resolution microscopy via laterally structured illumination. *Micron (Oxford, England : 1993)* **38,** 150–157; 10.1016/j.micron.2006.07.010 (2007).

67. Ryu, J., Hong, S. S., Horn, B. K. P., Freeman, D. M. & Mermelstein, M. S. Multibeam interferometric illumination as the primary source of resolution in optical microscopy. *Appl. Phys. Lett.* **88,** 171112; 10.1063/1.2192153 (2006).

68. Wang, L., Pitter, M. C. & Somekh, M. G. Wide-field high-resolution structured illumination solid immersion fluorescence microscopy. *Optics letters* **36,** 2794–2796; 10.1364/OL.36.002794 (2011).

69. Chang, B.-J., Chou, L.-J., Chang, Y.-C. & Chiang, S.-Y. Isotropic image in structured illumination microscopy patterned with a spatial light modulator. *Optics express* **17,** 14710–14721; 10.1364/oe.17.014710 (2009).

70. Shao, L., Kner, P., Rego, E. H. & Gustafsson, M. G. L. Super-resolution 3D microscopy of live whole cells using structured illumination. *Nature methods* **8,** 1044–1046; 10.1038/nmeth.1734 (2011).

71. Hirvonen, L. M., Wicker, K., Mandula, O. & Heintzmann, R. Structured illumination microscopy of a living cell. *European biophysics journal : EBJ* **38,** 807–812; 10.1007/s00249-009-0501-6 (2009).

72. Förster, R. *et al.* Simple structured illumination microscope setup with high acquisition speed by using a spatial light modulator. *Optics express* **22,** 20663–20677; 10.1364/OE.22.020663 (2014).

73. Rust, M. J., Bates, M. & Zhuang, X. Sub-diffraction-limit imaging by stochastic optical reconstruction microscopy (STORM). *Nature methods* **3,** 793–795; 10.1038/nmeth929 (2006).

74. van de Linde, S. *et al.* Direct stochastic optical reconstruction microscopy with standard fluorescent probes. *Nature protocols* **6,** 991–1009; 10.1038/nprot.2011.336 (2011).

75. Endesfelder, U. & Heilemann, M. Direct stochastic optical reconstruction microscopy (dSTORM). *Methods in molecular biology (Clifton, N.J.)* **1251,** 263–276; 10.1007/978-1-4939-2080-8_14 (2015).

76. Vaughan, J. C., Jia, S. & Zhuang, X. Ultrabright photoactivatable fluorophores created by reductive caging. *Nature methods* **9,** 1181–1184; 10.1038/nmeth.2214 (2012).

77. Lehmann, M. *et al.* Multicolor Caged dSTORM Resolves the Ultrastructure of Synaptic Vesicles in the Brain. *Angewandte Chemie (International ed. in English)* **54,** 13230–13235; 10.1002/anie.201505138 (2015).

78. Betzig, E. *et al.* Imaging intracellular fluorescent proteins at nanometer resolution. *Science (New York, N.Y.)* **313,** 1642–1645; 10.1126/science.1127344 (2006).

79. Hell, S. W. & Wichmann, J. Breaking the diffraction resolution limit by stimulated emission. Stimulated-emission-depletion fluorescence microscopy. *Opt. Lett.* **19,** 780; 10.1364/OL.19.000780 (1994).

80. Pawley, J. B. *Handbook of biological confocal microscopy.* 3rd ed. (2006).

81. Klar, T. A., Jakobs, S., Dyba, M., Egner, A. & Hell, S. W. Fluorescence microscopy with diffraction resolution barrier broken by stimulated emission. *Proceedings of the National Academy of Sciences of the United States of America* **97,** 8206–8210; 10.1073/pnas.97.15.8206 (2000).

82. van de Linde, S., Sauer, M. & Heilemann, M. Subdiffraction-resolution fluorescence imaging of proteins in the mitochondrial inner membrane with photoswitchable fluorophores. *Journal of structural biology* **164,** 250–254; 10.1016/j.jsb.2008.08.002 (2008).

83. Fiolka, R., Shao, L., Rego, E. H., Davidson, M. W. & Gustafsson, M. G. L. Time-lapse two-color 3D imaging of live cells with doubled resolution using structured illumination. *Proceedings of the National Academy of Sciences of the United States of America* **109,** 5311–5315; 10.1073/pnas.1119262109 (2012).

84. York, A. G. *et al.* Resolution doubling in live, multicellular organisms via multifocal structured illumination microscopy. *Nature methods* **9,** 749–754; 10.1038/nmeth.2025 (2012).

85. Ishigaki, M. *et al.* STED super-resolution imaging of mitochondria labeled with TMRM in living cells. *Mitochondrion* **28,** 79–87; 10.1016/j.mito.2016.03.009 (2016).

86. Jans, D. C. *et al.* STED super-resolution microscopy reveals an array of MINOS clusters along human mitochondria. *Proceedings of the National Academy of Sciences of the United States of America* **110,** 8936–8941; 10.1073/pnas.1301820110 (2013).

87. Stoldt, S. *et al.* Mic60 exhibits a coordinated clustered distribution along and across yeast and mammalian mitochondria. *Proceedings of the National Academy of Sciences of the United States of America* **116,** 9853–9858; 10.1073/pnas.1820364116 (2019).

88. Gottschalk, B., Klec, C., Waldeck-Weiermair, M., Malli, R. & Graier, W. F. Intracellular Ca^{2+} release decelerates mitochondrial cristae dynamics within the junctions to the endoplasmic reticulum. *Pflugers Archiv : European journal of physiology* **470,** 1193–1203; 10.1007/s00424-018-2133-0 (2018).

89. Waldeck-Weiermair, M. *et al.* Generation of Red-Shifted Cameleons for Imaging Ca^{2+} Dynamics of the Endoplasmic Reticulum. *Sensors (Basel, Switzerland)* **15,** 13052–13068; 10.3390/s150613052 (2015).

90. Barnett, L., Platisa, J., Popovic, M., Pieribone, V. A. & Hughes, T. A fluorescent, genetically-encoded voltage probe capable of resolving action potentials. *PloS one* **7,** e43454; 10.1371/journal.pone.0043454 (2012).

91. Fallaize, D., Chin, L.-S. & Li, L. Differential submitochondrial localization of PINK1 as a molecular switch for mediating distinct mitochondrial signaling pathways. *Cellular signalling* **27,** 2543–2554; 10.1016/j.cellsig.2015.09.020 (2015).

92. Otsu, N. A Threshold Selection Method from Gray-Level Histograms. *IEEE Trans. Syst., Man, Cybern.* **9,** 62–66; 10.1109/TSMC.1979.4310076 (1979).

93. Poteser, M. *et al.* Live-cell imaging of ER-PM contact architecture by a novel TIRFM approach reveals extension of junctions in response to store-operated Ca^{2+}-entry. *Scientific reports* **6,** 35656; 10.1038/srep35656 (2016).

94. Yen, J. C., Chang, F. J. & Chang, S. A new criterion for automatic multilevel thresholding. *IEEE transactions on image processing : a publication of the IEEE Signal Processing Society* **4,** 370–378; 10.1109/83.366472 (1995).

95. Joshi, D. C. & Bakowska, J. C. Determination of mitochondrial membrane potential and reactive oxygen species in live rat cortical neurons. *Journal of visualized experiments : JoVE*; 10.3791/2704 (2011).

96. Gottschalk, B. *et al.* MICU1 controls cristae junction and spatially anchors mitochondrial Ca^{2+} uniporter complex. *Nature communications* **10,** 3732; 10.1038/s41467-019-11692-x (2019).

97. Wang, L. *et al.* Structural and mechanistic insights into MICU1 regulation of mitochondrial calcium uptake. *The EMBO journal* **33,** 594–604; 10.1002/embj.201386523 (2014).

98. Glytsou, C. *et al.* Optic Atrophy 1 Is Epistatic to the Core MICOS Component MIC60 in Mitochondrial Cristae Shape Control. *Cell reports* **17,** 3024–3034; 10.1016/j.celrep.2016.11.049 (2016).

99. Fülöp, L., Szanda, G., Enyedi, B., Várnai, P. & Spät, A. The effect of OPA1 on mitochondrial Ca^{2+} signaling. *PloS one* **6,** e25199; 10.1371/journal.pone.0025199 (2011).

100. Brito, O. M. de & Scorrano, L. Mitofusin-2 regulates mitochondrial and endoplasmic reticulum morphology and tethering. The role of Ras. *Mitochondrion* **9,** 222–226; 10.1016/j.mito.2009.02.005 (2009).

101. Klec, C. *et al.* Glycogen Synthase Kinase 3 Beta Controls Presenilin-1-Mediated Endoplasmic Reticulum Ca^{2+} Leak Directed to Mitochondria in Pancreatic Islets and β-Cells. *Cellular physiology and biochemistry : international journal of experimental cellular physiology, biochemistry, and pharmacology* **52,** 57–75; 10.33594/000000005 (2019).

102. Madreiter-Sokolowski, C. T. *et al.* Enhanced inter-compartmental Ca^{2+} flux modulates mitochondrial metabolism and apoptotic threshold during aging. *Redox biology* **20,** 458–466; 10.1016/j.redox.2018.11.003 (2019).

103. Picard, M. *et al.* Trans-mitochondrial coordination of cristae at regulated membrane junctions. *Nature communications* **6,** 6259; 10.1038/ncomms7259 (2015).

104. Giacomello, M. *et al.* Ca^{2+} hot spots on the mitochondrial surface are generated by Ca^{2+} mobilization from stores, but not by activation of store-operated Ca^{2+} channels. *Molecular cell* **38,** 280–290; 10.1016/j.molcel.2010.04.003 (2010).

105. Tong, J., McCarthy, T. V. & MacLennan, D. H. Measurement of Resting Cytosolic Ca^{2+} Concentrations and Ca^{2+} Store Size in HEK-293 Cells Transfected with Malignant Hyperthermia or Central Core Disease Mutant Ca^{2+} Release Channels. *The Journal of biological chemistry* **274,** 693–702; 10.1074/jbc.274.2.693 (1999).

106. Rajapaksha, M. *et al.* An Outer Mitochondrial Translocase, Tom22, Is Crucial for Inner Mitochondrial Steroidogenic Regulation in Adrenal and Gonadal Tissues. *Molecular and cellular biology* **36,** 1032–1047; 10.1128/MCB.01107-15 (2016).

107. Lam, S. S. *et al.* Directed evolution of APEX2 for electron microscopy and proximity labeling. *Nature methods* **12,** 51–54; 10.1038/nmeth.3179 (2015).

108. Rieger, B., Junge, W. & Busch, K. B. Lateral pH gradient between OXPHOS complex IV and $F_{(0)}F_{(1)}$ ATP-synthase in folded mitochondrial membranes. *Nature communications* **5,** 3103; 10.1038/ncomms4103 (2014).

109. Lam, A. K. M. & Galione, A. The endoplasmic reticulum and junctional membrane communication during calcium signaling. *Biochimica et biophysica acta* **1833,** 2542–2559; 10.1016/j.bbamcr.2013.06.004 (2013).

110. Yang, Z. & Watson, J. C. Molecular cloning and characterization of rho, a ras-related small GTP-binding protein from the garden pea. *Proceedings of the National Academy of Sciences of the United States of America* **90,** 8732–8736; 10.1073/pnas.90.18.8732 (1993).

111. MILLER, P. J. & JOHNSON, D. I. Characterization of theSaccharomyces cerevisiae cdc42-1ts Allele and New Temperature-Conditional-Lethalcdc42 Alleles. *Yeast* **13,** 561–572; 10.1002/(SICI)1097-0061(199705)13:6<561::AID-YEA114>3.0.CO;2-X (1997).

112. Lemmin, T., Bovigny, C., Lançon, D. & Dal Peraro, M. Cardiolipin Models for Molecular Simulations of Bacterial and Mitochondrial Membranes. *Journal of chemical theory and computation* **9,** 670–678; 10.1021/ct300590v (2013).

113. Schlame, M. Cardiolipin remodeling and the function of tafazzin. *Biochimica et biophysica acta* **1831,** 582–588; 10.1016/j.bbalip.2012.11.007 (2013).

114. Chakraborty, P. K. *et al.* MICU1 drives glycolysis and chemoresistance in ovarian cancer. *Nature communications* **8,** 14634; 10.1038/ncomms14634 (2017).

115. Tufi, R. *et al.* Comprehensive Genetic Characterization of Mitochondrial Ca^{2+} Uniporter Components Reveals Their Different Physiological Requirements In Vivo. *Cell reports* **27,** 1541-1550.e5; 10.1016/j.celrep.2019.04.033 (2019).

116. Antony, A. N. *et al.* MICU1 regulation of mitochondrial $Ca^{(2+)}$ uptake dictates survival and tissue regeneration. *Nature communications* **7,** 10955; 10.1038/ncomms10955 (2016).

117. Plovanich, M. *et al.* MICU2, a paralog of MICU1, resides within the mitochondrial uniporter complex to regulate calcium handling. *PloS one* **8,** e55785; 10.1371/journal.pone.0055785 (2013).

118. Tsai, M.-F. *et al.* Dual functions of a small regulatory subunit in the mitochondrial calcium uniporter complex. *eLife* **5**; 10.7554/eLife.15545 (2016).

119. Dong, Z. *et al.* Mitochondrial Ca^{2+} Uniporter Is a Mitochondrial Luminal Redox Sensor that Augments MCU Channel Activity. *Molecular cell* **65,** 1014-1028.e7; 10.1016/j.molcel.2017.01.032 (2017).

120. Patron, M. *et al.* MICU1 and MICU2 finely tune the mitochondrial Ca^{2+} uniporter by exerting opposite effects on MCU activity. *Molecular cell* **53,** 726–737; 10.1016/j.molcel.2014.01.013 (2014).

6 Supplementary materials

	Target	Sequence
si RNA	MICU1 si	5'-GCAGCUCAAGAAGCACUUCAAdTdT-3'
	nonCDSMICU1 si	5'-AGAAGUCUGUGAUGAUAAAdTdT-3'
	OPA1 si	5'-GUUAUCAGUCUGAGCCAGGdTdT-3'
	PRMT1 si	5'-CGUCAAACCCAACAAGUUAdTdT-3'
	MCU si 1	5'-GCCAGAGACAGACAAUACUdTdT-3'
	MCU si 2	5'-GGAAAGGGAGCUUAUUGAAdTdT-3'
	EMRE si	5'-GAACUUUGCUGCUCUACUUdTdT-3'
	taffazin si	5'-CCUACAGCUGCUUCUGGACCAAGUAdTdT-3'
	control si	5'-UUCUCCGAACGUGUCACGU-3'
cloning primer	MICU1 pos. 1 forward	5'-CCCGGATCCATGTTTCGTCTGAACTCACT-3'
	MICU1 pos. 1332 reverse	5'-GGTTGAATTCCATCAGCCGTTGCTTCATGAT-3'
	MICU1 pos. 210 reverse	5'-GGTTGAATTCTTTAGGTTGTCTACACATGG-3'
	MICU1 pos. 420 reverse	5'-GGTTGGATCCTTCAAGGTGGCAAAATATCGG-3'
	ROMO1 pos. 1 forward	5'-AAATCTAGACTCGAGCATGCCGGTGGCCGTGGGT-3'
	ROMO1 position 255 reverse	5'-CATACTCGAGTCTAGACGGATGCCCATCCCAATGG-3'
	mCherry for	5'-CGA-GAATTCATGGTGAGCAAGG-3'
	mCherry-myc P1 rev	5'-TGAGTTTTTGTTCGGATCCCTTGTACAGCTCGTCCATGCC-3'
	mCherry-myc P2 rev	5'-CGACGGCGCTATTCAGATCCTCTTCTGAGATGAGTTTTTGTTCGGATCCC-3'
	mCherry-myc-HIS P3 rev	5'-CCCTCTAGATTAATGGTGATGGTGATGATGGTCGACGGCGCTATTCAGATCC-3'
	mCherry HIS XbaI P4 rev	5'-CCCTCTAGATTAATGGTGATGG-3'
qRT-PCR	MICU1-for	5'-CAGGTTCAGAGCATCATTCG-3'
	MICU1-rev	5'-GAACACAAGCCAGACTTGAG-3'
	TAF-for	5'- GGAGAACAAGTCGGCTGTGGAG-3'
	TAF-rev	5'- GGAGCTGCTCTGCCTGAGTCTT-3'

Table 2: ***The siRNAs and primers used for experiments****. All siRNA used were purchased from Microsynth (Switzerland). Primer for cloning and qRT-PCR were purchased from Invitrogen (Vienna, Austria) [96]. [Figure reproduced from Gottschalk et al., Nature Communication 2019.]*

Figure	Reference label	Analysis label	Dilatation iterations	Erosion iterations	Fill holes
2b	EMRE-mCherry	MICU1-YFP	2	6	no
2g, 3a&b, supple. 11, supple. 12	MTR-FM	MICU1$^{1-70}$-GFP, MICU1$^{1-140}$-GFP, MICU1-YFP, ∆C-MICU1-YFP, MICU1-F-YFP, MICU1-K-YFP, MICU1-EF-YFP	2	6	no
4f	MTR-CMXROS	Cytochrome-c	3	3	no
6b&d, 7b&d, 8a, supple. 23, supple. 25, supple. 28, supple. 32	MICU1-YFP	MCU-mCherry, EMRE-mCherry, MTR-FM, UCP2-mCherry	1	6	yes
8c, supple. 24, supple. 33	MTG	UCP2-mCherry, MCU-mCherry	4	2	no

*Table 3: **IBM association index detailed parameter**. Summary of different directly comparable experiments and the analysis parameter (dilatation, erosion, fill holes) with references to figures, reference and analytic labels [96]. [Figure reproduced from Gottschalk et al., Nature Communication 2019.]*